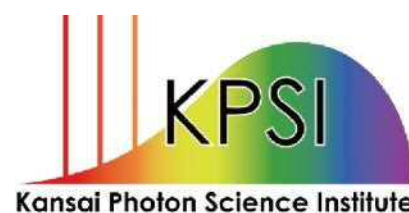# ANNUAL REPORT

2017

KANSAI PHOTON SCIENCE INSTITUTE
Quantum Beam Science Research Directorate
National Institutes for Quantum and Radiological Science and Technology

KPSI
Kansai Photon Science Institute

ANNUAL REPORT 2017

Contents

はじめに

　本年報では、関西光科学研究所（以下、関西研）において 2017 年度に実施された研究開発の主だった成果を紹介しています。関西研は 2016 年 4 月に国立研究開発法人量子科学技術研究開発機構（以下、量研）の研究開発拠点として再出発しました。けいはんな学研都市にある京都府木津地区と兵庫県播磨地区にある 2 つのサイトには、研究系職員約 80 名及びそれを支える技術系・事務系スタッフを含めて総勢約 150 名のスタッフが働いており、量研における関西研のミッションである「レーザーや放射光による光科学技術の研究開発」を推進しています。木津地区では、世界トップレベルの高強度レーザー技術を基盤としたレーザー加速やX線発生等のレーザー駆動の新しい放射線源開発、レーザーの短パルス性を活かした超高速計測技術開発、そして放射線影響や創薬に資する量子生命科学の最先端の研究開発を実施しています。また、播磨地区では、大型放射光施設 SPring-8 に 2 本の専用ビームラインと計算機シミュレーションを活用することで、新しい放射光X線利用技術開発と物質材料科学の最先端研究を展開しています。

　量研関西研として 2 年が経ち、新しい組織の中で優れた研究成果が生まれ始めています。木津地区の J-KAREN レーザーでは、可変形鏡を導入することで波面補正等を行った結果、集光強度として $1 \times 10^{22} \mathrm{W/cm^2}$ を達成し、それを用いたレーザー加速やX線発生実験等への運用を開始しました。特にレーザー加速研究に関しては、今年度より内閣府の受託事業 ImPACT に加え、JST の未来社会創造事業を受託することで研究開発が加速しています。播磨地区においても、放射光X線を用いたX線領域の新しい磁気光学効果（イナミ効果）の発見、高圧下における新しい鉄系高温超伝導相の発見、そして燃料電池触媒の性能低下の原因の解明など、優れた成果が数多く出始めています。また、光技術の社会実装の観点から、非侵襲血糖値測定技術やレーザーによるトンネル検査技術の実用化に向けた取組を引き続き行っています。

　関西光科学研究所は、「光」を通じた我が国の量子科学技術の発展とイノベーション戦略に貢献する開かれた研究拠点としての役割を果たすべく、今後とも職員一同、より一層努力してまいります。皆様のご理解・ご協力を宜しくお願い申し上げます。

<div style="text-align: right">

関西光科学研究所　所長

河内　哲哉

</div>

Preface

This annual report from the Kansai Photon Science Institute (KPSI) provides highlights of the scientific and technical research that was conducted over the 2017 fiscal year.

KPSI was reconstituted in April 2016 as one of the research and development bases of the National Institute of Quantum and Radiological Science and Technology (QST). At KPSI's two research sites—the Kizu site in Keihanna Science City in Kyoto Prefecture and the Harima site in Hyogo Prefecture—there are around 150 staff members, comprising around 80 researchers and the technical and administrative staff who support them. We promote the research and development of optical science and technology using lasers and synchrotron-radiation X-rays, which is the mission of KPSI in QST. At the Kizu site, we are conducting state-of-the-art research such as (i) developing new types of laser-driven radiation sources such as laser-accelerated particle beams and ultrashort X-rays based upon world-leading top-class high-intensity laser technology, (ii) ultrahigh-speed measurement technology using short laser pulses, and (iii) quantum life science that helps us understand radiation effects and develop new medicines. At the Harima site, using two contract beamlines of SPring-8 and computer simulations, we are developing new technology to utilize synchrotron-radiation X-rays and carrying out state-of-the-art research in material science.

Two years have passed since the restart of KPSI in QST and the new organization is beginning to produce outstanding research results. The J-KAREN laser system at the Kizu site has achieved a focusing intensity of 10^{22} W/cm^2 as the result of wavefront compensation by means of a deformable mirror system, and experiments using this laser are now underway on laser acceleration and X-ray generation. In particular, laser acceleration research is promoted by entrusting the external budget JST-Mirai R&D program from this fiscal year, in addition to the ImPACT research program of the Cabinet Office. Many outstanding results have also begun to flow from the Harima site, such as the discovery of a new magneto-optical effect in the X-ray region (the so-called *Inami effect*), a new high-temperature superconducting phase in iron-based material, and clarification of why the performance of fuel-cell catalysts degrade. In addition, regarding the social implementation of optical technology, we are making efforts toward practical application of non-invasive blood glucose measurement and laser-based tunnel inspection technology.

KPSI will continue to fulfill our role as an open research center of the "science of light" and will contribute to quantum science and technology and the strategy for innovation in Japan. We appreciate your understanding and cooperation.

Director General of KPSI
Tetsuya KAWACHI

Activities of KPSI

関西光科学研究所の主な動き

大阪大学とシンポジウム共催

　大阪大学と量研合同で、5月9〜10日に大阪大学銀杏会館（大阪府吹田市）にて、「光・量子ビーム科学合同シンポジウム 2017」を開催しました。同じく、11月24日にリーガロイヤルホテル大阪（大阪府大阪市）にて、「光量子ビーム科学シンポジウム 2017　光量子ビーム科学コ・クリエーション」を開催しました。

海外研究機関と研究協力に関する覚書締結

　国内外の研究機関との連携は、マシンタイムを始めとする研究リソース不足の補填、技術交流による双方の研究開発の加速、世界的に見た関西研の立ち位置の再確認等の観点から、その重要度が増しています。関西研としても積極的に他機関との連携を進め、更なる開かれた研究所を目指しています。

　7月13日　ルーマニア　ホリア・フルベイ国立物理学・原子力工学研究所と覚書締結（高強度レーザーを用いた科学共同研究に関する覚書）

　12月7日　ドイツ　ヘルムホルツ機構ドレスデン－ローゼンドルフ研究所と覚書締結（高強度レーザー及びその応用研究に関する覚書）

　12月9日　チェコ　ELI-Beam Line Project と覚書締結（高強度レーザーおよびそれを用いた高強度場科学に関する覚書）

　2018年2月12日　韓国　光州科学技術院相対論的レーザー科学センターと覚書締結（ハイパワーレーザー技術とレーザー生成プラズマ科学の学術的連携に関する覚書）

兵庫県内の科学イベント出展

　7月9日〜12日に第17回 SPring-8 夏の学校が開催され、関西研は12の主催団体の一つとして貢献しました。次世代の放射光利用研究者の発掘と育成を目的として、主に大学院修士課程の学生を対象として、2001年より毎年開校しています。関西研では、主としてビームライン14B1における実習（放射光を利用した高温高圧合成）を実施しました。7月22〜23日には、兵庫県姫路市の桜山公園にて開催された「桜山公園祭り」科学の屋台村へ出展しました。

QST 認定第1号ベンチャー設立

　関西研量子生命科学研究部レーザー医療応用研究グループの山川考一グループリーダーらが開発した高輝度中赤外レーザー（波長：6μm〜9μm）を用いた、採血なしで血糖値を測定する技術（非侵襲血糖値測定技術）の実用化を目指す「ライトタッチテクノロジー株式会社（代表取締役社長兼任：山川考一）」が、7月5日に QST ベンチャー第1号として認定され、7月10日に正式に設立されました。

木津地区の主な出展イベント

　2017 年度も積極的にアウトリーチ活動を実施しました。きっづ光科学館ふぉとんは年間来場者 4 万人を達成しました。
7 月 29 日〜30 日「青少年のための科学の祭典 2017 全国大会」ブース出展　科学技術館（東京都千代田区）
9 月 28 日〜29 日「京都スマートシティエキスポ 2017」出展　けいはんなオープンイノベーションセンター（京都府相楽郡精華町）
10 月 26 日〜28 日「けいはんな情報通信フェア 2017」＆「第 12 回けいはんなビジネスメッセ 2017」出展　けいはんなプラザ（京都府相楽郡精華町）
10 月 29 日　大阪科学技術館 OSTEC　サイエンス・ステージ「QST Kansai Presents 光のマジックショー」出展　大阪科学技術センター（大阪府大阪市西区）

原子力機構レーザー共同研究所と成果報告会を共催

　原子力機構レーザー共同研究所と関西研合同で、11 月 21 日「レーザー応用技術産学官連携成果報告会」を原子力機構レーザー共同研究所（福井県敦賀市）にて開催しました。

第 10 回文部科学省「最先端の光の創成を目指したネットワーク研究拠点プログラム」シンポジウム開催

　1 月 23 日に京都大学国際科学イノベーション棟（京都府京都市）において、第 10 回文部科学省「最先端の光の創成を目指したネットワーク研究拠点プログラム」シンポジウムが開催され、関西研は 9 の主催団体の 1 つとして貢献しました。

JAEA-QST 放射光科学シンポジウム 2018/文部科学省ナノテクノロジープラットフォーム事業微細構造解析プラットフォーム放射光利用技術セミナー開催

　関西研の放射光科学研究センター、原子力機構物質科学研究センター、文部科学省ナノテクノロジープラットフォームの主催により、SPring-8（兵庫県佐用郡佐用町）にて 3 月 12〜14 日にシンポジウム・セミナーを開催しました。設立 3 年目を迎える QST 放射光科学研究センター、および、JAEA 放射光エネルギー材料研究ディビジョンにおける放射光利用研究の最新成果と将来計画が報告されました。1 日目の QST のセッションでは、稲見俊哉グループリーダーが「X 線発光における磁気円二色性」について紹介しました。

User Facilities

主要な施設・装置

木津地区

○J-KAREN レーザー装置

【装置概要】

　世界トップクラスの極短パルス超高強度レーザーです。30J のレーザーエネルギーを 30 フェムト秒（1 フェムトは 1000 兆分の 1）の時間に閉じ込めることにより 1000 兆ワットの超高強度を実現します。（上の写真は強力な励起レーザーの光で緑色に光っています。）

【装置性能】

・照射エネルギー：30 J/pulse
・コントラスト比：10^{-12}
・波長：800 nm
・繰り返し：0.1 Hz
・パルス幅：30 フェムト秒
・集光強度：10^{22} W/cm²

【主要な研究課題】

　レーザーの高度化技術の開発、イオンおよび電子のレーザー加速技術の開発、高エネルギーコヒーレント X 線の発生等

○X 線レーザー実験装置

【装置概要】

　強力なレーザーで作ったプラズマを使って発振する X 線のレーザーです。目に見える光に比べて発振波長が短く、さらにほんの一瞬の短い間しか光らないという特徴を生かして、ものの表面で起こる物性現象の変化の様子の観察等に利用しています。

【装置性能】

・照射エネルギー：1 µJ/pulse
・波長：13.9 nm
・繰り返し：0.1Hz
・パルス幅：約 10 ピコ秒

【主要な研究課題】

　軟 X 線光学素子の評価、フェムト秒レーザーアブレーションの機構解明
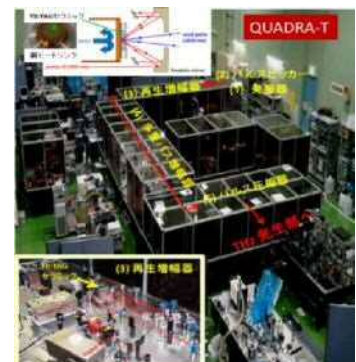
○QUADRA-T レーザーシステム

【装置概要】

　1 秒間に 1000 発のレーザーパルスが繰り出せる高平均出力ピコ秒パルスレーザーです。中心周波数 0.3THz の高強度テラヘルツパルスを発生することが可能です。

【装置性能】

・照射エネルギー：10 mJ/pulse
・波長：1 µm

・繰り返し：1kHz
・パルス幅：1 ピコ秒
【主要な研究課題】
　高繰り返し高出力レーザーの開発、高強度テラヘルツ光源の開発、テラヘルツパルスによる分子の選択的励起技術の開発

播磨地区

　播磨地区では大型放射光施設 SPring-8 に 2 本の QST 専用ビームラインを設置しているほか、日本原子力研究開発機構（JAEA）の専用ビームラインにも複数の放射光専用実験装置を常設しています。一方で、QST 専用ビームラインにも、JAEA の専用実験装置が常設されています。

○BL11XU（QST 極限量子ダイナミクス I ビームライン）
【装置概要】
　SPring-8 標準の真空封止アンジュレータを光源とし、マルチ結晶交換システムを装備することで、広範囲のエネルギー領域の高輝度放射光 X 線を高効率に利用できるビームラインです。
【装置性能】
・光源：真空封止アンジュレータ
・エネルギー領域：6～70keV
・分光結晶：Si(111)、Si(311)
・実験装置：放射光メスバウアー分光装置、共鳴非弾性 X 線散乱装置、及び表面 X 線回折計

1. 放射光メスバウアー分光装置

　^{57}Fe, ^{61}Ni 等のメスバウアー核種を対象とした放射光メスバウアー分光が可能で、物質の電子、磁気状態から格子振動状態に関する情報などを得ることができます。

2. 共鳴非弾性 X 線散乱装置

　2m 長アームに搭載した球面湾曲型集光式アナライザー結晶による背面反射を用いることで、高分解能の X 線分光を行い、散乱光の方位や入射光とのエネルギー差から、運動量移行を伴う固体内素励起が観察できます。

3. 表面 X 線回折計

　分子線エピタキシー（MBE）チェンバーを搭載した表面構造解析用装置で、窒化物を含む半導体結晶などの成長過程を、X 線回折法を用いてその場観察・リアルタイム観察することができます。
【主要な研究課題】
　金属薄膜の原子層単位での磁性探査、白金系燃料電池触媒の電子状態解析、半導体量子ドットや半導体多層膜の成長過程のリアルタイム解析

○BL14B1（QST 極限量子ダイナミクス II ビームライン）
【装置概要】
　偏向電磁石を光源とすることで、連続スペクトルを持つ白色 X 線や高エネルギーの単色 X 線が利用可能なビームラインです。全反射ミラーや分光結晶の曲げ機構によって、試料位置への集光が可能となっています。

【装置性能】
・光源：偏向電磁石
・エネルギー領域：白色 X 線（5〜150keV）、単色 X 線（5〜90keV）
・実験装置：高温高圧プレス装置、分散型 XAFS 測定装置（JAEA）及び κ（カッパ）型回折計（JAEA）

1. 高温高圧プレス装置

　高温高圧の条件下にある試料を、白色 X 線を用いたエネルギー分散型 X 線回折法やラジオグラフィー法、単色 X 線を用いた XAFS（X 線吸収微細構造）法や角度分散型 X 線回折法によって調べることができます。

【主要な研究課題】
　高圧下での金属水素化物形成過程のその場観察

○BL22XU（JAEA 専用ビームライン）における放射光専用実験装置

1. 単色 X 線実験用高温高圧プレス装置（JAEA　BL22XU）

　高温高圧下（到達圧力 10GPa（10 万気圧）、到達温度 2000K　程度）の X 線回折測定や X 線吸収法を用いた密度測定、室温、1MPa 未満の水素ガス雰囲気中でのその場 X 線回折観察、時分割 X 線回折測定が可能な装置です。

2. ダイヤモンドアンビルセル回折計（JAEA　BL22XU）

　大型イメージングプレート検出器と高エネルギーX 線を利用することにより、高圧下での単結晶 X 線回折及び粉末 X 線回折実験、X 線全散乱測定及び原子二体分布関数（PDF）解析が可能な装置です。

3. 大型 X 線回折計

　共鳴 X 線散乱による電子軌道状態の観測、スペックル回折によるドメイン構造の研究、応力・歪み分布測定などの回折マッピングなど多目的に利用する四軸回折計です。

【主要な研究課題】
　水素貯蔵合金の水素吸蔵過程の時分割その場 X 線回折測定、負の熱膨張材料、超伝導体、f 電子系化合物、コヒーレント X 線を利用したスペックル散乱によるナノドメイン観察。応力・歪の 3 次元分布測定、等

施設の稼働実績

○光量子科学研究施設

実施課題件数

装置名称	独自研究	受託研究	共同研究	施設共用
J-KAREN レーザー装置	1	0	0	0
X 線レーザー実験装置	1	0	3	3
QUADRA-T レーザーシステム	3	0	1	0
kHz チタンサファイアレーザー	4	0	3	0
X 線回折装置	4	0	4	0
軟 X 線平面結像型回折格子	48	0	0	1

○放射光科学研究施設

　2017 年度の SPring-8 蓄積リングの運転時間は 5280 時間で、放射光利用時間はそのうちの 4512 時間でした。量研、原子力機構とも専用ビームラインでは 10〜20%弱程度の調整時間を除き、放射光利用時間で独自研究や受託研究、外部利用者への施設共用と研究支援を行っています。

実施課題件数

ビームライン	独自研究	受託研究	共同研究	施設共用
BL11XU	7	0	4	16
BL14B1	6	0	0	2
BL22XU	4	0	1	18

利用日数

ビームライン	独自研究	受託研究	共同研究	施設共用
BL11XU	60	0	45	56
BL14B1	36	0	0	6
BL22XU	32	0	5	47

施設の利用状況

○光量子科学研究施設

J-KARENレーザー装置
（合計ビームタイム：1440時間）

- メンテナンス：25%
- 内部利用：75%
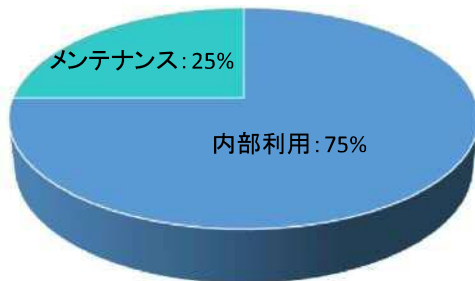
X線レーザー装置
（合計ビームタイム：1745時間）

- メンテナンス：24%
- 施設共用：5%
- 共同研究：22%
- 内部利用：49%
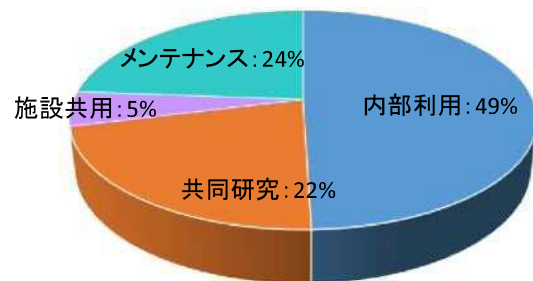
QUADRA-Tレーザー装置
（合計ビームタイム：1092時間）

- 内部利用：100%
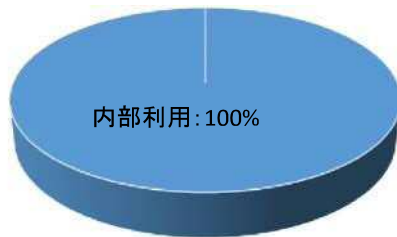
その他装置（木津地区）
（合計ビームタイム：960時間）

- 共同研究：17%
- 内部利用：83%

○放射光科学研究施設

QST極限量子ダイナミクスⅠビームライン（BL11XU）
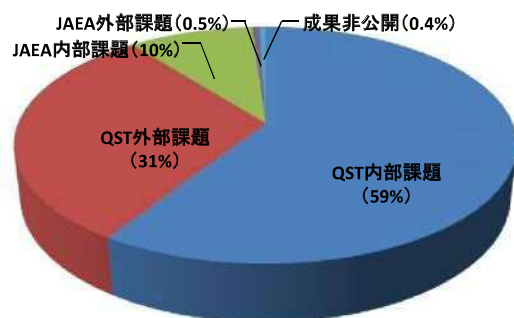
- JAEA外部課題（0.5%）
- 成果非公開（0.4%）
- JAEA内部課題（10%）
- QST外部課題（31%）
- QST内部課題（59%）

QST極限量子ダイナミクスⅡビームライン（BL14B1）

- JAEA内部課題（30%）
- QST内部課題（21%）
- QST外部課題（4%）
- JAEA外部課題（46%）

JAEA重元素科学Ⅰビームライン（BL22XU）

- 成果非公開(2%)
- JAEA外部課題（14%）
- QST内部課題（24%）
- JAEA内部課題(34%)
- QST外部課題（28%）

JAEA重元素科学Ⅱビームライン（BL23SU）

- JAEA内部課題（30%）
- QST内部課題（18%）
- JAEA外部課題（52%）

Research Highlights

Laser performance of J-KAREN-P facility laser

Hiromitsu Kiriyama

Advanced Laser Group, Department of Advanced Photon Research

The J-KAREN laser facility [1] delivered a single-shot on-target intensity of 10^{21} W/cm^2 with a temporal contrast of $\sim 10^{12}$. J-KAREN has been upgraded to J-KAREN-P to realize petawatt (PW) peak-power pulses on target at a repetition rate of 0.1 Hz with an intensity capability of over 10^{22} W/cm^2. Such progress in high-field science will give rise to new applications and breakthroughs, including relativistic particle acceleration, bright X-ray source generation, and nuclear activation. Many other interesting features can be investigated with PW and higher-intensity laser pulses, including relativistic transparency and radiation friction.

J-KAREN-P is shown schematically in Fig. 1. The output pulses with high temporal contrast and uniform spatial profile from the power amplifier [1] are up-collimated and enter booster amplifier 1 (BA1), which uses an 80-mm-diameter Ti:sapphire crystal pumped with ~ 50 J from two commercial Nd:glass green lasers at a repetition rate of 0.1 Hz. The pulses from BA1 are then amplified in booster amplifier 2 (BA2), which uses a 120-mm-diameter Ti:sapphire crystal pumped with ~ 100 J from four commercial Nd:glass green lasers at 0.1 Hz. A deformable mirror is installed in the laser chain to correct the wavefront distortion. The amplified pulses are up-collimated to a diameter of ~ 250 mm, and finally, compressed in the compressor consisting of four 1,480 grooves/mm gold-coated gratings of 565×360 mm^2.

A maximum output energy of 23 J was achieved with an incident pump energy of 47 J with a good conversion efficiency of 49% from BA1. The near-field beam profile has a homogeneous and uniform spatial intensity distribution. The amplified spectrum from the Ti:sapphire amplifiers is red-shifted because of saturation. As a mitigating measure, the amplifier input spectrum is blue-shifted by tuning the phase-match setting of the BBO crystals in the OPCPA amplifier.

Figure 2 shows the measured dependence of the output broadband energy from BA2 on the total pump energy at a repetition rate of 0.1 Hz. A maximum output energy of 63 J is achieved with an incident energy of 92 J. The figure clearly shows that the experimental data fit the simulation. Figure 3 shows the typical spatial profile of the laser beam from BA2. The profile has a homogeneous and uniform intensity distribution (Fig. 3(a)).

After BA2, the wavefront distortions are corrected using a deformable mirror. The beam is then sent into the pulse compressor. The measured spectrum has a bandwidth of ~ 50 nm (FWHM). The recompressed pulse duration is obtained as less than 30 fs. The peak power is expected to be over PW at 0.1 Hz on target because the beam-line throughput from the laser room to the target chamber including the compressor is $\sim 60\%$. With an f/1.3 off-axis parabolic mirror, according to measurements of the focal spot and encircled energy, a peak intensity of 10^{22} W/cm^2 is achievable with a power level of 0.3 PW [2] (Fig. 3(a)). The contrast is measured with a third-order cross correlator for the laser pulse without pumping the booster amplifiers, as shown in Fig. 4. The contrast earlier than 200 ps before the main pulse is 3×10^{-12} (detection limited). At 100, 50, 10, and 5 ps before the main pulse, the contrast is roughly 10^{-11}, 6×10^{-10}, and 8×10^{-9}, respectively.

Laser-driven acceleration via the interaction of short, intense laser pulses with matter is known as laser-plasma acceleration. Compared to radio-frequency accelerators, it features higher accelerating electric fields, shorter acceleration distances, and shorter bunch lengths. Laser acceleration of protons [3] and electrons with the J-KAREN-P laser system is being tested. Currently, protons in excess of 50 MeV [4] are obtained with $\sim 10^{21}$ W/cm^2 and GeV-class electrons are obtained with $\sim 10^{20}$ W/cm^2. We will optimize the target and increase the laser intensity gradually while checking the total system. Laser-plasma acceleration can replace the front end of a conventional accelerator system and would help greatly in downsizing accelerator systems, especially for heavy ions [5]. Also, in progress are experiments on (i) high-order harmonics from relativistic singularities [6,7], (ii) multi-MeV pure proton beam generation from micro-size hydrogen cluster targets [8], and (iii) X-ray spectroscopy of laser-plasma interaction in the ultra-relativistic regime [9].

From national laboratories to university departments, ultra-high-intensity lasers have evolved to become one of the most important scientific tools for studying matter in extreme states. The J-KAREN-P laser system is a leading facility in the provision and application of ultra-high-intensity lasers for the broad scientific community. It has been used in various pioneering and cutting-edge studies, which has resulted in high-impact discoveries for high-field science.

Multi-PW lasers are now being constructed for specific applications in many fields ranging from proton therapy for cancer treatment to the simulation of astrophysical phenomena. The next generation of lasers will approach exawatt (EW =
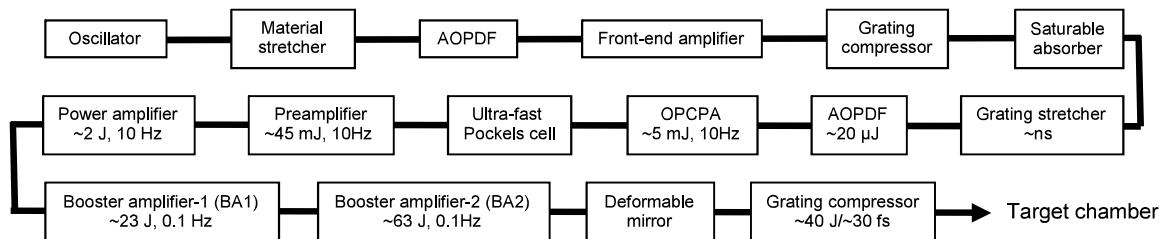

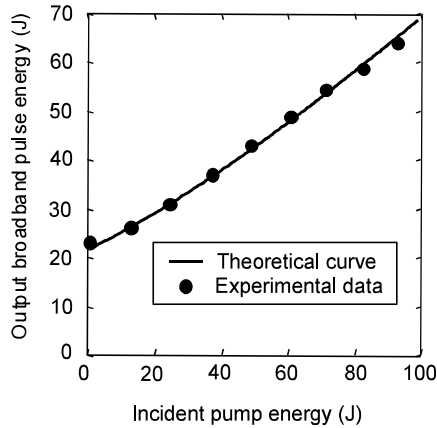Fig. 1.   Schematic setup of the J-KAREN-P laser system.

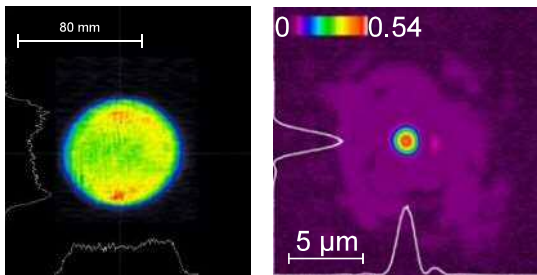Fig. 2. Measured broadband output energy from the final.

Fig. 3. Measured (a) near-field and (b) far-field profiles of the output beam.
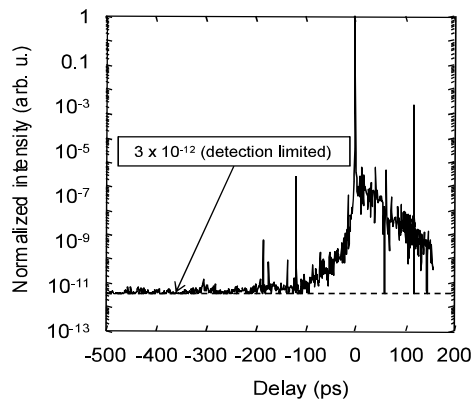

Fig. 4. Measured contrast of the recompressed pulse.

10^{18} W) power levels and may allow us to reach conditions beyond those that occur naturally in the universe.

References

1. H. Kiriyama, M. Mori, A. S. Pirozhkov, K. Ogura, A. Sagisaka, A. Kon, T. Zh. Esirkepov, Y. Hayashi, H. Kotaki, M. Kanasaki, H. Sakaki, Y. Fukuda, J. Koga, M. Nishiuchi, M. Kando, S. V. Bulanov, K. Kondo, P. R. Bolton, O. Slezak, D. Vojna, M. Sawicka-Chyla, V. Jambunathan, A. Lucianetti, and T. Mocek: IEEE Sel. Topics J. Quantum Electron. (Invited Paper) 21 (2015) 1601118.
2. A. S. Pirozhkov, Y. Fukuda, M. Nishiuchi, H. Kiriyama, A. Sagisaka, K. Ogura, M. Mori, M. Kishimoto, H. Sakaki, N. P. Dover, K. Kondo, N. Nakanii, K. Huang, M. Kanasaki, K. Kondo, and M. Kando: Opt. Exp. 25 (2017) 20486.
3. H. Daido, M. Nishiuchi, and A. S. Pirozhkov: Rep. Prog. Phys. 75 (2012) 056401-71.
4. M. Nishiuchi, H. Kiriyama, H. Sakaki, N. P. Dover, K. Kondo, A. S. Pirozhkov, A. Sagisaka, Y. Fukuda, K. Nishitani, T. Miyahara, K. Ogura, M. A. Alkhimova, T. A. Pikuz, A. Ya Faenov, Y. Watanabe, J. Koga, S. V. Bulanov, M. Kando, and K, Kondo: Proc. SPIE 10241 (2017).
5. M. Nishiuchi, H. Sakaki, T. Zh. Esirkepov, K. Nishio, T. A. Pikuz, A. Ya. Faenov, I. Yu. Skobelev, R. Orlandi, H.Sako, A. S. Pirozhkov, K. Matsukawa, A. Sagisaka, K. Ogura, M. Kanasaki, H. Kiriyama, Y. Fukuda, H. Koura, M. Kando, T. Yamauchi, Y. Watanabe, S. V. Bulanov, K. Kondo, K. Imai, and S. Nagamiya: Phys. Plasmas. 22 (2015) 033107.
6. A. S Pirozhkov, M. Kando, T. Zh Esirkepov, P. Gallegos, H. Ahmed, E. N Ragozin, A. Ya Faenov, T. A Pikuz, T. Kawachi, A. Sagisaka, J. K Koga, M. Coury, J. Green, P. Foster, C. Brenner, B. Dromey, D. R Symes, M. Mori, K. Kawase, T. Kameshima, Y. Fukuda, L. Chen, I. Daito, K. Ogura, Y. Hayashi, H. Kotaki, H. Kiriyama, H. Okada, N. Nishimori, T. Imazono, K. Kondo, T. Kimura, T. Tajima, H. Daido, P. Rajeev, P. McKenna, M. Borghesi, D. Neely, Y. Kato, and S. V Bulanov: New J. Phys. 16 (2014) 093003.
7. A. S. Pirozhkov, T. Zh. Esirkepov, T. A. Pikuz, A. Ya. Faenov, K. Ogura, Y. Hayashi, H. Kotaki, E. N. Ragozin, D. Neely, H. Kiriyama, J. K. Koga, Y. Fukuda, A. Sagisaka, M. Nishikino, T. Imazono, N. Hasegawa, T. Kawachi, P. R. Bolton, H. Daido, Y. Kato, K. Kondo, S. V. Bulanov, and M. Kando: Sci. Rep., in press.
8. S. Jinno, H. Tanaka, R. Matsui, M. Kanasaki, H. Sakaki, M. Kando, K. Kondo, A. Sugiyama, M. Uesaka, Y. Kishimoto, and Y. Fukuda: Opt. Exp. 25 (2017) 18774.
9. M. A. Alkhimova, A. Y. Faenov, I. Y. Skobelev, T. A. Pikuz, M. Nishiuchi, H. Sakaki, A. S. Pirozhkov, A. Sagisaka, N. P. Dover, K. Kondo, K. Ogura, Y. Fukuda, H. Kiriyama, K. Nishitani, T. Miyahara, Y. Watanabe, S. A. Pikuz, M. Kando, R. Kodama, and K. Kondo: Opt. Express 25 (2017) 29501.

J-KAREN-P laser approached the diffraction-limited, bandwidth-limited Petawatt

Alexander S. Pirozhkov,[1] Yuji Fukuda,[1] Mamiko Nishiuchi,[1] Hiromitsu Kiriyama,[1] Akito Sagisaka,[1] Koichi Ogura,[1] Michiaki Mori,[1] Maki Kishimoto,[1] Hironao Sakaki,[1] Nicholas P. Dover,[1] Kotaro Kondo,[1] Nobuhiko Nakanii,[1] Kai Huang,[1] Masato Kanasaki,[1,2] Kiminori Kondo,[1] and Masaki Kando[1]

[1]Advanced Laser Group, Department of Advanced Photon research
[2]Graduate School of Maritime Sciences, Kobe University

J-KAREN-P is a high-power laser facility aiming at the highest beam quality and irradiance for performing state-of-the-art experiments at the frontier of modern science. Here, we approached the physical limits of the beam quality—diffraction limit of the focal spot and bandwidth limit of the pulse shape—removing the chromatic aberration, angular chirp, wavefront, and spectral phase distortions. We performed accurate measurements of the spot and peak fluence after an f/1.3 off-axis parabolic mirror under full amplification at a power of 0.3 PW attenuated with 10 high-quality wedges, resulting in a Strehl ratio of ~0.5 and an irradiance of ~10^{22} W/cm^2, which is the highest accurately estimated irradiance demonstrated to date.

The performance of ultrafast petawatt-class lasers has gradually and steadily improved in recent years. However, the final beam diameter of high-power lasers is typically 20–30 cm to prevent the damage caused to the compressor gratings. Such a wide beam makes it challenging to achieve a tightly focused beam with clean pulse compression. The major difficulties include wavefront and spectral phase distortions and various spatiotemporal couplings, e.g., chromatic aberration and angular chirp. If not dealt with carefully, all these effects result in poor focal spot and pulse shape, i.e., low irradiance. Typically, the irradiance drops by order(s) of magnitude, destroying the main advantage of high-power lasers, i.e., their high irradiance capability.

J-KAREN-P [1] is a high-power laser facility aiming at the highest beam quality and irradiance for performing state-of-the-art experiments at the frontier of modern science. We have recently achieved a major breakthrough and approached the physical limits of the beam quality [2]: the diffraction limit of the focal spot (Fig. 1) and the bandwidth limit of the pulse shape (Fig. 2).
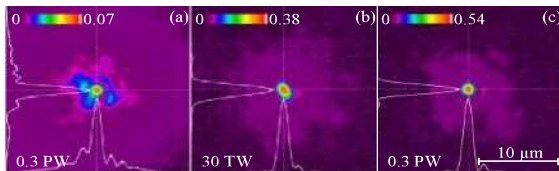
Importantly, we have measured the focal spot after an f/1.3 off-axis parabolic mirror (OAP) during 0.3 PW operation. The laser beam was attenuated by 10 wedges with high surface quality confirmed with interferometry. The resulting focal spot had a Strehl ratio of 0.46 ± 0.06 and an effective radius [3] $r_{eff} = 1.02 \pm 0.07$ μm (Fig. 1). We have thus achieved the highest accurately characterized at-focus irradiance of $0.93(\pm0.12) \times 10^{22}$ W/cm^2.

We also performed a full-beam duration measurement, down-collimating the Ø280 mm beam to a few millimeters using a telescope consisting of two off-axis parabolic mirrors. The full-beam pulse duration and shape were nearly identical to the duration and shape measured using a few-millimeter-diameter pick-off, confirming the high spatiotemporal quality of the beam and the absence of spatiotemporal couplings.

This breakthrough was made possible by significantly improved laser performance [1] and careful design and accurate construction of the beamline (Fig. 3), including increased optics size, mirror-based low-aberration expanders, several monitors for reproducible alignment, a deformable mirror and wavefront sensors for wavefront correction (Fig. 4), attenuation paths, and focal spot monitors for accurate spot characterization.

The high quality of the J-KAREN-P laser will result in enhanced proton and ion acceleration, coherent x-ray generation, and electron acceleration in the on-going and near-future experiments.
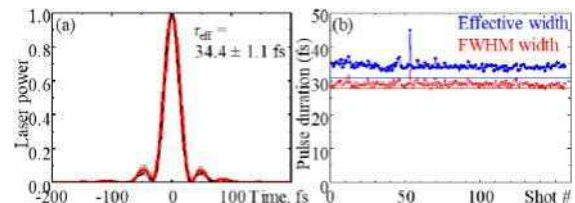
Fig. 2.   J-KAREN-P pulse (Wizzler, 156 shots). (a) Laser power, gray area shows shot-to-shot standard deviation, dashed line shows bandwidth-limited pulse. (b) Effective [4] and full width at half maximum (FWHM) pulse width history; horizontal lines show the bandwidth limits.

Fig. 1.   J-KAREN-P focal spot, f/1.3 OAP; color scale maxima = Strehl ratios. (a) Starting spot. (b) 1st step: chromatic aberration removed, wavefront corrected. (c) Final spot: angular chirp compensated. (a) and (c): booster amplifier operating at 0.3 PW; (b): power amplifier, 30 TW.

Fig.3. J-KAREN-P beamline (part after the final amplifier is shown); the beamline is covered to reduce air fluctuations. M_1−M_7: monitors (far, near fields through dielectric mirrors). DM: deformable mirror. W_1, W_5, W_6: wavefront sensors. P: periscope. ×1.5 and ×2.1: mirror expanders. [1−4] : alignment CCDs. OAP_5−OAP_7: high-quality f = 2,000 mm OAPs for alignment and beam characterization. OAP8: in-vacuum f = 350 mm (f/1.3, 45° deviation) OAP focusing the beam on target. T_1 and T_2: two target areas. S_5−S_8: focal spot monitors.

Fig. 4 J-KAREN-P wavefront; the values are rms errors. (a) Before deformable mirror, beam Ø90 mm. (b) After deformable mirror, beam Ø90 mm. (c) Before the compressor; the Ø280 mm beam is focused by the f/7 alignment OAP.
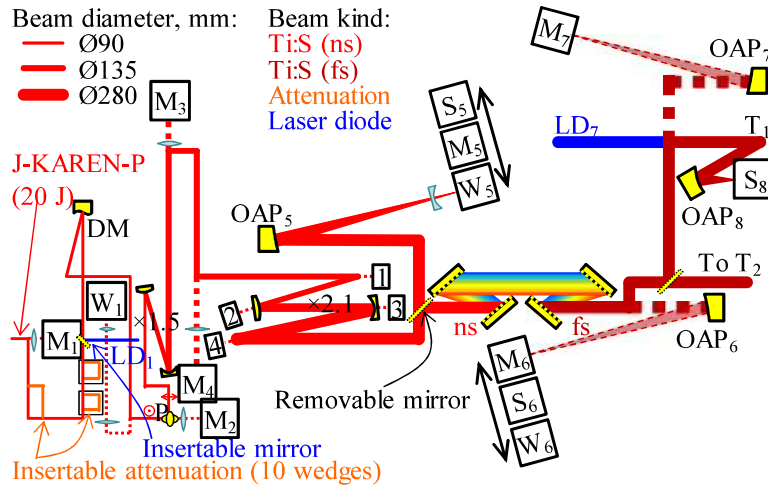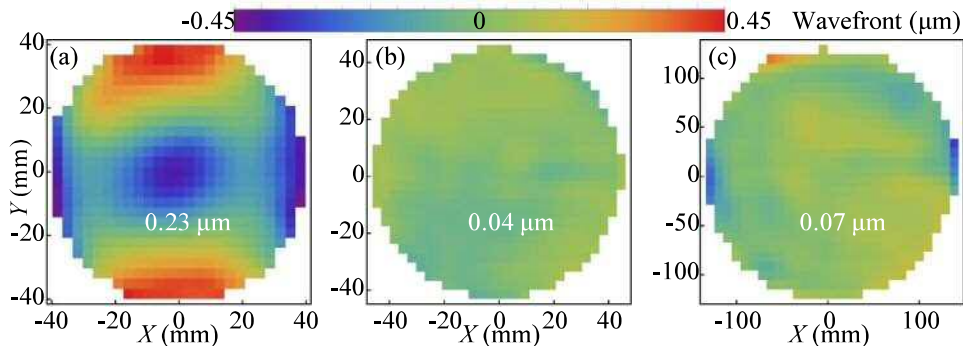
References

1. H. Kiriyama, M. Mori, A. S. Pirozhkov, K. Ogura, A. Sagisaka, A. Kon, T. Zh. Esirkepov, Y. Hayashi, H. Kotaki, M. Kanasaki, H. Sakaki, Y. Fukuda, J. Koga, M. Nishiuchi, M. Kando, S. V. Bulanov, K. Kondo, P. R. Bolton, O. Slezak, D. Vojna, M. Sawicka-Chyla, V. Jambunathan, A. Lucianetti, and T. Mocek, "High-Contrast, High-Intensity Petawatt-Class Laser and Applications," IEEE J. Sel. Topics Quantum Electron. 21 1601118-18 (2015).

2. S. Pirozhkov, Y. Fukuda, M. Nishiuchi, H. Kiriyama, A. Sagisaka, K. Ogura, M. Mori, M. Kishimoto, H. Sakaki, N. P. Dover, K. Kondo, N. Nakanii, K. Huang, M. Kanasaki, K. Kondo, and M. Kando, "Approaching the diffraction-limited, bandwidth-limited Petawatt," Opt. Express 25, 20486 (2017).

3. The effective radius is defined as $\pi \cdot r_{eff}^2 = \int F(x,y)dxdy$, where $F(x,y)$ is the normalized fluence distribution. The peak irradiance is $I_0 = P_0/(\pi \cdot r_{eff}^2)$; this estimate is correct, unlike the commonly used incorrect estimate of P_0/d_{FWHM}^2.

4. The effective pulse width is $\tau_{eff} = \int p(t)dt$, where $p(t)$ is the normalized laser power. The peak power is $P_0 = E_{Laser}/\tau_{eff}$; this estimate is correct, unlike the commonly used incorrect estimate of E_{Laser}/τ_{FWHM}.

17

Delbrück Scattering with Polarized Gamma Rays to Probe Vacuum Polarization

James K. Koga[1] and Takehito Hayakawa[2]

[1]High-Intensity Laser Science Group, Department of Advanced Photon Research
[2]Project LCS gamma-ray, Tokai Quantum Beam Science Center

Probably the most common use of polarized light is when people go to see 3D movies at movie theaters. Images with a slight offset are shown on the movie screen with different polarizations. If viewed with the naked eye, all one sees is a blurred image. However, by wearing glasses that have different polarization-filter orientations for each eye, one can see a 3D image from a 2D movie screen. Similarly, we have found that by using polarized gamma rays when scattering them off atoms, we can "see" more clearly the nature of vacuum than would be possible with unpolarized gamma rays [1]. Vacuum can be polarized by electromagnetic fields by the formation of virtual electron–positron pairs [2]. The polarization effect of these virtual electron–positron pairs on electromagnetic waves is extremely small and difficult to detect. One way in which such an effect has been measured is by the scattering of gamma rays off the Coulomb field of atomic nuclei, which is called Delbrück scattering (Fig. 1), in which virtual electron–positron pairs that result from the interaction scatter the gamma rays [3]. The scattering cross section of Delbrück scattering increases as $(Z\alpha)^4$ [2], where Z is the atomic number of the nucleus and α is the fine-structure constant ($\alpha^{-1} \sim 137.036$) [4]. Although this cross section increases rapidly with the atomic number, its isolated measurement is difficult. First, the elastic scattering of gamma rays from atoms is a coherent combination of four different processes, namely Rayleigh, Thomson, giant dipole resonance (GDR), and Delbrück scattering [5–7]. Second, unpolarized gamma-ray sources were previously used to measure it [5,6]. As a result, although scattering measurements have been performed for gamma rays of various energies, Delbrück scattering was measured on the basis that it is a necessary contribution to the total scattering for the results to agree with theoretical calculations [8]. In 1977, De Tollis and Pistoni pointed out that by using photons with polarization parallel to the scattering plane, two of the four scattering contributions, namely Rayleigh and GDR scattering, go to zero at scattering angles of 90° [9]. Now, high-flux linearly polarized gamma-ray sources from laser Compton scattering are becoming available, such as ELI-NP-GBS [10]. As a result, we investigated whether Delbrück scattering can be isolated using such polarized gamma-ray sources.

Thomson and GDR scattering amplitudes can be calculated fairly simply [11], but Rayleigh and Delbrück scattering amplitudes require more complex calculations. Rayleigh scattering amplitudes have been calculated previously using the relativistic second-order S matrix and form factors [12] and can be found in a database [13]. However, because we required finer resolution, we used the "ENTING" code to recalculate them [11,12]. Delbrück scattering amplitudes have also been calculated previously using the lowest-order vacuum polarization tensor, and exist in tabular form [14]. Because finer resolution was necessary and no code was available to calculate the Delbrück scattering amplitudes, we constructed our own code
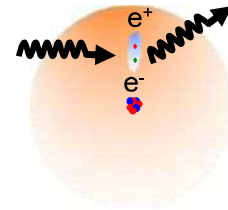
Fig. 1. γ-ray scattering off Coulomb field of nucleus

using the compact formulae from [9,15,16]. The values were found to agree with the tabular values. Because equations for the higher-order forms of Delbrück scattering are yet to be calculated, we chose regimes in which these effects are predicted to be small [8,17]. As a result, we calculated the amplitudes for 1,100 keV gamma rays scattering off tin ($Z = 50$). Figure 2 shows the results of the calculations for the differential scattering amplitude for all four elastic scattering processes (reproduced from Fig. 4 of [1]). It can be seen that at $\theta \sim 70°$, Delbrück scattering is much larger than that of the other three components, indicating that a measurement at this angle gives a nearly isolated measurement of Delbrück scattering [1].

In conclusion, we have found through extensive calculations that Delbrück scattering can be nearly isolated from other processes contributing to the elastic scattering of gamma rays from atoms. A precise measurement of this vacuum contribution to the scattering of gamma rays can lead to the discovery of new physics if the measurements disagree with theoretical models. In the future, experimental measurements are expected to be carried out at facilities with high-flux polarized gamma-ray sources.
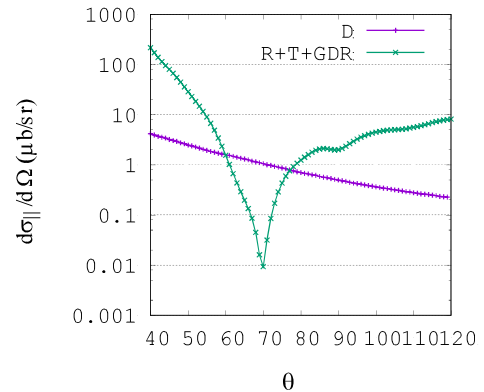
Fig. 2. Differential scattering amplitude verses angle for Delbrück scattering (D) and Rayleigh, Thomson, and giant dipole resonance scattering (R+T+GDR) at 1,100 keV for tin (reproduced from Fig. 4 of [1]).

References

1. J. K. Koga and T. Hayakawa, *Phys. Rev. Lett.* **118**, 204801 (2017).
2. V. Costantini, B. De Tollis, and G. Pistoni, *Nuovo Cimento Soc. Ital. Fis. A* **2**, 733 (1971).
3. L. Meitner, H. Kösters, and M. Delbrück, *Z. Phys.* **84**, 137 (1933).
4. https://physics.nist.gov/cgi-bin/cuu/Value?alph
5. A. Milstein and M. Schumacher, *Phys. Rep.* **243**, 183 (1994).
6. M. Schumacher, *Radiat. Phys. Chem.* **56**, 101 (1999).
7. P. Papatzacos and K. Mork, *Phys. Rep.* **21**, 81 (1975).
8. B. Kasten, et al., *Phys. Rev. C* **33**, 1606 (1986).
9. B. De Tollis and G. Pistoni, *Il Nuovo Cimento* **42**, 499 (1977).
10. K. Dupraz, et al., *Phys. Rev. ST Accel. Beams* **17**, 033501 (2014).
11. P. Rullhusen, et al., *Phys. Rev. C* **23**, 1375 (1981).
12. L. Kissel, *Radiat. Phys. Chem.* **59**, 185 (2000).
13. L. Kissel (private communication).
14. H. Falkenberg, et al., *At. Data Nucl. Data Tables* **50**, 1 (1992).
15. B. De Tollis, M. Lusignoli, and G. Pistoni, *Nuovo Cimento Soc. Ital. Fis. A* **32**, 227 (1976).
16. B. De Tollis and L. Luminari, *Nuovo Cimento Soc. Ital. Fis. A* **81**, 633 (1984).
17. B. Kunwar, et al., *Phys. Rev. A* **71**, 032724 (2005).

Burst Intensification by Singularity Emitting Radiation (BISER)

A. S. Pirozhkov[1], T. Zh. Esirkepov[1], T. A. Pikuz[2,3], A. Ya. Faenov[3,4], K. Ogura[1], Y. Hayashi[1], H. Kotaki[1], E. N. Ragozin[5,6], D. Neely[7,8], H. Kiriyama[1], J. K. Koga[1], Y. Fukuda[1], A. Sagisaka[1], M. Nishikino[1], T. Imazono[1], N. Hasegawa[1], T. Kawachi[1], P. R. Bolton[1,13], H. Daido[9], Y. Kato[10], K. Kondo[1], S. V. Bulanov[1,11,12], M. Kando[1]

[1]High Intensity Laser Science Group, Kansai Photon Science Institute
[2]Graduate School of Engineering, Osaka University
[3]Joint Institute for High Temperatures of the Russian Academy of Sciences
[4]Open and Transdisciplinary Research Initiatives, Osaka University
[5]P. N. Lebedev Physical Institute of the Russian Academy of Sciences
[6]Moscow Institute of Physics and Technology, State University
[7]Central Laser Facility, Rutherford Appleton Laboratory
[8]Department of Physics, SUPA, University of Strathclyde
[9]Naraha Remote Technology Development Center, Japan Atomic Energy Agency
[10]The Graduate School for the Creation of New Photonics Industries
[11]A. M. Prokhorov Institute of General Physics of the Russian Academy of Sciences
[12]Institute of Physics of the Czech Academy of Sciences
[13]Present address: Chair of Experimental Physics and Medical Physics, Faculty of Physics

We have recently demonstrated experimentally the phenomenon of burst intensification by singularity emitting radiation (Fig. 1), where extremely bright coherent X-rays are emitted by relativistic density singularities in plasma driven by high-power ultrashort pulse lasers [1–3]. Promising scalings indicate that this compact ultra-bright coherent X-ray source can approach the brightness of present-day free electron lasers at photon energies from 10 eV to a few kiloelectronvolts.

Coherent X-ray sources are indispensable in fundamental research and applications in life sciences, material sciences, and nanotechnology. Recent trends in development of coherent X-ray sources include two broad classes: large-scale accelerator-based X-ray FELs (XFELs) and compact laser-based sources such as X-ray lasers and atomic high-order harmonics. Fundamental limitations of conventional techniques severely hinder the development of a bright compact coherent X-ray source, especially at kiloelectronvolt photon energies. Relativistic laser plasma gives a new class of bright coherent sources. Among them, a substantial portion is based on the KPSI scientists' inventions, which include relativistic high-order harmonic generation in overdense plasmas, e.g., via the relativistic oscillating mirror [4] or relativistic sliding mirror [5-6] model. Another important representative is based on coherent X-ray generation in underdense plasmas via the relativistic flying mirror [7-10] model.

BISER is a new phenomenon in which relativistic plasma singularities are used to obtain ultra-bright coherent X-rays. Our research combines several fields: catastrophe theory (i.e., the study of singularities), nonlinear plasma physics, and the development of coherent X-ray sources. Since the 1970s, it has been realized that structurally stable singularities play a fundamental role in nature [11]. Singularities explain a wide range of phenomena ranging from physical effects to animal behavior and social processes. For example, catastrophe theory explains the large-scale structure of the Universe (galaxy clustering) [12,13]. Singularities are produced widely by multi-stream flows, which are ubiquitous in nature, such as with shock waves and jets in astrophysical and laboratory plasmas.
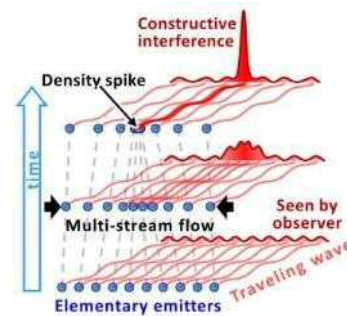
Fig. 1. Burst intensification by singularity emitting radiation (BISER).

Catastrophe theory explains the existence, universality, and structural stability of singularities, i.e., their insensitivity to perturbations.

If a singularity occurs in an emitting medium, the emission from the singularity location can be extremely intense and coherent because of constructive wave interference (N^2 effect) (Fig. 1). This is a fundamental general effect that is applicable to any medium capable of emitting traveling waves, e.g., electromagnetic, acoustic, or gravitational. However, this effect was overlooked for at least 40 years. We found indications of this effect several years ago [1,2]: We discovered experimentally a new surprising ultra-bright coherent X-ray source in relativistic laser plasma and developed a theory showing that the coherent X-rays are generated by relativistic plasma singularities. In particular, for linearly polarized lasers, the theory predicts two singularities situated in the laser polarization plane. In our recent paper [3], we confirmed this cornerstone prediction by demonstrating experimentally a nanometer-scale double source with individual emitters situated along the laser polarization (Figs. 2 and 3). This helped us finally to formulate the BISER mechanism and generalize it to other types of travelling waves, thereby eliminating the 40-year lacuna in knowledge.

Fig. 2. PIC simulation revealing X-ray sources at the electron density spikes (singularities), and an image of the two point-like sources obtained experimentally in the LiF plate.

Fig. 3. (a) Harmonic combs corresponding to the two point-like X-ray sources. (b) Detail of the spectrum. (c) Pulse train seen in PIC simulation. (d) Black: a portion of the pulse train from (c); red: transform-limited shortest-possible pulse deduced from (a).

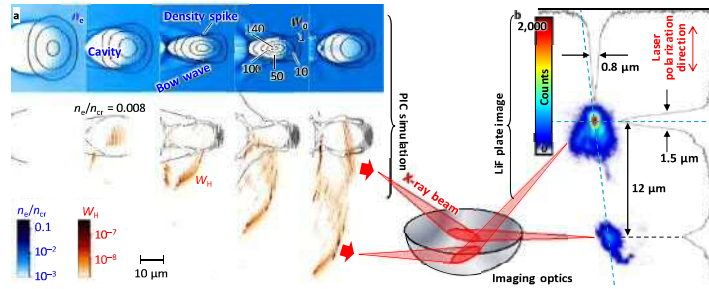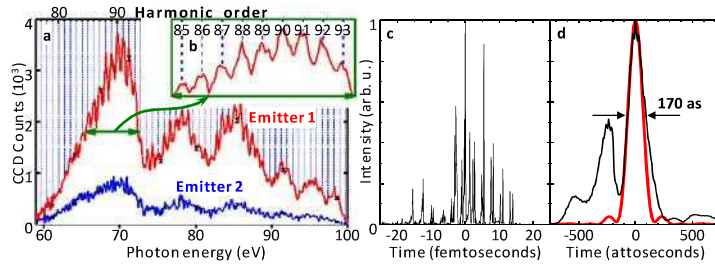Essentially, the singularity is a phase object through which elementary emitters flow continuously. This differs fundamentally from a compact bunch, which consists of the same emitters. Furthermore, in contrast to a particle bunch, the singularity is determined by the multi-stream flow and has a non-local nature. BISER radiation is both spatially and temporally coherent, as evidenced by the fringes in the LiF image and spectra in Figs. 2b and 3b, respectively. We emphasize that the spatial coherence of our point-like source is not explained by the propagation effect (van Cittert–Zernike theorem), which would require ~20 km propagation. Our source demonstrates coherence at a distance of 286 mm. Therefore, the fringes that appear in the image are due to source coherence and not propagation. This differs fundamentally from a typical phase-contrast experiment with an incoherent source.

Besides studying singularities in general, we showed that BISER is a promising coherent X-ray source. It is driven by relatively compact lasers (~10–50 m scale) focused on high-repetition-rate, debris-free gas-jet targets. Typical laser parameters are a pulse duration of 30–50 fs, a peak power of 2 TW to 1 PW, and a relativistic irradiance far greater than 10^{18} W/cm². BISER is favorably scalable, with a photon yield proportional to the laser power squared, which we demonstrated to be up to 120 TW [1,2]. Together with high photon numbers (we demonstrated 10^{10} photons/pulse in the 60–100 eV spectral range) and extremely small source size (tens of nanometers), BISER exhibits a very high peak spectral brightness, e.g., 10^{27} photons/mm²·mrad²·s in 0.1% bandwidth. This is much brighter than any synchrotron, although two-to-three orders of magnitude lower than that provided by the brightest available sources, namely FELs. However, unlike present FELs, BISER is not only spatially but also *temporally* coherent, ultrashort (simulations show ~100 attoseconds), and compact, and available for university and industry laboratories.

Acknowledgments

References

1. S. Pirozhkov, M. Kando, T. Zh. Esirkepov, P. Gallegos, H. Ahmed, et al., "Soft-x-ray harmonic comb from relativistic electron spikes," Phys. Rev. Lett. 108, 135004 (2012).
2. Pirozhkov, M.Kando, T.Esirkepov, P.Gallegos, H.Ahmed, et al. "High order harmonics from relativistic electron spikes," New J. Phys. 16 093003 (2014).
3. A. S. Pirozhkov, T. Zh. Esirkepov, T. A. Pikuz, A. Ya. Faenov, K. Ogura, et al., "Burst intensification by singularity emitting radiation in multi-stream flows," Scientific Reports 7, 17968 (2017).
4. S. V. Bulanov, N. M. Naumova, and F. Pegoraro, "Interaction of an ultrashort, relativistically strong laser-pulse with an overdense plasma," Phys. Plasmas 1, 745 (1994).
5. A. S. Pirozhkov, S. V. Bulanov, T. Zh. Esirkepov, M. Mori, A. Sagisaka, and H. Daido, "Attosecond pulse generation in the relativistic regime of the laser-foil interaction: The sliding mirror model," Phys. Plasmas 13, 013107 (2006).
6. A. S. Pirozhkov, S. V. Bulanov, T. Zh. Esirkepov, M. Mori, A. Sagisaka, and H. Daido, "Generation of high-energy attosecond pulses by the relativistic-irradiance short laser pulse interacting with a thin foil," Phys. Lett. A 349, 256 (2006).
7. M. Kando, Y. Fukuda, A. S. Pirozhkov, J. Ma, I. Daito, et al., "Demonstration of laser-frequency upshift by electron-density modulations in a plasma wakefield," Phys. Rev. Lett. 99, 135001 (2007).
8. A. S. Pirozhkov, J. Ma, M. Kando, T. Zh. Esirkepov, Y. Fukuda, et al., "Frequency multiplication of light back-reflected from a relativistic wake wave," Phys. Plasmas 14, 123106 (2007).
9. M. Kando, A. S. Pirozhkov, K. Kawase, T. Zh. Esirkepov, Y. Fukuda, et al., "Enhancement of photon number reflected by the relativistic flying mirror," Phys. Rev. Lett. 103, 235003 (2009).
10. S. V. Bulanov, T. Zh. Esirkepov, M. Kando, A. S. Pirozhkov, and N. N. Rosanov, "Relativistic mirrors in plasmas. Novel results and perspectives," Phys. Usp. 56, 429 (2013).
11. E. C. Zeeman, "Catastrophe theory" in Scientific American, Apr (1976), p. 65.
12. V. I. Arnold, S. F. Shandarin, and Ya. B. Zeldovich, "The large scale structure of the universe I. General properties. One-and two-dimensional models," Geophysical & Astrophysical Fluid Dynamics 20, 111 (1982).
13. S. Shandarin, Ya. Zeldovich, "The large-scale structure of the universe: Turbulence, intermittency, structures in a self-gravitating medium," RMP 61, 185 (1989).

Development of a proton beam profile diagnostic for laser-plasma ion sources

Nicholas P. Dover, Mamiko Nishiuchi and Hironao Sakaki

High Intensity Laser Science Group, Kansai Photon Science Institute

The interaction of a high-intensity laser with a plasma is an attractive source of ion beams because of their high peak current, high charge, and low emittance and because of the compactness of the accelerator [1]. During the laser interaction with thin foil targets, electrons are heated to relativistic energies and form a sheath at the target surface. This sheath can accelerate surface ions to high energies. Typically, protons are accelerated preferentially because of their high concentration in surface contaminants and high charge-to-mass ratio.

Experiments conducted over the last few decades have primarily been performed at low repetition rate, motivating the use of passive single-use diagnostics such as radiochromic film stacks or nuclear track detectors. However, state-of-the-art Ti:sapphire lasers have recently demonstrated ~1 Hz repetition rates with the peak power and energy required to generate >MeV ion beams [2]. This has motivated the need for a new class of high-repetition diagnostics, particularly for transverse beam profile measurements, for which the transverse beam pattern depends on the energy band of the typical thermal spectrum.

Recently, plastic scintillators have been used to perform proton-beam profile measurements from laser plasma accelerators. They are attractive because of their flexibility, large size, and modest cost, as well as not being sensitive to the copious electromagnetic noise generated during the laser–plasma interaction. Preliminary studies showed measurement of multi-MeV proton beams with good spatial resolution but poor energy resolution [3]. A variation of the technique was recently demonstrated, in which differential filtering was used to form macro-pixels of different energy bands, sacrificing spatial resolution for significantly improved energy resolution [4]. However, in those initial studies, little attention was paid to scintillator nonlinear response and calibration.

We have therefore developed a simple and robust novel scintillator-based proton-beam profile (SB-PBP) diagnostic based on differential filtering, providing a flexible compromise between spatial and energy resolution [5]. We consider the nonlinear scintillation response and use accurate calibration to provide a true estimate of the angularly resolved energy spectrum. We also show that this technique can be used for protons in excess of 20 MeV, significantly higher than that demonstrated previously.

The response of plastic scintillators to ion irradiation is well known to be nonlinear with stopping power dE/dx because of ionization quenching [6]. Typically, the semi-empirical Birks model is used to characterize this, in which the density-normalized scintillation yield $L'=L/\rho$, in units of total energy of emitted photons per unit path length per incident particle, is given as

$$\frac{dL'}{dx} = \frac{\eta \frac{dE'}{dx}}{1 + kB\frac{dE'}{dx} + C\left(\frac{dE'}{dx}\right)^2} , \qquad (1)$$

where kB and C are experimentally determined scintillator-dependent constants and η is the scintillation efficiency. In this study, we used the EJ-232Q-0.5% scintillator and kB and B from recent calibration data of the chemically identical BC-422Q [7], and calibrated η using a known dose of 80 MeV protons at the Hyogo Ion Beam Medical Center (HIBMC), Japan.

We calculated the expected photon yield of incident protons of different energies entering the scintillator after passing through differential filtering (here, PTFE of differing thickness) by performing a series of TRIM [8] Monte Carlo simulations. The stopping power in the scintillator was taken from the simulations, and Eq. (1) was then integrated to calculate the scintillator yield. The total luminescence as a function of incident proton energy is shown in Fig. 1a. Increasing the thickness of the filter removes the contribution from lower-energy protons. Therefore, by using differing filter thickness and making an assumption about the incident energy spectrum of the protons, it is possible to reproduce the absolute original spectrum approximately.

In the design that follows, we use a macropixel with four different thicknesses (Fig. 1b and c), with each pixel 5 × 5 mm^2. This is performed by interlacing bars of differing thickness (or material, if desired) in a square lattice, making it easy and cheap to fabricate. Laser proton sources feature diverging beams; therefore, the angular resolution of the beam profile depends on the macropixel size and the distance between the target and detector. The energy resolution depends on the number of thicknesses used. It is simple to change this and the macropixel size, thereby optimizing the trade-off between spatial and energy resolution for each experimental setup.

We tested the diagnostic on an ion-acceleration experimental campaign with the J-KAREN-P laser at the Kansai Photon Science Institute, National Institutes for Quantum and Radiological Science and Technology, Japan. A ~15 J, ~40 fs pulse was focused with an f/1.3 off-axis parabola onto a thin foil target at a 45° angle of incidence. Proton beams in excess of ~30 MeV were generated. To benchmark the SR-PBP diagnostic, we sampled the upper half of the proton beam as shown in Fig. 2.
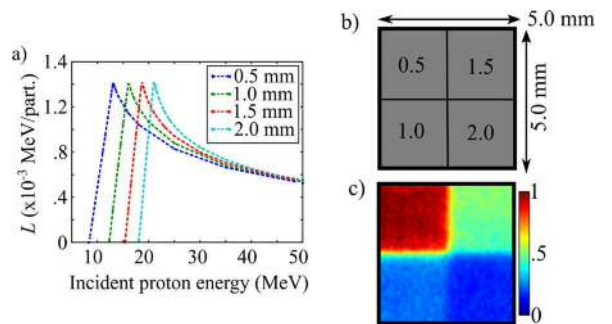

Fig. 1. a) Total scintillator luminescence as a function of incident proton energy for PTFE filters of differing thickness. b) Square filter macropixel design with thicknesses of PTFE in mm. c) Example of normalized scintillation of one macropixel after irradiation.
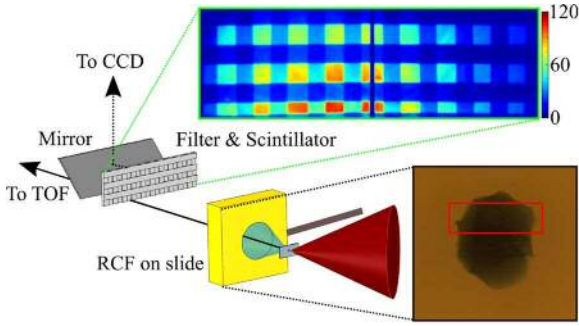
Fig. 2. Experimental setup for SB-PBP diagnostic implementation in J-KAREN-P experiment. Inset in green is a raw CCD image from the SB-PBP, and that in black is an RCF layer corresponding to a Bragg peak of 14.7 MeV showing the full proton beam. The corresponding ROI measured by SB-PBP is shown by the red box.

Fig. 3. a) Interpolated beam profiles for the different filter thicknesses from SB-PBP. b) Angularly resolved proton spectrum along horizontal plane.

The proton-beam maximum energy along the target normal was measured by a time-of-flight detector [9], and on some shots, a dose-calibrated RCF stack was inserted into the beam to confirm the scintillator calibration. The SB-PBP filtering was the same as that shown in Fig. 1. The grid pattern caused by the differential-filter lattice is clearly visible in the inset in Fig. 2.

The raw CCD data from the PBP were split into macropixels as shown in Figs. 1. The CCD counts were then interpolated between the macropixels, as shown in Fig. 3a, on a nonlinear scale for a 5 μm stainless-steel target. Clearly, the CCD counts are larger for thinner filters. Also, the divergence of the signal narrows with increasing filter thickness. This narrowing of proton divergence with energy is typical for laser proton sources and is visible in the RCF data [5].

The proton-beam spectrum was then estimated using a least-squares fitting algorithm. From the RCF stack, the proton beam was found to typically exhibit a thermal spectrum well described by

$$\frac{dN(E)}{dE} \propto \frac{1}{E^{1/2}} exp(-2\,E/E_0)^{1/2}, \qquad (2)$$

where E is the proton energy, E_0 is the beam temperature, and the spectrum extends up to a cut-off energy E_m determined by the time-of-flight diagnostic. Using Eq. (2) and stopping curves like those shown in Fig. 1, the estimated photon output was calculated and compared with the experimentally measured photon output. Using the beam temperature E_0 and the total proton flux as fitting factors, the spectrum was then determined by the least-squares method. More details of the spectrum retrieval are given in Dover et al. [5].

This fitting procedure is carried out for each macropixel individually to give an estimated proton spectrum at each macropixel point. In Fig. 3b, the angularly resolved spectrum in the horizontal plane (along 4° in the vertical plane) is shown. As is typical from laser ion sources, the beam has a wide divergence that narrows with increasing energy. During the experiment, a systematic shift of the angle corresponding to the maximum proton energy was observed (in Fig. 3b, this is roughly −8° from the target normal, corresponding to a shift toward the laser axis). This has been determined to be due to nonthermal effects of the rear sheath expansion characteristic of ultra-short and ultra-intense laser pulses [10] and will be discussed in detail in a future publication.
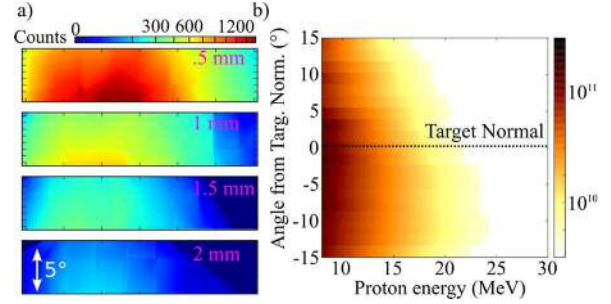
We have therefore demonstrated the effectiveness of a scintillator-based beam-profile diagnostic to simultaneously measure the transverse beam profile and coarsely estimate the beam energy spectrum. We have carefully included the nonlinearity of plastic scintillators into our spectral retrieval to allow us to make accurate measurements of the absolute proton flux. We have shown that this diagnostic is effective in measuring protons in excess of 20 MeV. It would be difficult to increase this energy range because of an increasingly large background from energetic electrons that are also generated in the laser–plasma interaction. However, these can be eliminated using a time-gated CCD camera and fast-quenched CCD, which will be the subject of future research [5]. This novel diagnostic will therefore be of great interest to high-repetition-rate laser facilities and particularly for applications using laser-driven ion sources.

References

1. H. Daido et al., Rep. Prog. Phys. 75, 056401 (2012)
2. C. Danson et al., High Power Laser Sci. Eng. **3**, e3 (2015)
3. J. S. Green et al., Proc. SPIE **8079**, 807919 (2011)
4. J. Metzkes et al., Rev. Sci. Instrum. **87**, 083310 (2016)
5. N. P. Dover et al., Rev. Sci. Instrum. **88**, 073304 (2017)
6. G. F. Knoll, *Radiation Detection and Measurement*, 4th ed. (Wiley, 2000), Vol. 3, p. 860
7. N. Cook et al., J. Instrum. **9**, P09004 (2014)
8. J. F. Ziegler et al., Nucl. Instrum. Meth. B **268**, 1818 (2010)
9. S. Nakamura et al., Jpn. J. Appl. Phys., Part 2 **45**, L913 (2006)
10. K. Zeil et al., Nat. Commun. **3**, 874 (2012)

Effect of target density in laser ion acceleration

Toshimasa Morita

High-Intensity Laser Science Group, Department of Advanced Photon Research

There has recently been much progress in compact laser systems, and laser ion acceleration is a compelling application of high-power compact lasers [1]. If a compact laser system could generate ions with sufficiently high energy, a low-cost compact accelerator would become feasible. However, the ion energies achieved to date are insufficient for some applications. Therefore, it is important to study which conditions are effective for generating ions with higher energies. Herein, we investigate a method to generate higher-energy ions and a high-quality ion beam with minimal energy spread.

Higher-energy protons can be obtained using a "light" material for the target. Herein, "light" denotes small m/q (where m is the ion mass and q is its charge) and "heavy" denotes large m/q. A double-layer target is used because it can generate a high-quality proton beam (Fig. 1(a)) [2]. Carbon is employed as a "light" material for the first layer, and gold is used as a "heavy" material for comparison. Simulations are performed by varying the ion density (i.e., electron density) of the first layer with a fixed areal mass density. To examine the dependence of the achieved proton energy on the target density, we perform 3D and 2D PIC simulations. The number of ions (i.e., electrons) is the same in all cases, even under different densities. We increase the target density by reducing the thickness of the first layer while maintaining the same numbers of ions and electrons (Fig. 1(b)). We use a Gaussian linearly polarized laser pulse that is normally incident on the target. A laser power of 620 TW is focused on to a spot of size 3.2 μm (FWHM), with an intensity of 5×10^{21} W/cm^2, a duration of 27 fs, and a laser energy of 18 J. The target is disk-shaped. The first layer has a diameter of 6.4 μm and its thickness is varied according to density, being 0.4 μm for $30n_{cr}$, 0.15 μm for $80n_{cr}$, etc., where n_{cr} indicates a critical density of 1.7×10^{21} cm^{-3}. The ionization state of each ion in the first layer is assumed to be $Z_i = +6$. The hydrogen layer is narrower and thinner; its diameter is 3.2 μm and thickness is 0.024 μm.

Figure 2 shows the particle distribution and electric field magnitude of the $60n_{cr}$ carbon case in a 3D simulation. After strong interactions with the target, part of the laser pulse is reflected, while another part is transmitted. The carbon ions are distributed over a much wider area by the Coulomb explosion.
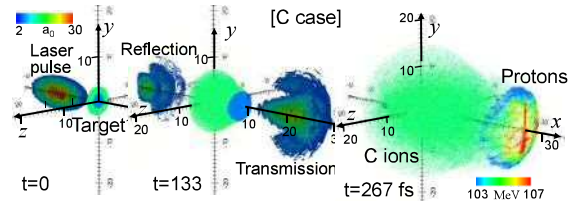
Fig. 2. 3D views of particle (ion) distribution and electric field magnitude for the carbon case.

The maximum proton energy is 110 MeV at $t = 267$ fs.

Figure 3 shows the obtained proton energy, which is normalized by its minimum in the carbon case, namely $\varepsilon/\varepsilon_{C,min}$, as a function of the initial electron density of the first layer, namely n_0/n_{cr}. The obtained proton energy of the carbon case is much higher than that of the gold case. In the carbon case, the proton energy increases dramatically from $30n_{cr}$ to $60n_{cr}$ and is almost flat above $60n_{cr}$. However, in the gold case, there is no such dramatic change in proton energy; instead, it decreases almost monotonically with density.

Figure 4 shows the electric field magnitude and the ion and electron distributions in the $60n_{cr}$ carbon and gold cases at early simulation times. Also shown is the distribution of the electric field magnitude of the reflected laser on the x axis. The head of the reflected laser has almost the same shape and value for both cases. The tail of the reflected laser in the carbon case is shorter than that in the gold case. In the -22 μm $< x$ region, the electric field in the carbon case decreases much more rapidly than that
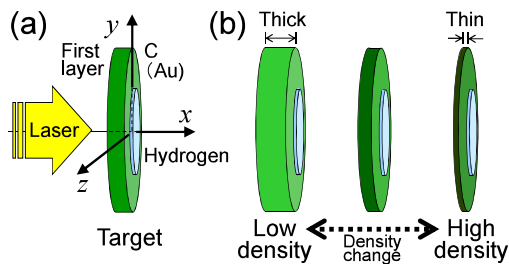
Fig. 1. (a) Laser pulse and target. (b) The ion density of the first layer is changed by adjusting the layer thickness while maintaining the same numbers of ions and electrons.
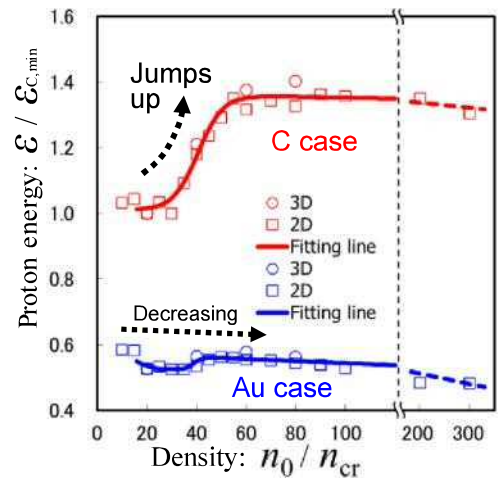
Fig. 3. Proton energy versus initial electron density of the first layer at $t = 267$ fs.
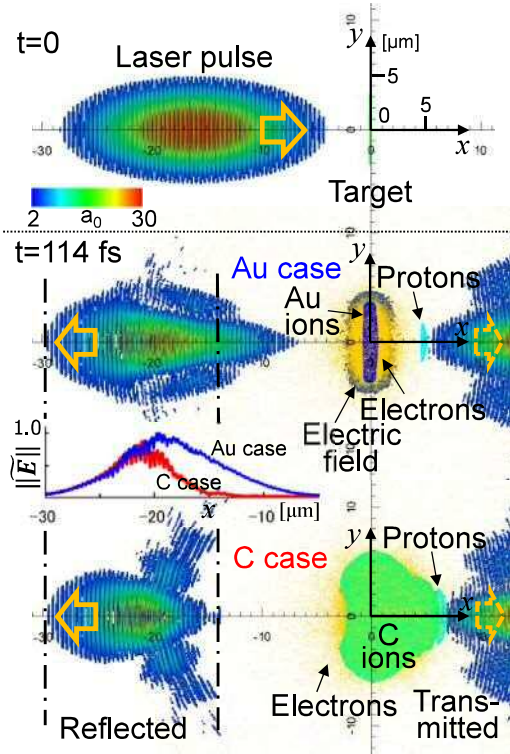
Fig. 4. Spatial distribution of particles (ions and electrons) and electric field magnitude of the $60n_{cr}$ carbon and gold targets in a 3D simulation at t = 0 and 114 fs. A 2D projection of the section at $z = 0$ is shown.

in the gold case and quickly becomes almost zero. The reflected laser energy from the carbon ("light" material) target is much less than that from the gold ("heavy" material) target, even with the same initial densities of electrons and ions. This is one of the reasons why we can obtain high-energy protons from the carbon target; a "light" material target (LMT) experiences strong Coulomb explosions, resulting in it being much thicker than a "heavy" material target (HMT) in the early acceleration stage. This means that the electron density in the LMT becomes much lower than that in the HMT. Therefore, the reflection of the laser pulse decreases and the more laser energy is absorbed in an LMT. With an LMT, the reflected laser energy does not increase with target density above $60n_{cr}$. However, the gold target does not experience such a strong explosion. In an HMT, the reflected laser energy keeps increasing with density, meaning that the energy absorbed in the target decreases continuously.

Therefore, the obtained proton energy decreases with target density.

The carbon target expands strongly in the x direction, and this tendency becomes stronger with higher density. The stronger Coulomb explosion in the x direction generates protons with higher energy. This effect increases along with density, ending only above a certain density, namely $n_0 > 60n_{cr}$ in our conditions. This is one of the reasons for the jump in proton energy and helps to explain the high-energy protons in high-density targets of "light" material.

The other reason for the jump in the obtained proton energy is the radiation pressure acceleration (RPA) behavior. The carbon ion cloud moves in the $+x$ direction. The velocities increase rapidly until around $60n_{cr}$, before becoming almost constant for $n_0 > 60n_{cr}$. This trend is also the same as shown in Fig. 3. However, the gold target does not experience such movement. The carbon-target velocities are much higher than the gold-target ones at all densities. This means that the RPA effect is much higher in the carbon target. In the initial stage of the RPA process, the electrons have almost the same momentum and distribution in the carbon and gold cases because they depend strongly on the laser conditions and the initial electron distribution. Therefore, the electric field working on the ions is almost the same in both cases. The "light" ions then acquire high velocities because they are "light". The RPA behavior is another reason why high-energy protons can be obtained from LMTs, which helps to explain the jump in proton energy in such targets.

The jump in proton energy of the LMT is due to the effect of the strong Coulomb explosion of the first layer and the effective RPA. The laser reflection from the LMT is smaller than that from the HMT. This also helps to explain why the obtained proton energies in the LMT are always higher than those in the HMT. HMTs have small target expansion and RPA effects with a large amount of laser reflection. Therefore, there is no energy jump as in LMTs and the obtained proton energy is low. Materials that can easily become "light" are ideal for the target because they can be almost fully stripped at low energy. It is effective for "lighter" ions to form quickly, before the main part of the laser pulse arrives, meaning an ordinary light material. That is, light materials are more effective than heavy ones for the target to obtain high-energy protons [3].

We have found that the obtained proton energy increases dramatically for a certain density of a light material target. That is, the Coulomb explosion of the target and the RPA act effectively above a certain density. Moreover, the reflection of the laser pulse from the target is small for a light material.

References

1. S. V. Bulanov, *et al.*, Phys. - Usp. **57**, 1149 (2014).
2. T. Esirkepov, *et al.*, Phys. Rev. Lett. **89**, 175003 (2002).
3. T. Morita, Phys. Plasmas **24**, 083104 (2017).

Modeling of ablation and plasma formation from laser-irradiated targets for the simulation of EUV sources

Akira Sasaki

X-ray Laser Group, Department of Advanced Photon Research

Laser-pumped plasma extreme ultra-violet (EUV) light sources have been investigated toward their application to next-generation microlithography.

It has been shown that an intense emission at the EUV wavelength (λ = 13.5 nm) is obtained from Sn ions. In laser-produced plasma with electron temperatures of 20–50 eV, 4 to 14 times ionized Sn with the outermost electron subshell of 4d is produced, which has an intense photo-emission through 4d–4f and 4p–4d unresolved transition arrays (UTAs).[1] The wavelengths of the emission are almost constant over these charge states and several emission lines overlap in the same wavelength region. In lower-density plasmas with an ion density less than 10^{19}/cm^3, the contribution of the satellite lines from the inner shell or multiply excited states decreases, resulting in a narrow emission spectrum. Figure 1 shows the dependence of spectral efficiency on the temperature and ion density of Sn plasmas. The bandwidth (2%) of the EUV source is determined from that of the multilayer optics, and the fraction of usable EUV light for the lithography increases at lower densities.

A low plasma density is also preferable for reducing the effect of opacity, which also causes a broad emission spectrum.[2] To produce low-density plasmas, CO_2 lasers are more suited for the pumping source because of the low critical density.[3]

To reduce the emission of particle debris, small droplets of Sn with a diameter of a few tens of micrometers are used as the targets of the EUV source. These mass-limited targets are expected to be also useful for producing low-density plasmas. However, the absorption of the CO_2 laser light by the droplets is inefficient because the target diameter is smaller than the beam size. Furthermore, the laser light is reflected from the steep density gradient of the plasma, which is produced at the droplet surfaces.

The double-pulse technique required to perform a plasma from the droplet targets is critical for obtaining a high-efficiency EUV source. As shown in Fig. 2, in recent studies, a YAG laser pulse with a duration of a few picoseconds irradiates the droplets to break the targets into particles through the effect of the shock wave. The cloud of particles expands up to 10 times the initial diameter ($\approx$100 µm) and is subsequently irradiated by the main CO_2 laser pulse with a duration of nanoseconds to produce a plasma with ideal density and temperature for EUV emission.

Radiation hydrodynamic simulations are a useful tool for optimizing the EUV source. However, conventional codes are not always applicable to low-temperature conditions when initially solid or liquid material is heated, evaporates to the gas phase, and is then ionized to produce plasma. The solid/liquid-to-gas transition may cause structure formation and particle emission. We have investigated this phenomenon theoretically and developed a hydrodynamic simulation code that takes account of the emission of particle debris from the heated metal targets.[4]

We develop a Lagrangian hydrodynamic simulation code using grid re-organization algorithms, which allows one to place the grid along the distribution of particles and to evaluate the equation of state under the conservation of mass and internal energy.

The application of the Lagrangian hydrodynamics code to the modeling of laser-produced plasma has been limited by the collapse of grids because of the motion of the fluid.[5] We use triangular grids in a two-dimensional geometry and the following grid re-organization algorithms to avoid collapse. As shown in Fig. 3(a,b), when the aspect ratio (i.e., the ratio of the cell height to the cell base) becomes too small or the cell becomes too flat, the cell is split, conserving its mass and internal energy. By contrast, if the ratio becomes too large or two grid points become too close, these points are merged and the cells are united.
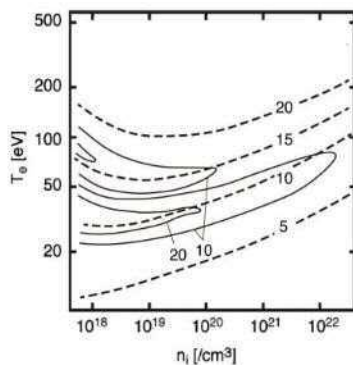

Fig. 1. Density and temperature dependence of spectral efficiency (solid line), which is defined by the fraction of in-band emission into 2% bandwidth at l = 13.5 nm from total emission, and averaged charge (dotted line) of Sn plasma.
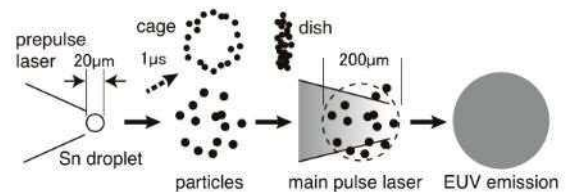

Fig. 2. Schematic of the excitation of the LPP EUV source based on the double-pulse technique.
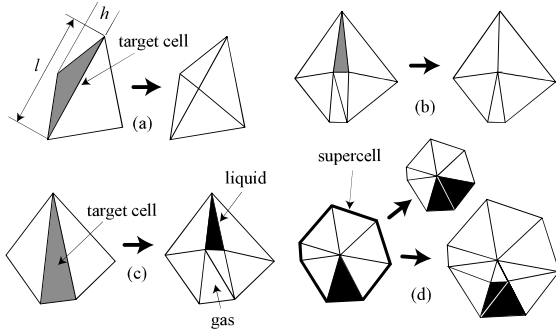
Fig. 3. Algorithms for re-organizing a grid by (a) splitting cells and (b) uniting cells. Methods to take liquid-to-gas transition by (c) splitting cells and (d) redistributing mass and internal energy are also shown.
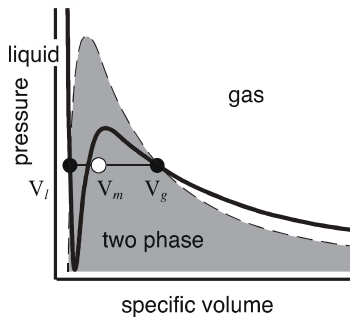

Fig. 4. Pressure and specific volume of material according to Van der Waals equation of state. Gray area indicates two-phase region.

Fig. 5. Temporal evolution of the density distribution of heated Sn cylinder for the heating rates of (a) 2.5 and (b) 6 $\times 10^{12}$ W/mol.

Formation of gas bubbles in the liquid phase, as well as formation of liquid clusters in the gas phase through phase transition, is modeled by splitting the target cell. The algorithms are shown schematically in Fig. 3(c,d).

We use the Van der Waals equation of state of Sn[6] which determines the phase of the material for a given temperature and density, as shown in Fig. 4. The equation of state shows the two-phase region where the material is unstable as a uniform state and split into separate liquid and gas regions with a void ratio, which is determined as a function of temperature and density. In the present model, if the conditions of the target cell are found to be those for a two-phase region, the cell is split to produce separate liquid and gas cells. This forms a group of cells that conforms to a super-cell. Subsequently, the mass and internal energy of the target cell are redistributed to each cell to ensure the correct void ratio for the super-cell. Note that the temperature changes after the transition, which corresponds to the effect of latent heat, which arises from the difference in the internal energy between the liquid and gas phases. We use the method of time splitting, in which the hydrodynamic motion and re-organization of the grids are performed alternately for each time step.

We perform test calculations using the present code, whose results are shown in Fig. 5. We calculate the temporal evolution of the temperature and density of the cylindrical Sn target, heated uniformly at a fixed rate. Initially, the target is in the liquid phase, which evaporates into the gas phase. As shown in Fig. 5(a), for a moderate heating rate, the target expands through the two-phase region, showing that the initial small expansion causes the formation of bubbles inside the target, which grow in size and eventually break the target into particles. By contrast, for a large heating rate, because the temperature immediately exceeds the critical temperature ($\approx 7,000$ K), the target expands uniformly without forming particles, as shown in Fig. 5(b).

The present model will be used to analyze the EUV source after further validations. Firstly, calculation of the particle formation due to the shock wave, which is driven by short, pre-pulse laser irradiation, will be carried out[7]. Secondly, calculation will be extended to include the interaction between particles and the main laser pulse. Recently, the spatial distribution of density and temperature after the pre-pulse laser irradiation has been investigated.[8] Comparisons with these experiments will improve our understanding of the mechanism of excitation of the Sn plasmas, which will be useful for further optimization of the EUV source.

Refernces

1. G. O′Sullivan, et al. J. Phys. **B48**, 144025 (2015).
2. A. Sasaki, et al. J. Appl. Phys. **107**, 113303 (2010).
3. K. Nishihara, et al. Phys. Plasmas **15**, 056708 (2008).
4. A. Sasaki, et al. AIP Advances **7**, 095005 (2017).
5. R. Ramis, et al. Comput. Phys. Commun. **180**, 977 (2007).
6. D. A. Young, Phys. Rev. **A3**, 361 (1971).
7. D. Kurilovich, et al. Proc. 2017 EUV Source Workshop (https://www.euvlitho.com).
8. K.Tomita, et al. Appl. Phys. Express **8**, 126101 (2015).

Mo/Si multilayer-coated photodiode-based X-ray laser intensity monitor and its application to polarization analysis

Takashi Imazono

X-ray Laser Group, Department of Advanced Photon Research

The laser-driven plasma soft X-ray laser (XRL) system at the Kansai Photon Science Institute, QST, provides 13.9 nm coherent radiation with a monochromaticity of 10^{-4} and a pulse duration of 7 ps, and has been used for various applications.[1,2] To meet the increasing requirements for coherent pulsed beams, it is beneficial to determine the beam characteristics, especially the shot-to-shot beam intensity. The number of photons per pulse depends mainly on the excitation conditions of the pumping laser, and therefore, is quite sensitive to the gain of the lasing medium. A slight gain fluctuation leads to a large intensity variation, thereby indicating that a real-time beam-intensity monitor (BIM) is indispensable for quantitative XRL applications such as reflectivity and polarization measurements and pump-probe techniques.

Amplitude-division beam splitters such as free-standing and membrane-supported multilayer films have been used frequently as beam-intensity monitoring techniques at around 13.9 nm. The transmitted light for downstream experiments can be used without changing the direction of the optical axis, but there are several difficulties in fabrication process and operation of amplitude-division beam splitters, such as those resulting from membrane rigidity, roughness, uniformity, and absorption.[3] Besides, reflection mirrors can be used as wavefront-division beam splitters, but the intensity distribution and pointing stability of an incoming beam strongly affect the susceptibility. Alternatively, photoionization-based gas detectors have a wide dynamic range and can be used effectively in the EUV range without changing the optical axis.[4] However, they are unsuitable for use in the spectral regions in which the target rare gas has strong resonance. Furthermore, the installation and/or use would be restricted because of differential pumping.

The AXUV series of photodiodes (OptoDiode), commercially available silicon p-n junction photodiode detectors for EVU and X-ray radiation, are made of polished silicon, and some of them have an active area coated with a bandpass filter to filter out radiation outside a specific range, e.g., Si/Zr for the 11–18 nm range. Meanwhile, an AXUV photodiode coated with a well-designed Mo/B$_4$C/Si multilayer has been reported to show a high reflectivity of 69.9% and work as a good polarizer at a wavelength of 13.5 nm and 45° incidence.[5] Unfortunately, its use as a BIM has not been discussed explicitly. If a well-designed multilayer-coated photodiode shows high correlation between the reflected intensity and generated photodiode current at a wavelength of 13.9 nm, it should be possible to monitor the incident and reflected intensities from shot to shot. This type of BIM changes the direction of the optical axis but makes it possible to avoid the problems of amplitude- and wavefront-division beam splitters and can be installed easily anywhere in a beamline, even immediately in front of the samples.

To develop a reflection-type multilayer-coated photodiode for XRL, we prepared two identical AXUV100G photodiodes with an unfiltered active area of 10×10 mm^2. One of the photodiodes was coated with a Mo/Si multilayer by ion-beam sputtering; the parameters were determined to be a multilayer period of 10.36 nm and Mo thickness ratio of 0.34 by grazing-incidence X-ray reflectivity using Cu $K\alpha$ radiation.[6] The other photodiode was used without coating for detecting the reflected light from the MP in synchrotron radiation (SR) and XRL measurements.

The MP was characterized using SR from 12.5 to 15.2 nm. At 13.9 nm, the reflectance R of the MP tilted at an angle of incidence of 45° was measured to be 52.5%, where R is defined as the ratio of the reflected beam intensity I_{OP} from the MP to the beam intensity measured when the MP is removed from the beam path. Note that both intensities have been measured with the OP irradiated at normal incidence.[7] Meanwhile, the relative transmittance T has been measured to be 8.96%,[7] where the definition is slightly different from conventional ones and is the ratio of the 45°-tilted MP signal, I_{MP}, to a normal incident signal. Consequently, we obtain $R/T = 5.86$ and the sensitivity correction factor as $\alpha = 2.91$, resulting from the difference between the respective independent photodiodes, in addition to the complete correlation between reflection and transmission intensities.[7] It seems reasonable that the incoming beam to the photodiodes is absorbed almost completely and used to generate the photodiode currents proportional to the incident light intensity because the reflections from the MP and OP at normal incidence are negligible, being below 10^{-4}. Therefore, I_{OP} can be calibrated using R, T, α, and I_{MP} as

$$I_{OP} = (R/T)\,\alpha\,I_{MP}. \tag{1}$$

This indicates that the beam intensity can be monitored by measuring I_{MP} from shot to shot. Thus, MP performs well as a BIM that can deliver a high-intensity beam for application experiments.

Polarization analysis of XRL beams in single-target mode was performed using a six-axis soft X-ray ellipsometer installed at an end station of the XRL beamline.[6] XRL beams were irradiated onto the MP active area and then reached the OP via a Mo/Si multilayer polarizing mirror (mirror A). The s- and p-polarization reflectances of A were determined with SR in advance, resulting in 54.5% and 2%, respectively, at an angle of incidence of 42.75°.[6-8] Another plane mirror M2 of an unknown reflectivity R_x was placed between MP and A.

Figure 1(a) shows a plot of I_{OP} versus I_{MP} for 23 successive shots, measured in the experimental configuration in which A is removed from the optical path, as illustrated in the inset. The correlation coefficient between I_{OP} and I_{MP} is 0.965. Taking account of the reflectivity R_x of M2 placed between MP and OP, Eq. (1) is modified as

$$I_{OP} = 17.1\,R_x\,I_{MP}. \tag{2}$$

Substituting the measured I_{OP} and I_{MP} into Eq. (2), R_x can be evaluated from shot to shot, as shown in Fig. 1(b). The averaged reflectance is 0.568 ± 0.048, which is as high as that of A and a reasonable value because the multilayer coatings of A and M2 have been deposited in the same manner. Fig. 1(c) shows a SR and XRL; the XRL data agree well with the SR ones.[6] The correlation coefficient between I_{OP} and I_{MP} exceeds 0.960 comparison of the s-polarized reflectivities of A measured with
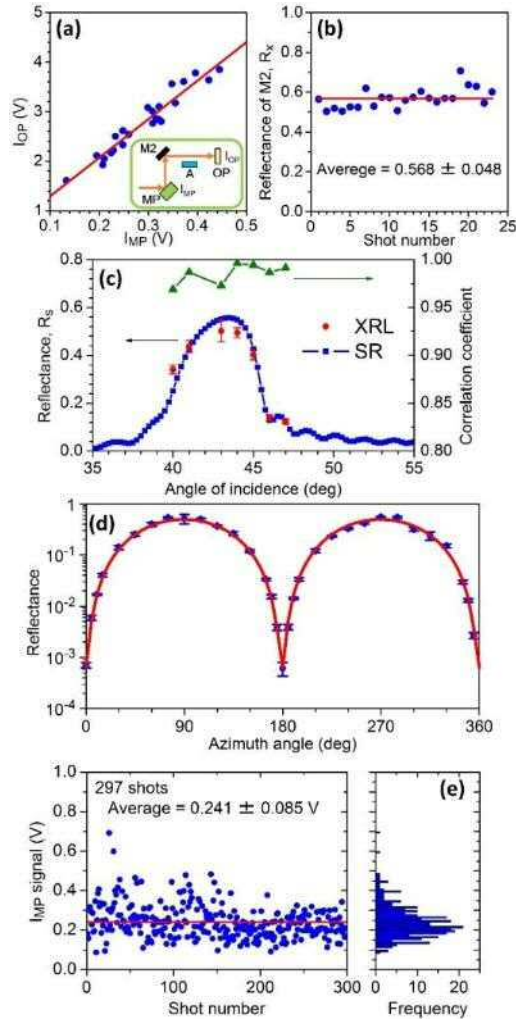
Fig. 1. (a) Plot of IOP versus IMP for 23 shots, measured in the configuration shown in the inset. (b) Plot of Rx of M2 versus shot number. (c) Comparison of measured reflectivities of A with XRL and SR on the left-hand axis and the correlation coefficient between IOP and IMP at each data point on the right-hand axis. (d) Measured reflectance of A as a function of azimuth angle. (e) Plot of IMP against shot number. The XRL energy conversion factor evaluated from IMP corresponds to roughly 6 nJ/V.[7]

(plotted on the right-hand axis). These results imply that the MP acts as a satisfactory BIM and enables absolute measurements with XRL. Figure 1(d) shows the reflectance of A plotted as a function of azimuth angle. By applying curve fitting to the sinusoidal data, we find that the XRL beam incident to A is perfectly linearly polarized with the polarization plane tilted slightly from the vertical direction, and that the polarization state at the end station is stable because of reflections by mirrors such as M2 on the beam path. Figure 1(e) shows the XRL beam-intensity stability, plotted using the I_{MP} of 297 shots taken from the measurements in Fig. 1(c) and (d). Despite a large root-mean-square (rms) variation of 35%, quantitative polarization analysis can be performed successfully by means of the MP. The dark noise from the MP is negligible at below 0.2% rms with respect to the average MP signal. The large fluctuation is therefore considered to be caused mainly by the concentration fluctuation of the plasma at the source point and the shot-by-shot fluctuation of the pumping energy, in addition to the horizontal beam profile of the XRL output at the lasing medium.[9] This indicates the importance of monitoring the beam intensity in real time during the experiments.

In conclusion, we have succeeded in developing an excellent XRL BIM by means of a Mo/Si multilayer-coated photodiode detector, enabling the delivery of a high-intensity beam to downstream experiments such as polarization analysis.[7] We hope that our beam-intensity monitoring technique will be used widely in the time-resolved morphology of single- or multiple-shot laser ablation.

References

1. R. Z. Tai et al., *Phys. Rev. Lett.* **89**, 257602 (2002).
2. A. Y. Faenov et al., *Appl. Phys. Lett.* **94**, 231107 (2009).
3. R. Sobierajski et al., *J. Synchr. Rad.* **20**, 249−257 (2013).
4. K. Tiedtke et al., *J. Appl. Phys.* **103**, 094511 (2008).
5. B. Kjornrattanawanich et al., *Appl. Opt.* **43**, 1082−1090 (2004).
6. T. Imazono et al., *Thin Solid Films* **571**, 513−516 (2014).
7. T. Imazono, *Appl. Opt.* **56**, 5824−5829 (2017).
8. T. Imazono et al., *Rev. Sci. Instrum.* **80**, 085109 (2009).
9. T. Kawachi et al., *Phys. Rev. A* **66**, 033815 (2002).

4 J, 50 Hz Nd:YAG laser system for transportable remote-sensing system

Katsuhiro Mikami

X-ray Laser Group, Department of Advanced Photon Research

A new laser remote-sensing (LRS) system for inspecting social infrastructure constructions such as tunnels has been demonstrated.[1,2] Laser hammering is an LRS procedure that can replace the hammer impact test for detecting defects inside concrete. The basic idea behind LRS is that a high-energy pulse of an impact laser system is irradiated on the concrete surface to generate panel vibrations by laser ablation and/or thermal stress, thereby acting as a hammer. After that, a laser interferometer detects the generated vibrations in the audible range, similar to the human ear. In recent years, we have demonstrated LRS (in the laboratory) using a laser system with a pulse energy of 1 J and a repetition rate of 25 Hz.[3] The pulse energy of the impact laser should be increased to detect deeper and wider defects; this would also improve the signal-to-noise ratio in the LRS results because it would prevent noise being generated upon ablation. A higher repetition rate of the impact laser would also be an improvement because it would increase the LRS inspection speed. Figure 1 shows the distribution of the developed and commercial high-average-power laser systems currently in operation. For LRS, the output characteristics of the high-average-power laser system must exceed those demonstrated previously and fall within the shaded area in Fig. 1. Furthermore, the laser system should be able to operate under tough outdoor conditions and be suitable for commercial use. Therefore, it is important for the impact laser to combine environmental stability, compactable layout, and low cost.

The laser-irradiated medium should be cooled to prevent its thermal destruction when operating with high-average-power output; therefore, its temperature distribution is generated naturally using the cooling and pumping schemes. The thermal effects caused by the temperature distribution lead to distortion of the wavefront of the laser pulse, such as the thermal lens effect,[4] and generate undesired effects in primary processes for which the laser phase is essential, e.g., focusing, propagation, and wavelength conversion. Most laser systems with an average power output of over 100 W are realized with special phase controllers such as a stimulated Brillouin scattering phase-conjugating mirror (SBS-PCM)[5,6] or a cryogenic system,[7] as shown in Fig. 1. Both advanced techniques are solutions for wavefront distortion by the thermal lens effect, but have some drawbacks for operation in outdoor conditions, in particular, large size and temperature control. In fact, an SBS-PCM requires a seed injection system to obtain a single longitudinal mode, while a cryogenic system requires various equipment and electrical power.

In this study, we developed an Nd:YAG laser system based on a master-oscillator power amplifier (MOPA) platform with a compact layout. LRS requires a simple and tough laser system with an adequate laser output. A commercial high-average-power Q-switched Nd:YAG laser (Litron Lasers, LPY742-100) was adapted as the master oscillator on an MOPA platform to downsize the amplifier stages. A single longitudinal mode was not required in the impact laser system because an SBS-PCM was not employed. Hence, a multi-longitudinal mode was adopted to achieve a low-cost master-oscillator system. Figure 2 shows the optical layout of the developed laser system. The wavelength and pulse width of the master oscillator were 1,064 nm and 14 ns,

respectively. The pulses of the master oscillator were amplified with two 1.1 at% doped Nd:YAG rods pumped by flash lamps operating at 50 Hz. The Nd:YAG rods were 14 mm in diameter and 70 mm in length. The equal-sized Nd:YAG rods provided the same thermal effects and fluorescence spectra, allowing the components for thermal compensation to be simplified. However, the stored energy in the Nd:YAG rods could not be extracted sufficiently with a single pass of the master-oscillator pulse; therefore, a double-pass scheme was used for the first Nd:YAG rod amplifier. A design of the high power laser system considered for thermal-optical effect is important to prevent thermal lens effects in the amplifier rods. In the developed laser system, we installed pairs of lenses at the ends of the vacuum tubes to act as an image transfer tube(A to D in Fig. 2). The distance between each pair of lenses was adjusted with a translation stage to collimate the beam and correct the divergence that occurred because of the thermal lens effect. The size of the constructed laser system was 4.0 m × 0.8 m, including the master oscillator.

Figure 3 shows the input–output characteristics after single- and double-pass amplification by the first rod and amplification by the second rod for an input laser beam diameter of 13 mm. In Fig. 3, the symbols represent measured values and the solid lines are theoretical values estimated using the Frantz–Nodvik
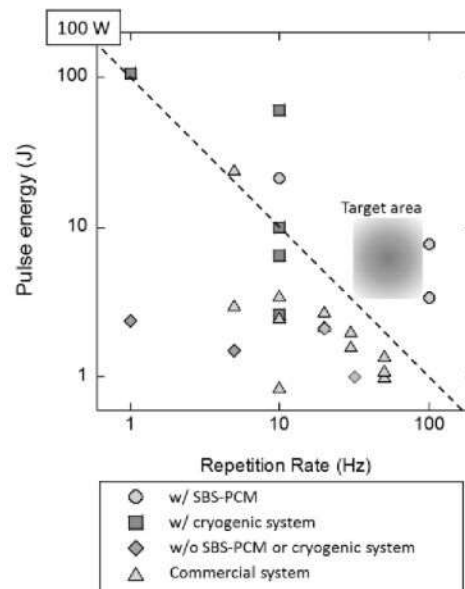

Fig. 1. Distribution of developed and commercial high-average-power laser systems currently in operation, in terms of their pulse energy and repetition rate. Most laser systems with an output over 100 W incorporate special phase controllers such as SBS-PCM (circle) and cryogenic systems (squares). The shaded area indicates the output characteristics required for LRS.
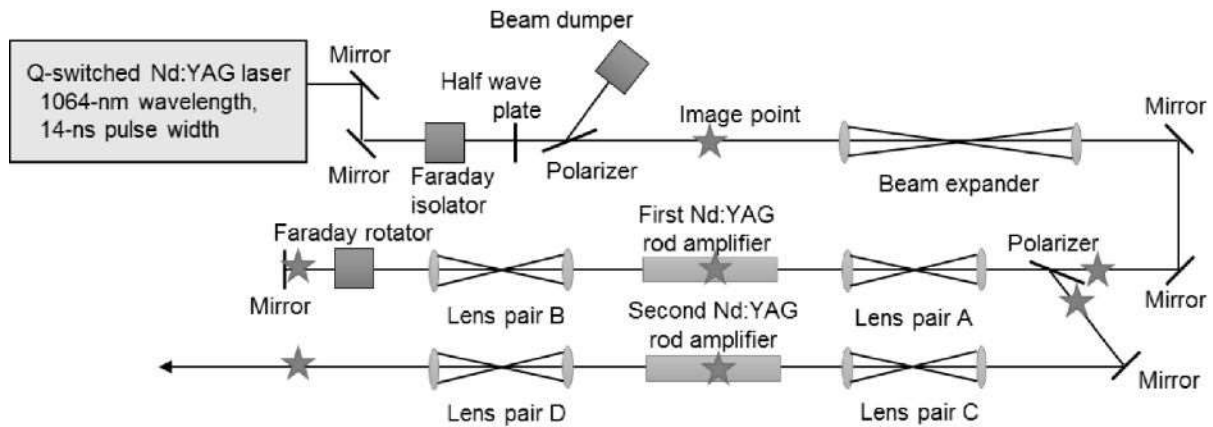
Fig. 2. Optical layout of the developed laser system. The stars represent image points.
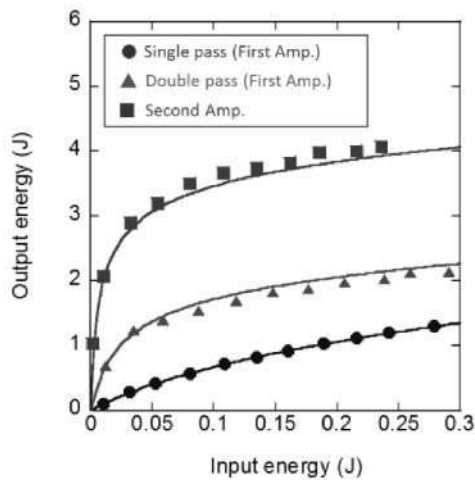
Fig. 3. Input–output characteristics of the developed laser system after single- and double-pass amplification by the first rod and amplification by the second rod. The symbols represent measured values and the solid lines are theoretical values estimated using the Frantz–Nodvik formula.

formula,[8] assuming a saturation fluence of 0.622 J/cm² for the Nd:YAG rod as a fitting parameter. The maximum value obtained for the output energy was 4.06 J with an operating frequency of 50 Hz. The measured output energies showed good agreement with the theoretical values, so the ASE could be neglected. Furthermore, thermal birefringence was cancelled appropriately in the double-pass amplification scheme. Saturation amplification was achieved after the double-pass scheme in the LRS laser system, but wavefront distortion led to undesired focusing characteristics. In the case of focusing with a simple lens with f = 687 mm, the beam profile at the beam waist showed that an energy of 2.13 J was obtained. Moreover, the double-pass scheme in the first rod achieved full extraction of the stored energy during the amplification. The focusing characteristics are an essential parameter adequate laser irradiation on the concrete surface, and roughly 97% of the pulse energy was transferred successfully in an area twice that of the beam waist. The total electrical energy needed to run the system was roughly 20 kWh, which can be provided by a diesel generator or some storage batteries. A 20 kWh air-cooling system is also available. Therefore, the developed LRS system will provide standalone behavior without untransportable equipment in outdoor conditions.

References

1. M. Sinoda, H. Omura, N. Misaki, Y. Shimada, and S. Uchida, RTRI Report 23, 29 (2009) [in Japanese].
2. S. Kurahashi, O. Kotyaev, Y. Shimada, and T. Norimatsu, Rev. Laser Eng. 42, 849-853 (2014) [in Japanese].
3. S. Kurahashi, K. Mikami, T. Kitamura, N. Hasegawa, H. Okada, S. Kondo, M. Nishikino, T. Kawachi, and Y. Shimada, J. Appl. Remote Sens. [Accepted].
4. J. D. Foster and L. M. Osterink, J. Appl. Phys. 41, 3656 (1970).
5. R. Yasuhara, T. Kawashima, T. Sekine, T. Kurita, T. Ikegawa, O. Matsumoto, M. Miyamoto, H. Kan, H. Yoshida, J. Kawanaka, M. Nakatsuka, N. Miyanaga, Y. Izawa, and T. Kanabe, Opt. Lett. 33, 1711 (2008).
6. T. Hatae, E. Yatsuka, T. Hayashi, H. Yoshida, T. Ono, and Y. Kusama, Rev. Sci. Inst., 83, 10E344 (2012).
7. S. Banerjee, P. D. Mason, K. Ertel, P. J. Phillips, M. De Vido, O. Chekhlov, M. Divoky, J. Pilar, J. Smith, T. Butcher, A. Lintern, S. Tomlinson, W. Shaikh, C. Hooker, A. Lucianetti, C. Hernandez-Gomez, T. Mocek, C. Edwards, and J. L. Collier, Opt. Lett. 41, 2089 (2016).
8. L. M. Frantz and J. S. Nodvik, J. Appl. Phys. 34, 2346 (1963).

Deformation of a Molecular Orbital in Ethanol Induced by an Intense Laser Field

Hiroshi Akagi, Tomohito Otobe and Ryuji Itakura

Ultrafast Dynamics Group, Department of Advanced Photon Research

In laser fields with intensities as high as 10^{14} W/cm^2, molecules are ionized through electron tunneling. It is understood that the tunnel ionization depends on the spatial density distribution and binding energy of the molecular orbital (MO) from which an electron is ejected. This is based on the angular dependence of the ionization probability measured for diatomic or triatomic molecules [1–5]. Recently, it has been suggested that MOs in molecules larger than the triatomic ones are deformed by laser electric fields [6,7]. As the molecular size increases, the energy spacing between MOs decreases, leading to strong interactions among MOs in laser electric fields.

In the present study, we derive the molecular frame photoelectron angular distribution (MFPAD) of the dissociative ionization of ethanol (CH$_3$CD$_2$OH) in an intense near-infrared laser field ($I_0 \approx 8 \times 10^{13}$ W/cm^2, $\lambda \approx 800$ nm). The energy levels from HOMO-1 to HOMO-4 are close in a small energy range of 3 eV. Additionally, photoelectron-photoion coincidence measurement with He(I) at 21.2 eV showed that electron ejection from different MOs results in different fragment ions [8]. Therefore, identifying the fragment ion allows us to identify the MO from which the electron was ejected.

In our experiment, we use a partially deuterated CH$_3$CD$_2$OH sample to avoid producing different fragment ions with the same mass. The vaporized sample is introduced in an ultrahigh-vacuum chamber through a micro-syringe [9], and the molecular effusive beam is irradiated with a circularly polarized laser pulse, which singly ionizes an unaligned molecule. A linearly polarized femtosecond laser pulse from Ti:Sapphire regenerative and multi-pass amplifiers ($\Delta\tau \approx 60$ fs, 1 kHz) is converted into a circularly polarized pulse by passing through a quarter-wave plate. The photoelectron drifts perpendicular to the laser electric field at the moment of ionization [3,4]. The recoil direction of a fragment ion reflects the orientation of the parent molecule. We detect an electron and a fragment ion in coincidence with two position-sensitive detectors to determine the angle between their recoil vectors. MFPADs are derived by taking account of the electron drift.

Figures 1A and B show the MFPADs of the CD$_2$OH$^+$ and CH$_3$CD$_2^+$ production channels, respectively. The CD$_2$OH$^+$ channel shows preferential electron ejection from the CH$_3$ side of CH$_3$CD$_2$OH (Fig. 1A), whereas the MFPAD of the CH$_3$CD$_2^+$ production channel is almost isotropic (Fig. 1B). A previous measurement using He(I) suggested that (i) CD$_2$OH$^+$ is produced from the first electronically excited state of the parent
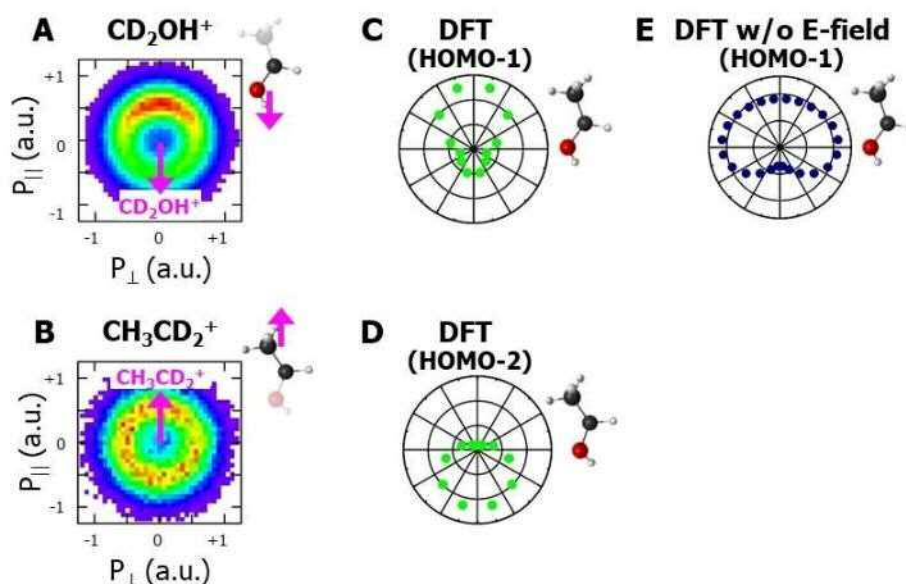

Fig. 1. (A and B) Electron momentum distribution in the molecular frame for the CD$_2$OH$^+$ and the CH$_3$CD$_2^+$ channels, respectively. (C and D) Simulated MFPADs of HOMO-1 and HOMO-2 in a static electric field. (E) Simulated MFPAD of HOMO-1 without the influence of the electric field. The simulated results are convoluted with the experimental angular uncertainty (±45°).

$CH_3CD_2OH^+$ ion and (ii) $CH_3CD_2^+$ is produced from the second excited state of $CH_3CD_2OH^+$ [8]. Therefore, the MFPADs of the CD_2OH^+ and $CH_3CD_2^+$ channels correspond to the electron ejection from HOMO-1 and HOMO-2, respectively.

We simulate the angular dependence of the tunnel ionization rate and compare it with the experimental results. We use density functional theory (DFT) with the KLI-SIC potential, which reproduces the HOMO binding energy. We solve the complex eigen-energy of the Kohn–Sham Hamiltonian under a static electric field and absorbing potential far outside the molecule. The tunnel ionization rate is obtained from the imaginary part of the Gamow state eigenvalue [10]. Figures 1C and D show the simulated MFPADs for HOMO-1 and HOMO-2, respectively. The simulated HOMO-1 MFPAD (Fig. 1C) shows preferential electron tunneling in the direction along the CH_3 recoil and agrees reasonably with the measured one for the CD_2OH^+ channel (Fig. 1A). Our simulations do not reproduce the measured HOMO-1 MFPAD unless we account for MO deformation in the electric field. Figure 1E shows the MFPAD for the field-free HOMO-1 from which the MO deformation is excluded. The MFPAD for the field-free HOMO-1 shows preferential tunneling in the lateral direction with respect to the CD_2OH^+ recoil direction (Fig. 1E). This discrepancy suggests that HOMO-1 deformation is needed to explain the preferential electron ejection from the CH_3 side derived in the measured MFPAD of the CD_2OH^+ channel.

For HOMO-2, the simulation indicates that the electron is ejected preferentially from the OH side (Fig. 1D). However, the measured MFPAD for the $CH_3CD_2^+$ channel is almost isotropic (Fig. 1B). In the intense laser field, the second electronically excited state of $CH_3CD_2OH^+$ can be produced by not only electron ejection from HOMO-2 but also from HOMO or HOMO-1 followed by the electronic excitation of $CH_3CD_2OH^+$ to the second electronically excited state [9]. The isotropic MFPAD suggests that the stepwise channels contribute comparatively to the ionization to form the second excited state of $CH_3CD_2OH^+$, which has a hole in HOMO-2.

In summary, we measure MFPADs of dissociative ionization channels of ethanol CH_3CD_2OH in a circularly polarized laser field with an intensity of $I_0 \approx 8 \times 10^{13}$ W/cm^2. The MFPAD of the CD_2OH^+ channel shows reasonable agreement with the simulated MFPAD for HOMO-1. Our DFT simulations reveal that HOMO-1 is deformed appreciably by the laser electric field. The measured isotropic MFPAD of the $CH_3CD_2^+$ channel cannot be reproduced by the simulated MFPAD for HOMO-2, suggesting that the electronic excitation following the electron ejection from HOMO and HOMO-1 takes place significantly.

References

1. A. S. Alnaser, S. Voss, X. -M. Tong, C.M. Maharjan, P. Ranitovic, B. Ulrich, T. Osipov, B. Shan, Z. Chang, and C. L. Cocke, "Effects of molecular structure on ion disintegration patterns in ionization of O_2 and N_2 by short laser pulses," Phys. Rev. Lett. **93**, 113003 (2004).
2. D. Pavičić, K.F. Lee, D.M. Rayner, P.B. Corkum, and D.M. Villeneuve, "Direct measurement of the angular dependence of ionization for N_2, O_2, and CO_2 in intense laser fields," Phys. Rev. Lett. **98**, 243001 (2007).
3. A. Staudte, S. Patchkovskii, D. Pavičić, H. Akagi, O. Smirnova, D. Zeidler, M. Meckel, D. M. Villeneuve, R. Dörner, M. Y. Ivanov, and P. B. Corkum, "Angular tunneling ionization probability of fixed-in-space H_2 molecules in intense laser pulses," Phys. Rev. Lett. **102**, 033004 (2009).
4. H. Akagi, T. Otobe, A. Staudte, A. Shiner, F. Turner, R. Dörner, D. M. Villeneuve, and P. B. Corkum, "Laser tunnel ionization from multiple orbitals in HCl," Science **325**, 1364, (2009).
5. L. Holmegaard, J. L. Hansen, L. Kalhøj, S. L. Kragh, H. Stapelfeldt, F. Filsinger, J. Küpper, G. Meijer, D. Dimitrovski, M. Abu-samha, C. P. J. Martiny, and L. B. Madsen, "Photoelectron angular distributions from strong-field ionization of oriented molecules," Nature Phys. **6**, 428 (2010).
6. P. M. Kraus, B. Mignolet, D. Baykusheva, A. Rupenyan, L. Horný, E. F. Penka, G. Grassi, O. I. Tolstikhin, J. Schneider, F. Jensen, L. B. Madsen, A. D. Bandrauk, F. Remacle, and H. J. Wörner, "Measurement and laser control of attosecond charge migration in ionized iodoacetylene," Science **350**, 790 (2015).
7. B. Jochim, R. Siemering, M. Zohrabi, O. Voznyuk, J. B. Mahowald, D. G. Schmitz, K. J. Betsch, B. Berry, T. Severt, N. G. Kling, T. G. Burwitz, K. D. Carnes, M. F. Kling, I. Ben-Itzhak, E. Wells, and R. de Vivie-Riedle, "The importance of Rydberg orbitals in dissociative ionization of small hydrocarbon molecules in intense laser fields," Sci. Rep. **7**, 4441 (2017).
8. Y. Niwa, T. Nishimura, and T. Tsuchiya, "Ionic dissociation of ethanol studied by photoelectron-photoion coincidence spectroscopy," Int. J. Mass. Spectrom. Ion. Phys. **42**, 91 (1982).
9. K. Hosaka, A. Yokoyama, K. Yamanouchi, and R. Itakura, "Correlation between a photoelectron and a fragment ion in dissociative ionization of ethanol in intense near-infrared laser fields," J. Chem. Phys. **138**, 104301 (2013).
10. T. Otobe, K. Yabana, and J.-I. Iwata, "First-principles calculations for the tunnel ionization rate of atoms and molecules," Phys. Rev. A **69**, 053404 (2004).

High-speed measurement of terahertz waveforms using a 100 kHz Yb-doped fiber laser for terahertz imaging

Masaaki Tsubouchi and Keisuke Nagashima

Ultrafast Dynamics Group, Department of Advanced Photon Research

Terahertz (THz) light has been used to inspect semiconductor devices, security, biological tissues, and other applications. THz light with low photon energy allows non-destructive and non-invasive probes to be used for these inspections without influencing the molecular structure and electronic properties. THz time-domain spectroscopy (THz-TDS) has been used widely as a sensitive and accurate method to observe THz spectra. This method has already been applied to two-dimensional THz imaging [1] and time-of-flight THz tomography [2] as an inspection tool.

To realize THz imaging as a practical tool, the acquisition speed of THz imaging systems must be increased by two to three orders of magnitude, as suggested in the 2017 THz science and technology roadmap [3]. In this study, we demonstrate the high-speed measurement of THz waveforms to improve the acquisition speed of THz imaging. First, we develop a laser system to generate intense THz pulses with a repetition rate of 100 kHz. Second, we construct a system for high-speed measurement of THz waveforms with the measurement time of 10 ms.

To achieve high-speed THz waveform measurement for practical use, we develop a compact system to generate intense and short THz pulses with high-repetition rate. Intense THz pulses allow us to measure samples with high absorbance into depth. The short THz pulses allow us to measure the thickness of thin films with high resolution.

To generate intense THz pulses, optical rectification in an $LiNbO_3$ (LN) crystal pumped by near-IR light with a tilted pulse front is commonly used [4]. Calculations suggest that near-IR pump light with a pulse width of around 350 fs (transform limited: TL) is best for effective THz light generation in this method [5]. Then, we develop a Yb-doped fiber laser system to generate pump light with a repetition rate of 100 kHz, a pulse width of 320 fs, and a pulse energy of 28 μJ, as shown in Fig. 1. To avoid enhancing the amplified spontaneous emission in the fibers, we divide the amplification process into six stages.

The output light from the Yb fiber amplifier is introduced into the small-tip device (16×20 mm^2) proposed in our previous paper [6]. In the conventional method, the pump pulse front is tilted by a diffraction grating and imaged onto an LN prism to obtain an intense THz output. Our device uses a "contact grating setup" in which the diffraction grating is placed in contact with the input surface of the LN substrate, thereby downsizing the THz light source drastically. Figure 2(a) shows the THz waveform obtained from the contact-grating device pumped by a parallel beam of 4 mm in diameter and 13 μJ. The peak electric field is around 1 kV/cm. The Fourier-transformed spectrum (Fig. 2(b)) shows a peak frequency of 0.6 THz and a bandwidth of 1.5 THz.

The slow acquisition speed in THz-TDS is due to scanning the optical delay line to obtain the temporal profile of the electric field, as shown Fig. 2(a). To overcome this problem, we place a retroreflector on a speaker diaphragm vibrating at 50 Hz to scan the optical delay quickly (Fig. 3). We can measure a single waveform with a scanning time range of 15 ps (Fig. 2(a)) by a measurement time of 10 ms, which is 10^4 times shorter than the time required in the conventional method using the stepping scan. The 100 kHz laser system provides 1,000 data points during 10 ms, and therefore, the time interval between the data points is 15 fs. As described above, we realize a high-speed measurement system for THz waveforms with intense THz light. In the near future, we will realize high-speed THz imaging by using the system presented herein.
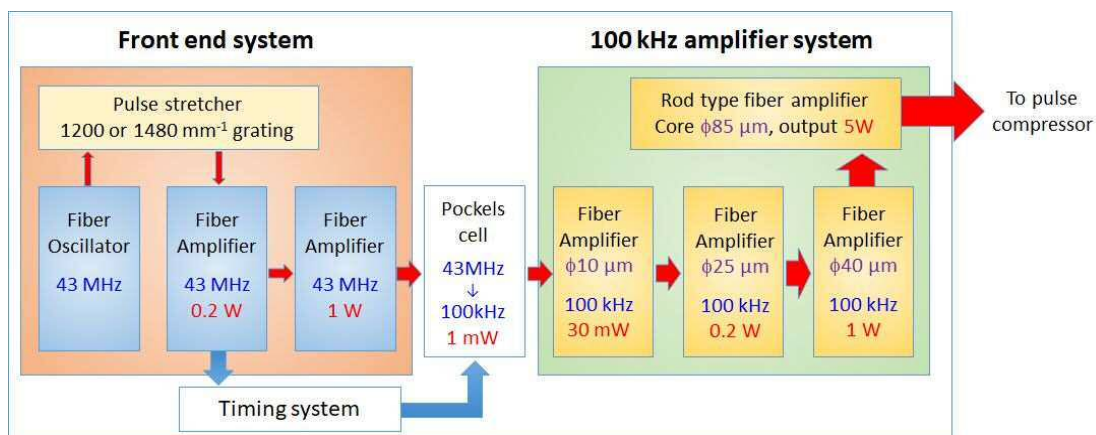
Fig. 1. Diagram of fiber laser system for THz light generation.
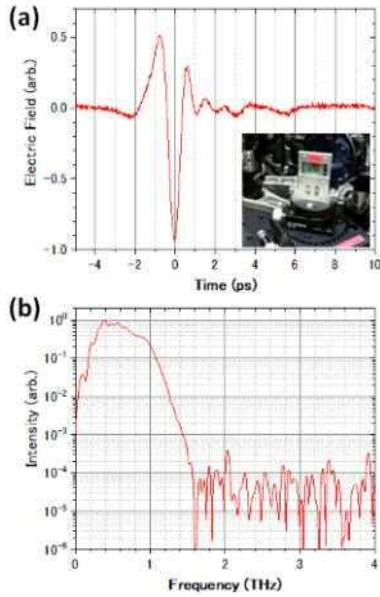
Fig. 2. (a) THz waveform and (b) Fourier-transformed spectrum obtained by our high-speed waveform measurement system. The inset shows our device used in this study.
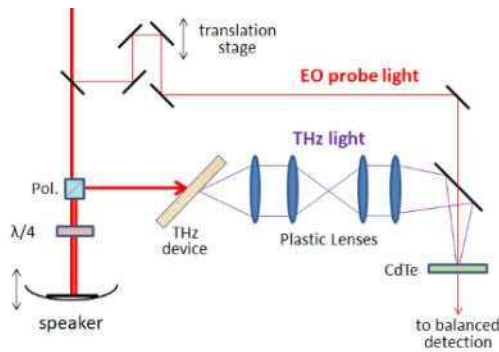
Fig. 3. Schematic of THz-TDS system with fast-scanning delay line.

References

1. K. Kawase, et al., "Non-destructive terahertz imaging of illicit drugs using spectral fingerprints," Opt. Express **11,** 2549-2554 (2003).
2. X.-C. Zhang, "Three-dimensional terahertz wave imaging," Phil. Trans. R. Soc. Lond. A **362,** 283-299 (2003).
3. S.S. Dhillon, et al., "The 2017 terahertz science and technology roadmap," J. Phys. D: Appl. Phys. **50,** 043001 (2017).
4. J. Hebling, et al., "Velocity matching by pulse front tilting for large-area THz-pulse generation," Opt. Express **10,** 1161-1166 (2002).
5. J. A. Fülöp, et al., "Design of high-energy terahertz sources based on optical rectification," Opt. Express **18,** 12311-12327 (2010).
6. M. Tsubouchi, et al., "Contact grating device with Fabry–Perot resonator for effective THz light generation," Opt. Lett. **39**, 5439-5442 (2014).
7. F. Yoshida, K. Nagashima, M. Tsubouchi, Y. Ochi, M. Maruyama, and A. Sugiyama "High-efficiency contact grating fabricated on the basis of a Fabry–Perot type resonator for terahertz wave generation," Jpn. J. Appl. Phys. **55**, 012201 (2016).

Method for Estimating Localization of DNA Lesions based on Fluorescence Anisotropy

Ken Akamatsu and Naoya Shikazono

Radiation DNA Damage Research Group, Department of Quantum Beam Life Science

DNA damage induced by ionizing radiation can cause mutations and cancers. In particular, "clustered damage," namely a DNA region containing two or more lesions within a few helical turns, is rarely repaired. This damage is induced around high-linear energy transfer (LET) ionizing-radiation tracks, but the details of such damage are unknown. We have already developed a method for estimating the localization of apurinic/apyrimidinic (AP) sites or abasic sites (APs; see Fig. 1) on DNA using Förster resonance energy transfer (FRET) occurring between different fluorescent dyes (Alexa350 and Alexa488) (*hetero*-FRET) (Fig. 2). The FRET efficiency was calculated from Alexa350 fluorescence intensities before/after enzymatic digestion of the labeled DNA with APs [1]. We succeeded in estimating qualities of clustered APs produced in ^{4}He^{2+}-, ^{12}C^{5+}-, and ^{60}Co γ-irradiated dry DNA films to study "direct" radiation effects using the method [2,3]. However, there are some problems associated with the complex protocol and the sensitivity due to the low extinction coefficient of Alexa350. Therefore, we developed "*homo*-FRET," which occurs between two or more Alexa488 molecules (Figs. 2 and 3). We can also obtain the FRET magnitude from the "fluorescence anisotropy" of *homo*-FRET between Alexa488 molecules. The new protocol using *homo*-FRET enables us to estimate DNA damage localization without any enzyme and improves the sensitivity to detect clustered damage. Herein, we present the results of the fluorescence anisotropy for DNA exposed to radiation and radio-mimetic chemicals.

PUC19 digested by Sma I was used (linear formed) for DNA samples to be irradiated. The DNA was dissolved in a 0.2M Tris-HCl (pH 7.5) buffer that was under cell-mimetic conditions in terms of radical scavenging capacity. ^{60}Co γ-rays were used as a standard radiation source at the Kyoto University Research Reactor Institute. In addition, we used well-known high-mutagenic chemicals, namely methyl methanesulfonate (MMS) and neocarzinostatin (NCS).
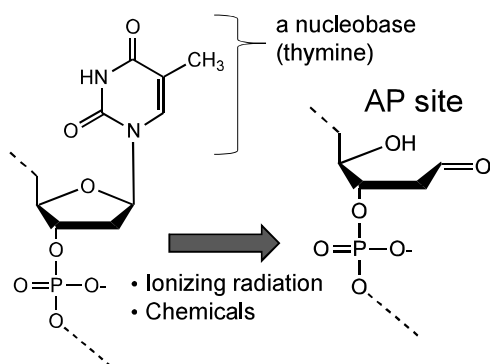
Fig. 1. Production of an abasic site (AP) on DNA. A nucleobase can be released by ionizing radiation, some chemicals, and even under physiological conditions. Several APs with an electrophilic aldehyde are known other than the "typical" one shown here.
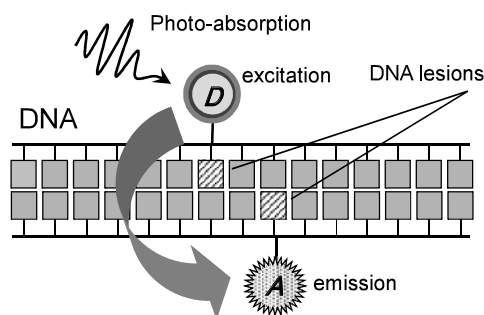
Fig. 2. Strategy of detecting clustered DNA lesions using FRET. When DNA lesions are labeled with a donor fluorescent dye (**D**) and an acceptor one (**A**), excitation energy in the photo-excited **D** can transfer to **A**. In general, FRET can occur within ~10 nm between **D-A** distance. The FRET probability is proportional to **D-A** distance to the power of −1/6.
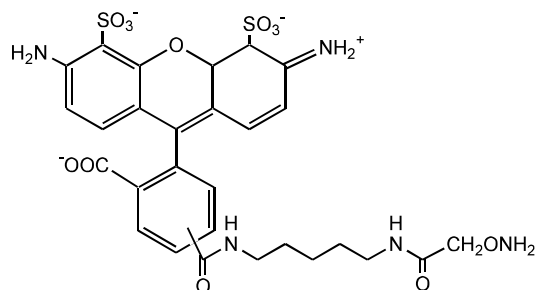
Fig. 3. Chemical structure of AlexaFluor488 C5-hydroxylamine. The hydroxylamine moiety (-ONH2) reacts selectively with an electrophilic carbonyl group such as aldehyde of AP under a mild reaction condition (e.g., neutral pH at room temperature).

We mixed the damaged DNA sample (10 µL in water) and 10 µL of 100 mM Tris-HCl (pH 7.5) in a microtube, added 2 µL of Alexa488/DMSO to the DNA solution, and incubated it for 24 h at 35°C. We purified the fluorophore-labeled DNA by ethanol precipitation followed by ultrafiltration, and then dissolved it in a buffered solution containing 80 wt% glycerin to prevent rotational Brownian motion of the fluorescent dye decreasing the anisotropy.

We measured the fluorescence anisotropy at 525 nm (ex. 470 nm) using a spectrofluorometer equipped with a xenon arc-lamp (SPEX FluoroMAX-3, HORIBA-Jobin Yvon) at 10°C. The anisotropy $< r >$ is defined as

$$<r> = (I_{VV} - G \cdot I_{VH})/(I_{VV} + 2 \cdot G \cdot I_{VH}),$$

where I_{VV} is the fluorescence intensity when the excitation and emission polarizers are both oriented vertically, I_{VH} is that when
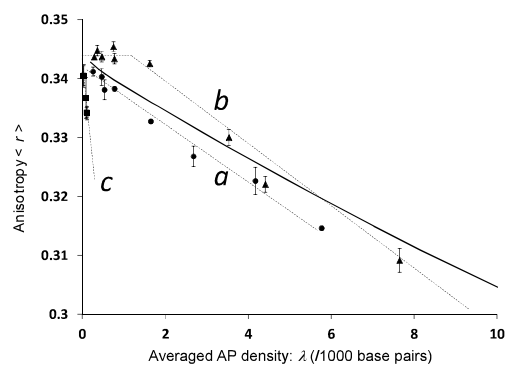
Fig. 4. Fluorescence anisotropy of AF488-labeled DNA exposed to ^{60}Co γ-rays (● line *a*), MMS (▲, line *b*), and NCS (■ line *c*) as a function of averaged AP density. The bold line represents a random distribution [5].

diene-diyne moiety

Fig. 5. Active center of NSC chromophore. Although the diene-diyne moiety is structurally unstable, its apoprotein protects the chromophore from its chemical change. However, a sulfhydryl compound such as glutathione induces diradical production on the active center.

the excitation/emission polarizers are oriented vertically/horizontally, and *G* is the grating factor defined as I_{HV}/I_{HH}. The FRET efficiency can be calculated from $<r>$ by using a theory established by Runnels and Scarlata [4].

As shown in Fig. 3, the AP distribution for ^{60}Co γ-rays is slightly more clustered than that for a random distribution. This suggests that γ-rays occasionally produce clustered APs compared to the case of a random distribution. ^{60}Co γ-rays are categorized into low-LET radiation (~0.2 keV/μm). However, a low-energy secondary electron (LEE) around the track-end ejected by the photon has a few tens of electron volts per nanometer. Clustered APs can be produced by a single track of the LEE within a few helical turns of the DNA molecule.

MMS is a well-known alkylating agent. This methylates mainly on N3 and N7 of purine nucleobases. The methylated purines are easily released from DNA to produce APs. As can be seen, there seems to be two phases. At low AP density ($λ$), $<r>$ seems to be constant. However, for $λ$ higher than ~1, $<r>$ decreases faster than the random distribution. The phenomena seen in MMS are due to differences in the alkylation rate of purines and in the release rate of the purine lesions.

NCS is an antibiotic holoenzyme that causes closely opposed carboxyl lesions under aerobic conditions because of its activated chromophore, diene-diyne diradical (Fig. 5). The $<r>–λ$ relation seems to deviate appreciably from the random distribution and from the other DNA-damaging agents tested here. The diradical leads to occasional production of closely bistranded lesions (clustered lesions) followed by DNA double-strand break (DSB). If the two closely opposed lesions labeled with the dye were produced by a single event, the anisotropy value at a low dose should be considerably less than r_0 (~0.343, $<r>$ without any FRET). However, the actual extrapolated value of $<r>$ at $λ = 0$
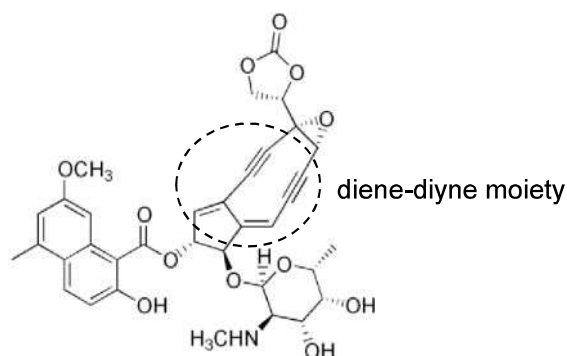
seems to be around r_0. This suggests that a single attack of NCS to DNA produces mainly single AP, but the resultant AP may attract another lesion within a few helical turns.

In conclusion, the present method will be useful for screening the mutagenicity and cytotoxicity of a chemical, an ionizing photon/particle with a given energy in terms of a new index, "AP clustering." Because there are actually numerous types of DNA lesion as well as AP, particularly those induced by ionizing radiation, the method can discover only a part of damage clustering. However, reactive carbonyl lesions are generally produced not only directly but also indirectly by nature, e.g., by a base/nucleotide repair enzyme and by an amine. Therefore, using these additives to create carbonyls will widen the application range of the method.

We have tried to apply the method to a DNA sample irradiated with a heavy-ion beam to discover the complexity of clustered DNA lesions.

References

1. K. Akamatsu, N. Shikazono, *Anal. Biochem.* **433** (2013) 171-180.
2. K. Akamatsu, et al., *Radiat. Res.* **183** (2015) 105-113.
3. K. Akamatsu, *Houshasen to Sangyo.* **145** (2017) 21-25.
4. L.W. Runnels, S.F. Scarlata, *Biophys. J.* **69** (1995) 1569.
5. K. Akamatsu, et al., *Anal. Biochem.* **536** (2017) 78-89.

Increased intensity of soft X-rays in water window from laser-produced plasma under gaseous N₂ atmosphere

Maki Kishimoto

Radiation-Induced DNA Damage Group, Department of Quantum Beam Life Science

The animals and plants that thrive on Earth consist of many cells that are the bases of all life processes. To reveal the functions of cells in life processes, we must clarify the relation between cellular structure and function, for which high-resolution observations of the fine structures of intact hydrated cells are especially important. Given that X-ray wavelengths are shorter than visible light wavelength, X-ray microscopes have been studied as a new means of observing intact biological cells in water with high resolution. In particular, soft X-ray microscopes (SXRMs) that use "water window" (WW) X-rays (i.e., those with wavelengths between the oxygen K absorption edge (2.3 nm) and the carbon K absorption edge (4.4 nm)) are expected as a new form of microscopy to enable us to observe biological cells in water with high resolution and contrast. Much study has already been conducted globally on WW SXRMs.

At QST, we have been developing a contact-type SXRM that uses an SXR source based on laser-produced plasma (LPP). However, some remaining problems must be solved before the contact-type SXRM can be used as an observation tool in biological sciences. The major problem is that achieving high-contrast X-ray imaging requires a high X-ray dose. In other words, many X-ray photons are required per unit cell area to suppress the statistical X-ray noise that degrades the resolution. Sayre et al. [1] showed that an X-ray dose of roughly 10^6 photons/μm^2 is required to obtain an X-ray image of a 1-μm-thick cell at a resolution of 50 nm. However, X-ray illumination that intense damages the cell by both breaking chemical bonds through ionization due to radiation and expanding the cell volume through heating due to X-ray absorption. Therefore, we seek to expose biological cells to short X-ray pulses of durations less than a few nanoseconds to obtain clear X-ray images without blurring.

Pulsed X-ray sources that uses a plasma produced by irradiating a target material with a high-intensity laser are called LPP light sources and are used as SXR light sources in laboratories. The SXR pulses emitted from the LPP are characterized by short durations (nearly equal to that of the excitation laser) and by emission wavelengths that depend on both the target material and specifications of the excitation laser. An LPP SXR source using a heavy-metal target (e.g., Au, W, or Bi) emits SXRs efficiently in the WW. Because a Au target is particularly suitable for WW SXRMs, we use Au as the LPP target material. However, a large laser system that can produce laser pulses in excess of tens of joules is required to generate enough WW SXR photons to achieve spatial resolutions of less than 100 nm. This is the main reason why the contact-type SXRM is not yet available as an observation tool in the biological sciences, and a new intense pulsed SXR source is required.

In SXRM experiments using Gekko XII at the Institute of Laser Engineering at Osaka University, we found that the number of WW SXR pulses from a Au LPP increased in a gaseous N₂ atmosphere [2]. The Gekko XII high-energy laser system has a wavelength, power, and duration of 1,053 nm, 120 J/pulse, and 500 ps, respectively. The target material was a thin Au film with 99.9% purity and 200 μm thickness. We used a flat-field spectrometer to measure the plasma emission spectra and a grazing-incident spherical mirror to collect the SXR pulses and focus them on the entrance slit of the spectrometer. The X-ray pulses passing through the slit were monochromatized by a grating (4,800 groves/mm) and recorded on an imaging plate (BAS-TR2025; Fujifilm Co., Japan), which was read using a laser scanner (Typhoon FLA 7000; GE Healthcare) with a 25×25 μm^2 pixel size. The spectral image was normalized over the entire area and read at 216 graduations as the emission intensity. The background of the emission intensity was obtained from an area of the spectral image without SXR exposure and subtracted from the emission intensity. The position of the emission distribution curve was translated to a wavelength on the basis of the grating equation, whereupon the wavelength was calibrated by the C and N edges. The resolving power λ degrees of the wavelength was estimated from the widths of the absorption edges and the value was less than 100. The 1,632-mm-long light path from the emission point to the imaging plate was filled with N₂ gas.

Figure 1 shows emission spectra from the Au plasma for N₂ gas pressures of 0–400 Pa. Because of X-ray absorption due to the N₂ gas, the emission intensity clearly decreases with pressure for wavelengths larger than the WW. Meanwhile, the emission intensities in the WW exceed those at zero pressure; the spectral intensity increases with pressure from zero up to 270 Pa and then decreases slightly at 400 Pa. The dip near 3.1 nm corresponds to the absorption peak of N₂.

In this experiment, the emitted SXRs were absorbed by the N₂ gas that filled the light path from the plasma to the detector. Therefore, we calculated the transmittance of the light path as a function of the gas pressure and then used the transmittance to calibrate the emission spectra. The results are shown in Fig. 2. The calibrated emission intensities clearly increase uniformly over a wide wavelength range.

The experimental results presented herein indicate that introducing N₂ gas improved the conversion efficiency of the LPP SXR source. If N₂ gas could be confined inside a small space around Au LPP (e.g., by using a gas cell or a pulsed gas jet), the absorption of the emitted SXRs would be decreased and a higher SXR intensity would be obtained at the sample point. The reported improvement in conversion efficiency makes possible single-shot SXR imaging of nanometer-scale samples in aqueous solutions using a compact pulsed laser system.

References

1. D. Sayre, et al., Ultramicroscopy **2**, pp. 337–349 (1977).
2. M. Kado, et al., Appl. Phys. Lett. **111**, 054102 (2017).
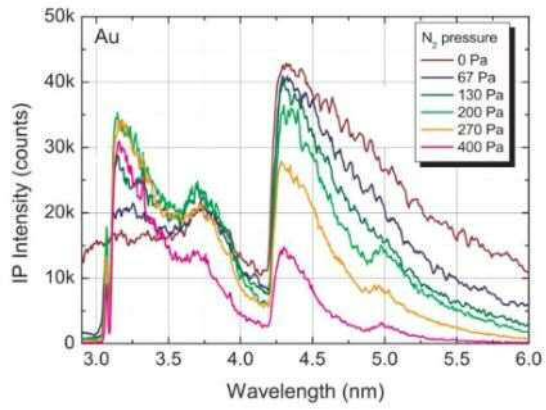
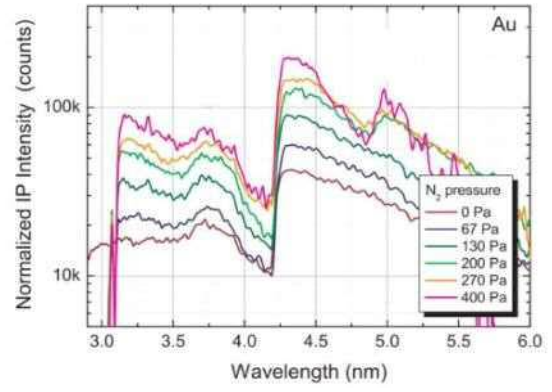Fig. 1. Emission spectra from Au plasma for various N_2 gas pressures [2].

Fig. 2. Emission spectra from Au plasma normalized by N_2 transmittance [2].

Impact of Post-translational Modifications of Histone H3 K9 on Nucleosome Structure and Dynamics

Hidetoshi Kono

Molecular Modeling and Simulation Group, Department of Quantum Life Science

Post-translational modifications (PTMs) of histone proteins, such as methylation, acetylation, and phosphorylation, play important roles in epigenetics because they have been found to be targets of many proteins that change the chromatin structure and dynamics. The nucleosome is a fundamental structural unit of chromatin. The crystal structure was solved in 1997, revealing that the nucleosome is composed of around 150 base pairs of deoxyribonucleic acid (DNA) wrapped around a histone octamer consisting of two copies each of histones H3, H4, H2A, and H2B. The histone proteins have intrinsically disordered regions whose structures cannot be determined by X-ray crystallographic analysis or nuclear magnetic resonance (NMR) spectroscopy because they do not have stable conformations. Because the disordered regions are located in either the N-terminus or C-terminus of the histone proteins, they are known as histone tails. Such tails are biologically important because (i) they are known to stabilize the nucleosome structure and (ii) amino acid residues in the tails are subject to post-translation modification as epigenetic markers. However, the nature of the tails makes it difficult to characterize their conformations experimentally.

Chromatin undergoes extensive changes during the cell cycle and is required to be relaxed or condensed for the cell to execute vital biological programs such as gene transcription and DNA repair, replication, and recombination. Chromatin restructuring is facilitated by remodeling the motors that hydrolyze ATP and using the released energy to remove, exchange, or reposition nucleosomes, the primary subunits of chromatin. Many remodeling motors operate as large multiprotein complexes consisting of regulatory and accessory components organized around a catalytic subunit. Among the major human chromatin remodeling machines is the nucleosome remodeling and deacetylase (NuRD) complex. It contains the catalytic ATPase/helicase subunit CHD. The tandem PHD fingers of the CHD subunit have been shown to bind two histone H3 tails concurrently, thereby helping to direct or stabilize the complex at specific genomic loci. The bivalent engagement of the CHD PHD fingers is required for the repressive activity of NuRD and leads to the displacement of HP1γ from pericentric sites and dispersion of the pericentric heterochromatin mark of tri-methylation of Lysine 9th in histone H3 (H3K9me3). In addition, binding of the PHD fingers to histone H3 stimulates the ATPase activity and chromatin-remodeling function of CHD4 and can in turn be augmented by the ATPase domain.

To understand the molecular mechanics of the tandem PHD fingers, we carried out a comprehensive mechanistic analysis of the bivalent engagement of a pair of readers (the tandem PHD fingers of the CHD ATPase) with the intact nucleosome. We used various methods such as NMR, chemical reactivity assays, molecular dynamics simulation, and single molecule FRET experiments [1,2]. Here, we summarize the molecular dynamics results.

Using an enhanced sampling method named ALSD that we developed recently [3,4], we studied the impact of acetylation and methylation on the 9-th residue Lys of H3 tail in a nucleosome context. This method is essential because the tails are intrinsically disordered regions and do not adopt stable conformations. Therefore, intensive conformational sampling must be performed to characterize the conformation. In doing so, we carried out 256 independent simulations with different initial conformations. The initial conformations were prepared using a 2-ns-long MD simulation under a condition where interaction energies were intentionally reduced to enhance conformational changes, starting from an extended form of histone H3 tail with different initial velocities. We performed the ALSD production run for 7.68 μs (= 30 ns × 256 runs) in total after ALSD iterative runs to realize a random walk on the λ axis. The conformational ensembles obtained by a production run of the same simulation length were analyzed after reweighting at λ = 1 based on a reweighting scheme, which corresponds to conformations under physiologically relevant conditions (300 K and 1 atm). The weight for each conformation in the ensemble indicates a relative existence probability.

The results show that irrespective of the presence or absence of the PTMs, the H3 tail remains in contact with the DNA [3]. The spatial distribution of the histone H3 tail in the conformational ensemble showed that the entire tail in NCP almost always interacts with nucleosomal DNA (Fig. 1). The H3 region encompassing residues 1–9, which are targeted by the PHD fingers, occupies both major and minor grooves of the outer DNA and forms transient hydrogen bonds with the phosphate groups of DNA. When K9 is tri-methylated or acetylated, the distributions of the tails change drastically. Essentially, irrespective of the PTMs, the tails are located along the DNA. However, upon the PTMs, the spatial distributions are limited compared to unmodified K9. Furthermore, the solvent-accessible surface area (SASA) of residues 1–9 of H3 increases for K9me3 (Fig. 2). This can be interpreted as follows. Exposing the hydrophobic methyl moieties to the solvent destabilizes the molecule. This is compensated by further exposing the hydrophilic residues in the tail. These conformational changes due to the PTM may provide a stable scaffold for the PHD fingers.

In this study, together with NMR, chemical reactivity, and FRET experiments, we show that binding of the paired PHDs to NCP is decreased compared to their binding to the free H3 peptide. NMR, chemical reactivity, molecular dynamics, and FRET analyses point to a critical role for intra-nucleosomal histone-DNA interactions, which reduce the accessibility of H3 tails in NCP and impede binding of the readers. We demonstrate that the histone-binding activities of paired PHDs toward NCP differ, with PHD2 initiating the interaction that is further modulated by the linker between the domains and by nucleosomal DNA. Our findings reveal a distinctive regulatory mechanism for the association of paired readers with the nucleosome, which provides an intricate balance between cooperative and individual activities of the readers.
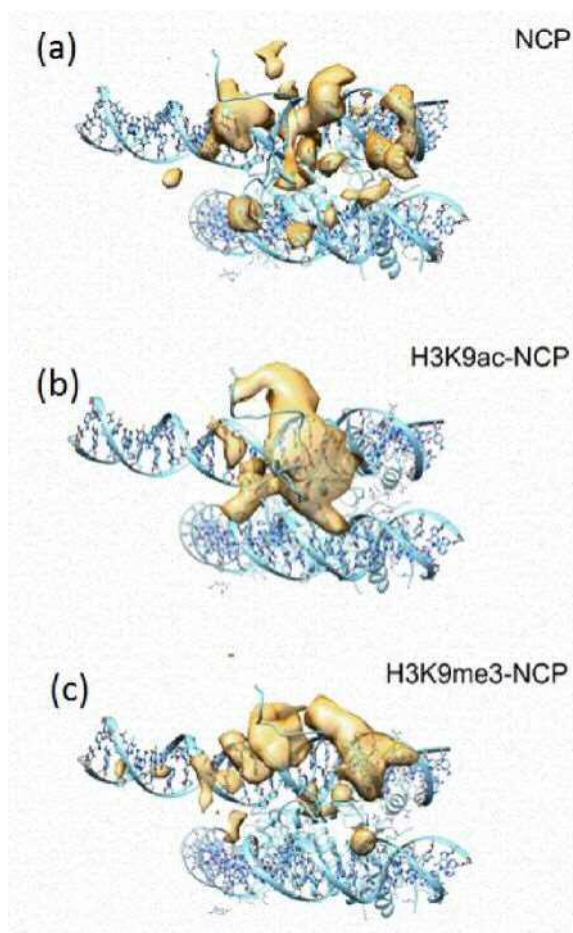
Fig. 1. Spatial distributions of K9 tip obtained by molecular dynamics simulations: (a) unmodified K9; (b) K9ac; (c) K9ac.
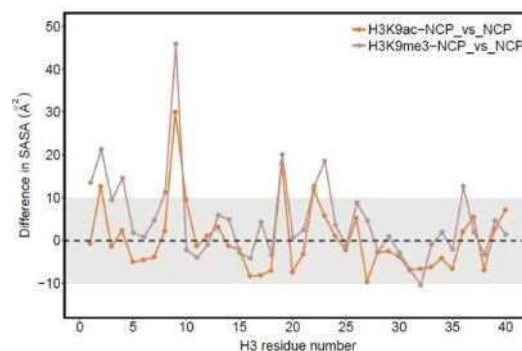
Fig. 2. Differences in solvent-accessible surface area (SASA) for each amino acid in H3 tail. Orange and brown lines denote the difference between K9ac and unmodified K9 and that between K9me3 and unmodified K9, respectively.

References

1. J. Gatchalian, X. Wang, J. Ikebe, D. Luo, M. Gibsono, Y. Zhang, K. Cox, C. A. Musselman, M. G. Poirior, H. Kono, J. J. Haynes and T. G. Kutateladze, *Nat. Comm.* (2017) **8,** 1489
2. A. H. Tencer, K. L. Cox, L. Di, J. B. Bridgers, J. Lyu, X. Wang, J. K. Sims, Tyler, H. F. Allen, Y. Zhang, J. Gatchalian, W. Li, J. Ikebe, P. A. Wade, J. J. Hayes, B. D. Strahl, H. Kono, M. G. Poirier, C. A. Musselman and T. G. Kutateladze, *Cell Reports* (2017) **21,** 455-466
3. J. Ikebe, S. Sakuraba and H. Kono, *J Comp. Chem.* (2014) **35**, 39-50
4. J. Ikebe, S. Sakuraba and H. Kono, *PLoS Comp. Biol.*,(2016) **12,** e104788

DNA conformational transitions inferred from re-evaluation of difference electron density maps

Tomoko Sunami and Hidetoshi Kono

Molecular Modeling and Simulation Group, Department of Quantum Beam Life Science

DNA plasticity is important in various biological processes such as transcriptions and packaging of genomic information. A representative example of such plasticity is the sequence-dependent deformation of DNA, which is known to be crucial for molecular recognition of DNA-binding proteins. The deformation is strongly related to the conformational transitions of the phosphate backbones of DNA.

Of the few studies that have used crystallography to analyze DNA flexibility, most used the crystallographic B-factor [1, 2]. Related to atomic thermal motion, the B-factor is expressed as the probability density function of atomic displacement from the mean position. However, it is difficult to use the B-factor to capture large conformational changes such as phosphate backbone transitions because the distribution of atomic positions in the crystal is assumed to be only spherical or elliptical in the B-factor calculation.

To deal with the variety of molecular conformations in crystals, assignments of multiple conformations have been performed. In some cases, multiple conformations of phosphate backbones were identified. However, those identifications were usually limited to high-resolution crystal structures. Recently, investigation of 2Fo−Fc electron density maps of protein structures have been reported to reveal unidentified minor conformations of protein-side chains, even in modest-resolution crystal structures [3]. In the present study, to evaluate the possibility of conformational transitions of DNA, electron density maps of DNA crystal structures were analyzed comprehensively [4].

In this study, we used the difference electron density map (m|Fo|−D|Fc|) to discover unassigned conformational transitions. Such a map represents the differences between structure factors derived from experimental X-ray diffractions and those calculated by Fourier transform of the model coordinates. Therefore, we expect such maps to provide us with information about structural transitions that were neglected in the refined models.

From the Protein Data Bank, public database of biomolecular structures, we extracted 147 sets of coordinates and X-ray structure factors of DNA solved at a resolution equal to or better than 1.5 Å. After refining the individual B-factors, we then recalculated the difference maps and extracted peaks from them. We set the threshold of the peak intensity to 3.5σ.

We began by examining the distribution of distances between peaks and their nearest DNA atoms. As shown in Fig. 1, peaks were often observed at around 1.25 Å and 3.0 Å from the DNA. Most peaks around 3.0 Å from the DNA are considered to correspond to unassigned solvent atoms, because low-occupancy solvent atoms are not be assigned in the refinement procedure in general. The peaks found around 1.25 Å are inferred to arise from the movement of the DNA itself: the distances from the DNA are too short to be interpreted due to the densities of the other molecules and too long to be interpreted due to the thermal vibration of the atoms around their mean positions. Therefore, we concluded that the peaks
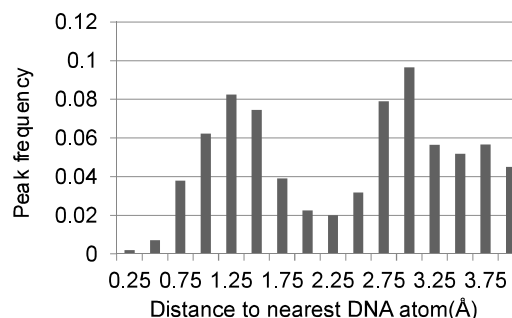
Fig. 1. Distances between peaks in the difference electron density (m|Fo|−D|Fc|) maps and their nearest DNA atoms.

correspond to conformational transitions rather than to thermal vibrations of individual atoms.

Next, we calculated the peak frequency of each atom of DNA (Fig. 2). The frequencies are around 5% for base atoms. By contrast, the peak frequencies for the atoms in sugar and phosphate are higher, namely 8-27%. In particular, P atoms most often accompany difference densities. As shown by using NMR and MD, phosphate backbones are equilibrated with different conformations in solution. Therefore, the peaks here most likely correspond to different backbone conformations in crystal.

We then classified the dinucleotides of our dataset according to known DNA conformation clusters and examined the differences in the distributions of the P-atom peaks due to the conformations. These distributions differed considerably among the conformations. The peaks were highly localized in the A/B, ZI, and ZII conformations (Fig. 3). This indicates that the movement of phosphate is strongly restricted to one direction for these three conformations. The locations of the

Fig. 2. Peak frequency of each DNA atom in the difference map. To calculate the peak frequency, peaks at distances within 2.2 Å from the DNA atoms were considered.
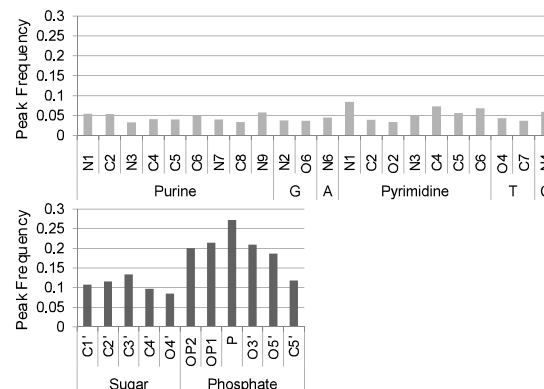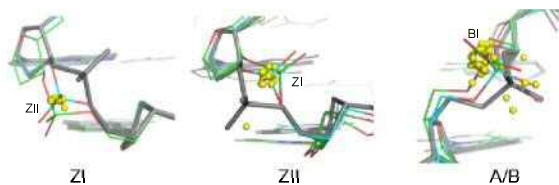
Fig. 3. Peaks in A/B, ZI, and ZII. Yellow spheres indicate peak locations. Each dinucleotide is superimposed on a representative structure of each conformer (gray). The representative structures are also superimposed on known multiple conformations (green and cyan).
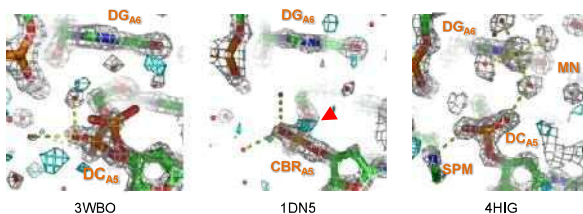
Fig. 4. Electron density maps in cation/polyamine binding sites. The 2m|Fo|−D|Fc| maps are shown in gray and the m|Fo|-D|Fc| maps are shown in cyan. A peak in the m|Fo|−D|Fc| map (1DN5) potentially corresponding to ZII is highlighted by a red arrow.

peaks found in ZI were consistent with those of P atoms of known alternative ZII conformation (Fig. 3, left). The peaks in ZII were found in locations corresponding to those of P atoms in the ZI conformation. Therefore, the peaks for ZI and ZII correspond to transited P atoms. Similarly, we interpret most of the peaks for A/B as transitions from A/B to BI.

Finally, we discuss the local environment of the DNA molecules on the ZI/ZII transitions. Many Z-DNA crystal structures for d(CGCGCG) have been solved in the same crystal system, namely $P2_12_12_1$ with a = 17.8 Å, b = 31.2 Å and c = 44.3 Å (Table 1). Guanine N7 at the sixth residue in chain A is a metal cation coordination site in the crystal structure. Upon closer observation, we found that the cations are intimately associated with the polymorphisms of phosphate of the fifth residue in the same chain. When guanine N7 at the sixth residue is coordinated directly by cations, ZI/ZII polymorphism at the fifth residue tends to be suppressed, and hence, ZII conformation is preferable, as summarized in Table 1. Electron density maps for the representative structures of the fifth phosphates are shown in Fig. 4. When guanine N7 at the sixth residue is coordinated by cations, five water molecules are coordinated octahedrally to the metal ion, as shown in 4HIG. One of the water molecules stabilizes the ZII conformation of

the fifth phosphate by interacting with atom OP1 of the phosphate. This hydrogen-bond network disappears when there is no cation at this site (e.g., 1DN5). Interactions between polyamines and the fifth phosphates are sometimes observed in addition to metal binding (Table 1). These interactions cooperatively stabilize the ZII conformations of the phosphates. Interestingly, the authors of 3WBO structure themselves assigned ZI/ZII transitions, which indicates that the transition in this structure is more obvious than in other structures. This specimen was thoroughly demineralized using liquid chromatography and no divalent cations were included in the crystallization condition. Removing divalent cations probably induces ZI/ZII transitions. Therefore, the hydrogen-bond network initiated from the divalent cations is important for determining the state of the phosphate backbone transitions.

Our analysis indicates that the electron density maps contain much structural information and that phosphate backbones assume rather polymorphic conformations even in crystals. Such information deepens our understanding of the nature of DNA conformations.

Table 1. ZI/ZII transitions in Z-DNA crystal structures

PDB ID	ZI/ZII transition		Peak intensity for ZI/ZI	Metal/polyamine binding
	Assign-ed in PDB	Found in this study		
1D39	ZII	ZII		Cu(H2O)$_5$
2ELG	ZII	ZII		Mg(H2O)$_5$
1ICK	ZII	ZII		Mg(H2O)$_5$/SPM
1VRO	ZII	ZI/ZII	3.85	Mg(H2O)$_5$/SPM
4HIF	ZII	ZII		Zn(H2O)$_5$
4HIG	ZII	ZII		Mn(H2O)$_5$/SPK
3P4J	ZII	ZII		Octahedral water structure /SPM
1D41	ZII	ZI/ZII	3.07	
1D76	ZII	ZI/ZII	3.47	
1DJ6	ZII	ZI/ZII	5.20	
1DN5	ZI	ZI/ZII	3.60	
2OBZ	ZII	ZI/ZII	4.40	
3WBO	ZI/ZII	ZI/ZII	-	

References
1. M. Wakamori, Y. Fujii, N. Suka, M. Shirouzu, K. Sakamoto, T. Umehara, S. Yokoyama *Sci. Rep.* (2015) **5**, 17204.
2. B. Schneider, J. C. Gelly, A. G. de Brevern, J. Cerny *Acta Cryst.* (2014) **D70**, 2413-2419.
3. P. T. Lang, H. L. Ng, J. S. Fraser, J. E. Corn, N. Echols, M. Sales, J. M. Holton, T. Alber *Protein Sci.* (2010) **19**, 1420-1431.
4. T. Sunami, T. Chatake and H. Kono, *Acta Cryst.* (2017) **D73**, 600-608.

Fractal nature of relaxor ferroelectrics

Kenji Ohwada

Coherent X-ray Research Group, Synchrotron Radiation Research Center

Relaxor ferroelectrics exhibit many unique and useful properties, such as large dielectric and piezoelectric coefficients with broad temperature and frequency dependencies. They have attracted intense scientific and industrial interest over the past few decades because they often show complex multiscale structures and puzzling mechanisms. Because of their good piezoelectric properties, relaxor ferroelectrics also show strong potential for industrial applications such as transducers. However, despite intensive research, the intrinsic mechanism underlying the unique properties of lead-based relaxors remains unclear. A main reason for this is the necessity to deal with the nanometer-to-micrometer-scale heterogeneity that is intrinsic to relaxors.

Typical relaxors have $PbB'B''O_3$ complex perovskite structures, where two different ions occupy the perovskite B site stoichiometrically to conserve the average charge of 4+, for example, $Pb(Mg_{1/3}^{2+}Nb_{2/3}^{5+})O_3$ (PMN) and $Pb(In_{1/2}^{3+}Nb_{1/2}^{5+})O^3$ (PIN). However, the arrangement depends strongly on the actual materials. The randomness at the B site is commonly accepted to be intrinsic to the appearance of the relaxor state.

PIN [1,2] is one of the best materials for investigating how the randomness at the B site affects the relaxor nature. Annealing PIN crystals orders the In and Nb atoms along the $\langle 111 \rangle$ direction, whereas quenching leads to disorder. PIN with a large amount of In-Nb ordered region (ordered-PIN: O-PIN) transforms into an antiferroelectric (AFE) state, while that with a large amount of In-Nb disordered region (disordered-PIN: D-PIN) becomes a relaxor. The dielectric constant $\varepsilon'(T)$ exhibits a small but sharp drop at a transition temperature T_N around 430 K in O-PIN, and by contrast, a large and broad peak around T_{max} near room temperature (RT) in D-PIN, where T_{max} depends strongly on the frequency of the electric field.

The structure and dynamics of relaxors can be understood in terms of fractals, which can deal well with a broad distribution of length and time scales [3,4]. However, few reports exist that treat the structure and dynamics in a unified approach. The present study addresses the issue using transmission electron microscope (TEM), synchrotron diffuse X-ray scattering (SDXS), and quasi-elastic light scattering (QELS) experiments on PIN to investigate the distribution of spatial structures and dynamics by changing the randomness at the B site.

Figure 1 shows the nanostructure in D-PIN observed by the TEM technique [5]. The white and black regions correspond to polar and non-polar regions, respectively. The pattern is characteristic because it remains similar if we magnify the square area in the left-hand panel by 10 times, as shown in the right-hand panel. This result indicates that the polar regions in the relaxor D-PIN have a fractal nature, as suggested previously for PMN.
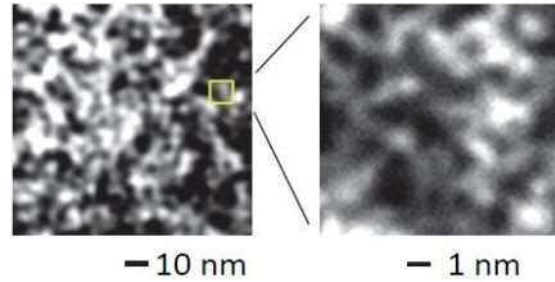
Fig. 1. TEM image of D-PIN. White regions correspond to polar regions. A similar pattern appears upon magnifying any given region, thereby showing that the sample has self-similarity (i.e., a fractal nature).

To confirm the fractal nature quantitatively, we performed SDXS measurements. Figure 2(a) shows the temperature evolution of the scattering intensity as a function of momentum transfer corresponding to the spatial size of interest [5]. Power-law behavior is clear in the log-log plot, indicating that a self-similar structure appears at low temperatures. The change in slope corresponds to the change in the fractal dimension (D_f). D_f reaches 2.5 at 100 K, indicating that the relaxor D-PIN is near the percolation threshold at that temperature. We used the QELS technique to measure the dynamics from the self-similar structure, and confirmed that these dynamics also showed power-law behavior (Fig. 2(b)) [5].

In conclusion, we have confirmed unambiguously the fractal nature of the relaxor D-PIN for the first time by the complementary use of the TEM, SDXS, and QELS techniques. No such fractal nature was observed in the antiferroelectric O-PIN, in which the randomness at the B site is excluded [5]. We expect that such fractal nature is common to inhomogeneous but functional materials that show large susceptibility, and introducing randomness is key to realizing such properties.

References

1. A. A. Bokov, I. P. Raevskii, and V. G. Smotrakov, Sov. Phys. Solid State **26**, 1708 (1984).
2. K. Ohwada and Y. Tomita, J. Phys. Soc. Jpn. **79**, 011012 (2010).
3. S. Vakhrushev, A. Nabereznov, S. K. Sinha, Y. P. Feng, and T. Egami, J. Phys. Chem. Solids **57**, 1517–1523 (1996).
4. A. Koreeda, H. Taniguchi, S. Saikan, and M. Itoh, Phys. Rev. Lett. **109**, 197601 (2012).
5. S. Tsukada, K. Ohwada, H. Ohwa, S. Mori, S. Kojima, N. Yasuda, H. Terauchi, and Y. Akishige, Sci. Rep. **7**, 17508 (2017).
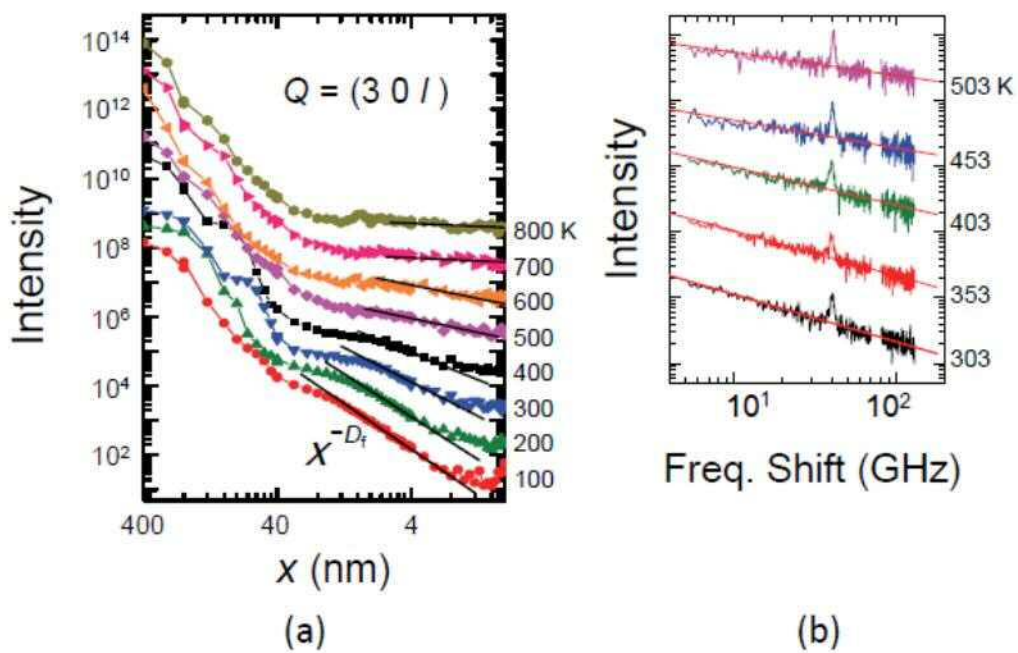
Fig. 2. Results of (a) synchrotron X-ray diffuse and (b) light scattering measurements of D-PIN. The plots are displayed on logarithmic scales. The regions indicated by the solid lines show the existence of a self-similar structure in the system, and the slopes correspond to the fractal dimension of the system.

Materials science under extreme conditions

Hiroyuki Saitoh, Akihiko Machida and Tetsu Watanuki

High Pressure Science and Stress Research Group, Synchrotron Radiation Research Center

Hydrogen forms various chemical bonds in materials.[1] Because of this bonding flexibility, hydrides exhibit various functionalities such as hydrogen storage, superconductivity, and fast ionic conductivity. Hydrogen-rich materials are expected to show excellent functionalities.

Complex transition-metal hydrides are a class of materials with high hydrogen content, in which hydrogen atoms are covalently bonded with transition-metal atoms to form complex anions. For example, iron-containing complex hydrides consist of octahedral $[FeH_6]^{4-}$ complex anions and metal cations. This six-fold hydrogen coordination realizes high hydrogen contents of iron-containing complex hydrides.[2] In the present study, we tried to synthesize a rare nine-fold hydrogen-coordinated complex hydride.[3]

The thermodynamic stability of a novel complex hydride Li_5MoH_{11} was evaluated by first-principles calculations. The theoretical calculations predicted that Li_5MoH_{11} can be synthesized via the reaction $5LiH + Mo + 3H_2 \rightarrow Li_5MoH_{11}$. Li_5MoH_{11} was predicted to consist of $[MoH_9]^{3-}$ nine-fold hydrogen-coordinated complex anion, five Li^+ ions, and two H^- ions. We tried to synthesize the theoretically predicted Li_5MoH_{11} using a high-pressure technique and to clarify the existence of the theoretically predicted nine-fold hydrogen coordination.

We developed a high-pressure technique to hydrogenate metals under high pressure and high temperature.[4] This technique enables us to hydrogenate a sample approximately 1 mg in weight, which is suitable for in situ X-ray diffraction measurements. In the present study, it is necessary to determine the hydrogen position, making neutron diffraction measurement indispensable (a deuteride is used for neutron diffraction measurement instead of the corresponding hydride). The neutron diffraction measurement requires a large sample of more than 10 mg. We developed a high-pressure technique to synthesize a large sample of several tens of milligrams for a neutron diffraction experiment. The development was carried out with the aid of in situ synchrotron-radiation X-ray diffraction measurement (Fig. 1).

A powder mixture of Mo and LiD with a molar ratio of 1:6 was prepared by mechanical milling at 400 rpm for 4 h under an Ar atmosphere. The mixture was compacted into a disk 4.0 mm in diameter and height. The disk was placed in a capsule made of pyrolytic boron nitride and sealed in a hydrogen sealing capsule made of NaCl together with an internal deuterium source (AlD_3). The sample was pressurized to 5 GPa at room temperature and deuterized at 923 K for 24 h. The deuterized sample was cooled to room temperature and then depressurized to ambient pressure.

The recovered sample was yellow in color, indicating that the deuterized sample was a complex transition-metal deuteride. The recovered sample was then subjected to neutron diffraction measurements. The obtained diffraction data were analyzed by the Rietveld method. Figure 2 shows the crystal structure of Li_5MoD_{11} determined by the Rietveld analysis. The obtained crystal structure agreed well with the theoretically predicted one; the novel complex hydride Li_5MoD_{11} was synthesized with nine-fold hydrogen coordination.

Such hydrogen-rich materials are expected to exhibit high-critical-temperature superconductivity if the gaps close under high pressure. Another preliminary calculation shows that at least one stable metallic phase of Li_5MoH_{11} is stable above 94 GPa.[3] Fast lithium conduction is also expected because of significant rotational motion of the $[MoH_9]^{3-}$ complex anions.

There has been active research on the superconductivity of strongly correlated electron systems since the discovery of high-T_c cuprates. The superconductivity mechanism of a strongly correlated electron system is considered to differ from that of conventional superconductors. Understanding this mechanism is expected to lead to design guidelines for new high-T_c superconductors. It is well known that the superconductivity of strongly correlated electron systems exhibits a superconducting dome in the vicinity of the magnetic order. There is considered to be a close relation between superconductivity and magnetic fluctuations. Recently discovered iron-based superconductors have attracted interest in their superconducting mechanism. As a typical iron-based superconductor, iron pnictide shows a superconducting phase near the antiferromagnetic phase, which is accompanied by a tetragonal-to-orthorhombic structural transition with significant electronic anisotropy (nematicity). This indicates that the fluctuations in electronic nematicity are closely related to the superconductivity in addition to the magnetic fluctuations. However, because both fluctuations appear under very similar conditions, they are difficult to distinguish.

Fig. 1. Photograph of in situ synchrotron-radiation X-ray diffraction measurement system.
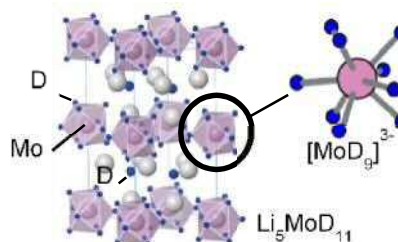
Fig. 2. Schematic of the crystal structure of Li_5MoD_{11} determined the by Rietveld refinement.

To address this issue, we focus on changes in the physical properties of the iron-based superconductor due to chemical and physical pressure effects. FeSe shows electronic nematicity below T_s = 90 K without magnetic ordering at ambient pressure. This nematicity is suppressed by substitution of Se with S (applying chemical pressure) without inducing magnetic order. By contrast, the electronic nematicity is suppressed by physical pressure. However, magnetic ordering is also induced, and T_c is enhanced up to 40 K around 6 GPa. Therefore, systematic study of temperature–pressure-substitution effect of $FeSe_{1-x}S_x$ can provide information about electronic nematicity, magnetic ordering, and superconductivity independently.[5]

As a result of high-pressure resistivity measurement, we observed separation of the partially overlapping nematic and magnetic phases by increasing the amount of S substitution. In addition, a new superconducting state was observed in this region. With further increase in S concentration, the nematicity disappeared completely and the magnetic ordering shrank. As this magnetic phase changes, the superconducting region in the P-T phase diagram becomes dome-like.

To verify the separation of nematicity and magnetic ordering, we approached from the viewpoint of the crystal structure. The synchrotron-radiation X-ray diffraction measurement was carried out using the diffractometer for diamond anvil cells[6] installed at beamline BL22XU in SPring-8. A single-crystal specimen was loaded into a diamond anvil cell with a helium pressure medium, which guaranteed hydrostatic conditions even at high pressure and low temperature. The diamond anvil cell was mounted in a closed-cycle helium refrigerator with a gas membrane for maintaining constant pressure upon cooling. The pressure in the sample space was determined by ruby fluorescence methods[7] for the whole temperature range.

From high-pressure X-ray diffraction measurements of $FeSe_{0.92}S_{0.08}$, no structural changes were observed in the region between the nematic and magnetic phases, while the magnetic phase shows lattice distortion (Fig. 3(b,c)). In this region, T_c is enhanced. This result suggests the formation of a new superconducting state in $FeSe_{1-x}S_x$. We also found differing influences of the chemical and physical pressures on the crystal structure, in particular, the chalcogen height h_{Ch} from the iron plane.

This study has revealed that the high-temperature superconductivity in FeS is closely related to the magnetic ordering and not to the electronic nematic state. The above research results provide important information for understanding the mechanism of the high-temperature superconductivity of iron-based superconductors.
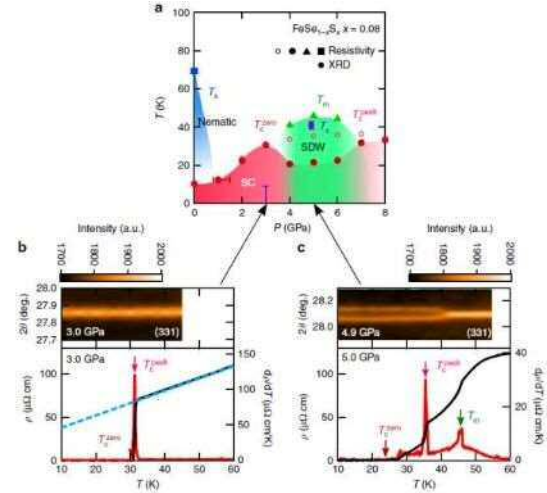
Fig. 3. (a) P-T phase diagram determined by high-pressure synchrotron-radiation X-ray diffraction and resistivity measurements. (b), (c) Temperature dependence of intensity of Bragg reflection as a function of diffraction angle 2θ for 3.0 GPa (b) and 4.9 GPa (c); $\rho(T)$ and $d\rho/dT$ are also shown with the same horizontal axis. The blue dashed line in (b) is a T linear fit to the normal-state $\rho(T)$ at 3.0 GPa (from Ref. 5).

References

1. S. Takagi and S. Orimo, Scripta Materialia, **109**, 1 (2015).
2. H. Saitoh, S. Takagi, T. Sato, Y. Iijima, and S. Orimo, Int. J. Hydrogen Energy, **42**, 22489 (2017).
3. S. Takagi, Y. Iijima, T. Sato, H. Saitoh, K. Ikeda, T. Otomo, K. Miwa, T. Ikeshoji, and S. Orimo, Sci. Rep. **7**, 44253 (2017).
4. H. Saitoh, A. Machida, and K. Aoki, Chinese Sci. Bull. **59**, 5290 (2014).
5. K. Matsuura, Y. Mizukami, Y. Arai, Y. Sugimura, N. Maejima, A. Machida, T. Watanuki, T. Fukuda, T. Yajima, Z. Hiroi, K.Y. Yip, Y.C. Chan, Q. Niu, S. Hosoi, K. Ishida, K. Mukasa, S. Kasahara, J.-G. Cheng, S.K. Goh, Y. Matsuda, Y. Uwatoko, and T. Shibauchi, Nature Communicaitons **8**, 1143 (2017).
6. T. Watanuki, A. Machida, T. Ikeda, A. Ohmura, H. Kaneko, K. Aoki, T. J. Sato, and A. P. Tsai, Philos. Mag. **87**, 2905 (2007).
7. C.-S. Zha, H.-K. Mao, and R. J. Hemley, Proc. Natl. Acad. Sci., **97**, 13494 (2000).

Observation of Magnetic Circularly Polarized Emission in the X-ray Region

Toshiya Inami

Magnetism Research Group, Synchrotron Radiation Research Center

A new magneto-optical effect is reported in the hard X-ray region. The new effect is an X-ray analog of magnetic circularly polarized emission (MCPE) in the visible region, which is a phenomenon whereby photons emitted from a magnetized material are circularly polarized. The degree of circular polarization is measured for the $K\alpha_1$ emission of metallic iron and is found to be large (~12%). It is also found that the sense of the circular polarization is reversed when the magnetization of the sample is reversed. These results constitute evidence that MCPE exists in the hard X-ray region. The observed large dichroic effect is also a feature suggesting that the new effect can be applied to a new measurement technique for practical materials.

The circular polarization of light is related to the magnetization of materials through symmetry and this fact gives rise to a magneto-optical effect. An obvious example is magnetic circular dichroism (MCD), which is the difference between absorption cross-sections when the circular polarization of incident light is parallel and antiparallel to the magnetization of a sample. Although the Faraday and magneto-optical Kerr effects are phenomena whereby the polarization plane of linearly polarized light rotates after transmission through and reflection from a magnetized sample, respectively, they are consequences of a difference between refractive indices of right and left circularly polarized light in a magnetized medium. Magneto-optical effects are very basic phenomena involving light and magnetism and now play vital roles in applications such as optical isolators and magneto-optical Kerr microscopes.

Because X-rays are a form of light, magneto-optical effects also exist in the soft and hard X-ray regions. The advent of synchrotron X-ray facilities has provided intense, highly polarized, and energy-tunable X-rays and has enabled us to observe magneto-optical effects in the X-ray region. Following the discovery at DESY of MCD in the hard X-ray region [1], major X-ray magneto-optical effects were reported in 1990s [2–4]. In particular, X-ray MCD is now a standard technique in research on magnetism because of several advantages, namely (i) element selectivity due to core-level spectroscopy, (ii) applicability of magneto-optical sum rules at spin-orbit split edges, and (iii) modestly good lateral resolution due to well-collimated synchrotron X-rays.

However, a problem with X-ray MCD is the very small dichroic effect (~0.5%) in the hard X-ray region for $3d$ transition metal (TM) elements. The use of hard X-rays is indispensable for bulk-sensitive measurements because of the long penetration length of hard X-rays into the materials. In addition, $3d$ TMs, which include Mn, Fe, Co, and Ni, are crucial elements in magnetic materials. Accordingly, there has been strong demand for finding a new principle or technique that would allow element-selective X-ray measurements with a large dichroic effect for $3d$ TM elements in the hard X-ray region.

Magnetic circularly polarized emission (MCPE) is a magneto-optical effect and a phenomenon whereby photons emitted from a magnetized material are circularly polarized. In 1971, Marrone and Kabler reported that the luminescence of excitons in alkali halides is markedly circularly polarized under magnetic fields [5]. Surprisingly, MCPE is yet to be reported in

the X-ray region. For instance, the $K\alpha$ emissions of $3d$ TMs are well-known characteristic X-rays in the hard X-ray region and correspond to transitions from the $2p$ level to the $1s$ level. The final state of $K\alpha$ emission is the $2p^5$ state and has large spin-orbit coupling, which is an essential requisite for a magneto-optical effect. A considerable interaction between the $3d$ magnetic moments and the $2p$ hole spin is also known [6]. A large dichroic effect is thus expected in $K\alpha$ emission. To address the aforementioned challenging issue, a measurement of circular polarization in $K\alpha$ emission is therefore planned here for metallic iron [7].

Experiments were carried out at beamline BL22XU at SPring-8. The experimental setup is described below and illustrated in Fig. 1. The sample was an iron single crystal that was inserted between permanent magnets to saturate the magnetization. The sample was illuminated by intense incident X-rays generated from an undulator. Fluorescence X-rays emitted from the sample were collimated by an exit slit (slit 1) down to 120 μrad in divergence. This is most important because the optical elements mentioned below are based on crystal optics. The quarter-wave plate (QWP) was a diamond single crystal that mutually converts circularly and linearly polarized X-rays. The polarization analyzer that reflects the vertical component of the incoming fluorescence X-rays was a Ge single crystal, which also functioned as an energy analyzer. The combination of a QWP and a polarization analyzer is a standard device for detecting the circular polarization of a beam of photons. Ideally, the intensity at the detector equals $I_0(1+P_C)/2$ ($I_0(1-P_C)/2$) when the QWP generates a $\pi/2$ ($-\pi/2$) phase shift, where I_0 is the total intensity and P_C is the degree of circular polarization.
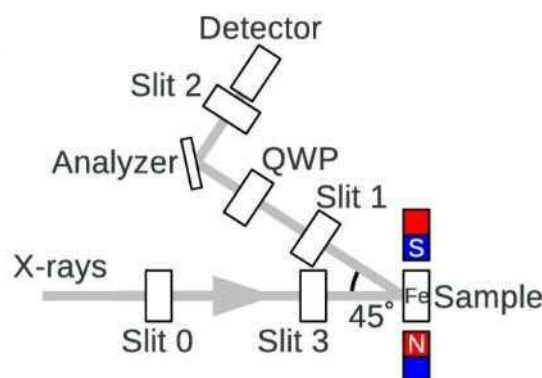
Fig. 1. Top view of experimental layout. QWP: a diamond phase retarder that acts as a quarter-wave plate. Analyzer: a Ge(400) single crystal that is both an energy and a polarization analyzer.
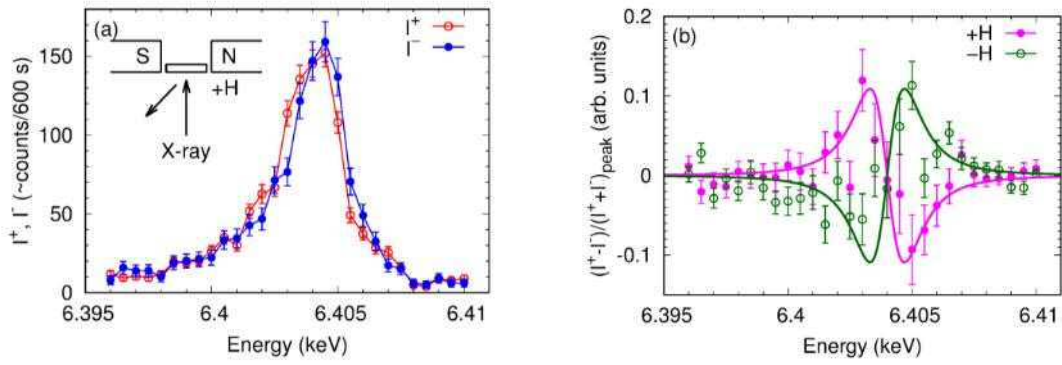
Fig. 2. (a) Fe $K\alpha_1$ emission spectra I^+ and I^- for a phase shift of $\pi/2$ (red open circles) and $-\pi/2$ (blue solid circles), respectively. The lines connect the data points to guide the eye. The magnetic field is applied as shown in the inset and the direction is defined as positive. It is obvious that the I^+ spectrum is shifted to the low-energy side compared to the I^- spectrum. (b) Difference spectra between I^+ and I^- normalized by the peak intensity. Magenta solid circles and green open circles are measured when the magnetic field is directed along the positive and negative directions, respectively. Solid lines are a guide to the eye.

The obtained Fe $K\alpha_1$ emission spectra are shown in Fig. 2(a). I^+ (red open circles) and I^- (blue closed circles) are data observed when the $\pi/2$ and $-\pi/2$ phase shifts, respectively, are introduced by the QWP. The magnetic field is applied as shown in the inset and is defined as the positive direction. It is obvious that the I^+ and I^- spectra do not coincide. The I^+ spectrum is shifted to the low-energy side by approximately 0.3 eV compared to the I^- spectrum. This difference between the two spectra is direct evidence that the $K\alpha_1$ emission is circularly polarized. The difference spectrum I^+-I^- normalized by the peak intensity of the sum spectrum is shown in Fig. 2(b) as magenta solid circles. When the magnetic field (and therefore the magnetization of the sample) is reversed, the sense of the circular polarization is reversed, as shown by the green open circles, which are data measured when the magnetic field is applied along the negative direction.

These results clearly illustrate that (i) the energy-resolved $K\alpha_1$ spectrum of ferromagnetic Fe indicates finite circular polarization and (ii) the circular polarization is inverted when the magnetization of the sample is inverted. These two features unambiguously indicate the existence of MCPE in Fe $K\alpha_1$ emission. The flipping ratio $(I^+-I^-)/(I^++I^-)$ is a measure of the size

of the dichroic effect and was $12 \pm 4\%$ at 6.405 keV. If the scattering-angle correction and QWP efficiency are considered, the value would amount to $18 \pm 6\%$. Because the flipping ratio of metallic iron in soft X-ray MCD is around 30%, a dichroic effect comparable to that in the soft X-ray region is obtained in the hard X-ray region.

To summarize, it is confirmed experimentally that MCPE exists in X-ray core-level emission and that the dichroic effect is quite large even in the K-edge of $3d$ TMs. Hence, this magneto-optical effect may open a new way to perform element-selective and truly bulk-sensitive measurements of the magnetization of $3d$ TMs.

References

1. G. Schütz *et al.*, Phys. Rev. Lett. **58**, 737 (1987).
2. D. P. Siddons, M. Hart, Y. Amemiya, and J. B. Hastings, Phys. Rev. Lett. **64**, 1967 (1990).
3. C. T. Chen, F. Sette, Y. Ma, and S. Modesti, Phys. Rev. B **42**, 7267 (1990).
4. J. B. Kortright, M. Rice, and R. Carr, Phys. Rev. B **51**, 10240 (1995).
5. M. J. Marrone and M. N. Kabler, Phys. Rev. Lett. **27**, 1283 (1971).
6. H. Mizuta and A. Kotani, J. Phys. Soc. Jpn. **54**, 4452 (1985).
7. T. Inami, Phys. Rev. Lett. **119**, 137202 (2017).

Adaptive design of an X-ray magnetic circular dichroism spectroscopy experiment with machine learning

Tetsuro Ueno

Magnetism Research Group, Synchrotron Radiation Research Center

Materials informatics, namely materials science reinforced with information science, has blossomed with the recent developments of machine-learning (ML) techniques such as convolutional neural networks. Materials informatics is aimed at the efficient discovery and development of novel materials with the assistance of ML. At the same time, metro-informatics, namely measurement techniques involving information science, is necessary for accelerating materials informatics.

Spectroscopy is one of the most important uses of quantum beams such as synchrotron X-rays. X-ray spectroscopy reveals the electronic structures of materials by exciting the core or valence electrons. X-ray magnetic circular dichroism (XMCD) spectroscopy, a variation of X-ray absorption spectroscopy (XAS), is particularly important for investigating magnetic materials such as permanent magnet materials, magnetic recording, and spintronic materials. Spins and orbital magnetic moments of a specific element can be evaluated by XMCD spectroscopy using magneto-optical sum rules. In this study, we applied an ML technique to an XMCD spectroscopy experiment to improve its efficiency.

Known as kriging, Gaussian process (GP) regression is an ML technique that is used in geostatistics to predict a geographic surface by interpolating discrete observational data [1]. An X-ray spectrum is represented as a nonlinear function of X-ray energy. GP is a generalized linear model that can approximate such nonlinear spectral shapes by linear regression in feature space. GP predicts a spectrum by tuning the hyper-parameters by learning experimental data points, namely photon energy versus intensity. Moreover, both the expectation and variance of the prediction can be evaluated. Therefore, the predictive certainty is known and an experiment can be designed adaptively (i.e., sampling new data points based on the variance).

We used an experimental XMCD spectrum to assess the applicability of GP modeling. Sm $M_{4,5}$ XMCD and XAS spectra of $SmCo_5$, a typical permanent-magnet material, were measured using a scanning transmission X-ray microscope (STXM) at the BL-13A of the Photon Factory, Institute of Materials Structure Science, High Energy Accelerator Research Organization (KEK), Japan [2]. Details of the STXM experiment are described in the literature [3].

Figure 1 shows a flowchart of the adaptive design of the XMCD spectroscopy experiment, in which one can evaluate magnetic moments in a sampling-by-sampling regime. First, initial data points are sampled to obtain an experimental spectrum as the training data. Next, a spectrum is predicted by GP modeling fitted to the training data. Then, magnetic moments are evaluated from the predicted spectra. The experiment is stopped if the values of the magnetic moments satisfy the convergence criterion. Otherwise, new data points are sampled and the spectrum is predicted again. We examined three methods for the selection of new sampling data points. (1) Sample the data point with maximum variance (max. var.) of the predicted spectrum, (2) random sampling, and (3) random sampling weighted with variance (i.e., a data point with large variance has a high possibility of being sampled). Hereafter, this sampling method is
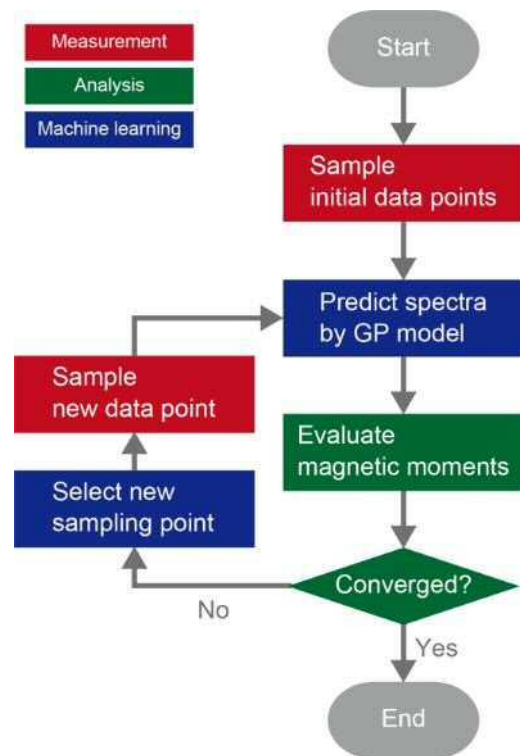
Fig. 1. Flowchart of adaptive design of XMCD spectroscopy experiment. 1) Initial data points are sampled to obtain an experimental spectrum as the training data at each energy point. 2) The Gaussian process (GP) model predicts the spectra and 3) magnetic moments are evaluated from the predicted spectra. 4) The convergence of values of the magnetic moments is checked to determine whether to sample new data points and return to predicting spectra or stop the experiment.

called "weighted sampling." Note that random sampling and weighted sampling were examined 50 times with different random numbers and averaged for all examinations.

Figure 2 shows the results of the adaptive design of the XMCD spectroscopy experiment. Typical XMCD spectra predicted by the GP model are shown in Fig. 2(a)–(d). The initial 30 data points were extracted from the experimental XMCD spectrum. Variances in the predicted spectra (red solid curves) became large among the observed data points. By increasing the number of observed data points, the total variance of the predicted spectra decreased and the spectral shape of the predicted spectrum became similar to that of the experimental (true) spectrum. Figure 2(e) shows the orbital magnetic moment m_o evaluated from the predicted spectrum plotted as a function of
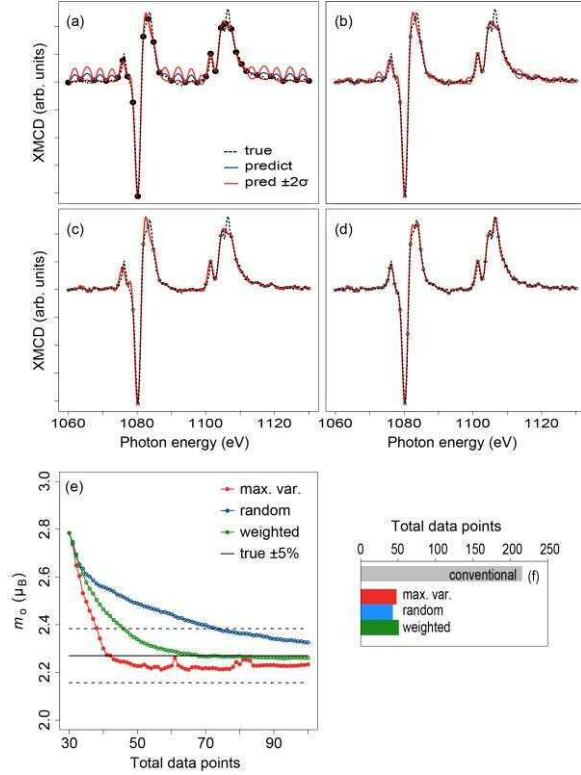
Fig. 2. (a)–(d) XMCD spectra predicted by GP model. Sm $M_{4,5}$ XMCD spectra for (a) 30, (b) 40, (c) 50, and (d) 70 total data points. The black dashed and blue solid curves represent the true (experimental) spectrum and predicted spectrum by the GP model, respectively. The open circles represent observed data points. The red solid curves indicate the variance with a 95% confidence interval ($\pm 2\sigma$) of the predicted spectrum. (e) Orbital magnetic moment m_o versus total data points. The red, blue, and green markers represent the methods for data-point sampling: maximum variance (max. var.), random, and random sampling weighted by variance, respectively. The black solid and dashed lines represent the reference value and 5% deviations, respectively. (f) Total number of data points needed for convergence of m_o values.

the total number of data points with different sampling methods. True values for the magnetic moments and the $\pm 5\%$ errors are indicated by black solid and dashed lines, respectively. The orbital magnetic moment converged to the true value at around 40 total data points with maximum variance sampling. Random sampling showed poor convergence to the true value even with 100 data points. Weighted sampling behaved halfway between maximum variance sampling and random sampling, and showed good convergence to the true value. Figure 2(f) shows the total number of data points for the various sampling methods to satisfy the convergence criterion. All sampling methods satisfied the convergence criterion at around 50 points.

In conclusion, we demonstrated the adaptive design of an XMCD spectroscopy experiment with GP modeling. GP was found to predict the nonlinear spectral shapes of the XMCD spectrum successfully. Magnetic moments could be evaluated from the predicted spectra with the required level of accuracy. The present method reduces the total number of data points for measurement as well as the time and cost of an XMCD spectroscopy experiment. This method has potential applicability to various spectroscopies. It drastically reduces the measurement time for point-by-point measurements, such as scanning transmission X-ray microscopy with scanning energy points around absorption edges.

References

1. C. E. Rasmussen and C. K. I. Williams, Gaussian Processes for Machine Learning, MIT Press (2006).
2. Y. Takeichi, N. Inami, H. Suga, C. Miyamoto, T. Ueno, K. Mase, Y. Takahashi, and K. Ono, Rev. Sci. Instrum. 87, 013704 (2016).
3. T. Ueno, A. Hashimoto, Y. Takeichi, and K. Ono, AIP Adv. 7, 056804 (2017).
4. T. Ueno, H. Hino, A. Hashimoto, Y. Takeichi, M. Sawada, and K. Ono, npj Comput. Mater. 4, 4 (2018).

First-principles centroid molecular-dynamics simulation of hydride in nanoporous C12A7:H⁻

Takashi Ikeda

Condensed Matter Theory Group, Synchrotron Radiation Research Center

Electrides are crystals with cavity-trapped electrons serving as anions. An inorganic electride $[Ca_{24}Al_{28}O_{64}]^{4+}(e^-)_4$ synthesized by Hosono *et al.* [1] in 2003 by using a main-group oxide $12CaO \cdot 7Al_2O_3$ (C12A7) is found to be stable in air up to 400°C, in sharp contrast to organic ones synthesized to date, which have been reported to be sensitive to air and moisture and decompose above roughly −40°C. As such, there has been less active investigation of organic electrides thus far, even though they are expected to exhibit various interesting physical and chemical properties arising from the presence of localized electrons. By contrast, C12A7:e⁻ is found to enhance the catalytic activity of Ru for NH_3 synthesis significantly when loaded on C12A7:e⁻ [2]. Interestingly, the poisoning of Ru surfaces by H adatoms is reported to be suppressed effectively because C12A7:e⁻ is capable of storing hydrogen reversibly in the form of H⁻ anions. Therefore, knowledge about the microscopic behavior of hydride H⁻ included in the cages of C12A7 systems would be useful for developing high-performance hydrogen-storage materials aimed at their practical use.

We investigated the behavior of hydrides in nanoporous C12A7:H⁻ by using Born–Oppenheimer (BO)-based centroid molecular dynamics (CMD), in which the quantum nature of nuclei is accounted for explicitly by using the path integral technique. As shown in Fig. 1, the system we employed includes 24 Ca^{2+}, 28 Al^{3+}, 64 O^{2-}, and 4 H⁻ ions in a cubic unit cell of side $L = 11.99$ Å, which corresponds to C12A7:H⁻ with the maximum concentration of H⁻. The distribution of H⁻ anions contained in the cages of our C12A7:H⁻, obtained at 300 and 100 K from our BO-CMD simulations, is shown in Fig. 2(a) and (c), respectively. For comparison, the corresponding distributions obtained by performing BO-MD simulations, in which the quantum nature of nuclei is ignored, are also shown in Fig. 2. In both BO-CMD and -MD results, 4 H⁻ anions are found to be widely distributed at 300 K in a similar fashion in the cages, as shown in Fig. 2(a) and (b), respectively, indicating that the thermal fluctuations dominate the quantum ones at 300 K. By contrast, the considerable difference of the H⁻ distributions between the BO-CMD and -MD results is clearly visible at 100 K, as shown in Fig. 2(c) and (d), respectively. This suggests that the behavior of hydrides in C12A7:H⁻ is governed mainly by the quantum nature of nuclei at such low temperatures.

Figure 3 shows the computed full width at half maximum (FWHM) of the distributions of H⁻ and D⁻ in our C12A7 systems. The approximate size of the cage constituting a C12A7 framework is roughly 1.2 Å smaller in radius along the S_4 symmetry axis than that perpendicular to it. Reflecting this anisotropic shape of the cage containing an anion, the computed FWHM values of the distribution of the centroids along the S_4 axis (denoted as $\rho_\parallel(H^-)$) obtained for H⁻ from our BO-CMD simulations are found to remain almost constant throughout the temperatures we considered, whereas those of the corresponding distribution perpendicular to the S_4 axis (denoted as $\rho_\perp(H^-)$) are
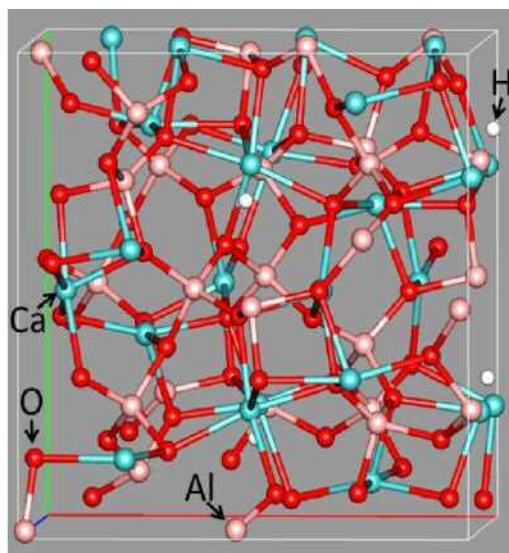
Fig. 1. Crystal structure of our C12A7:H⁻ containing 24 Ca^{2+}, 28 Al^{3+}, 64 O^{2-}, and 4 H⁻ ions in a unit cell of side $L = 11.99$ Å. Atom colors are white for H, red for O, pink for Al, and cyan for Ca.
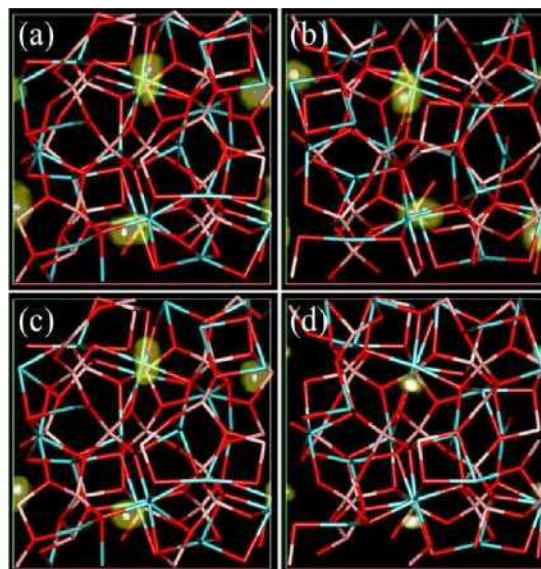
Fig. 2. Distribution of H⁻ anions in C12A7:H⁻ projected onto the xy plane at 300 K (a) ((b)) and 100 K (c) ((d)) from our CMD (MD) simulations. The regions of relatively low (high) residence probabilities of the centroids for quantum H nuclei are represented as yellow (white) isosurfaces.
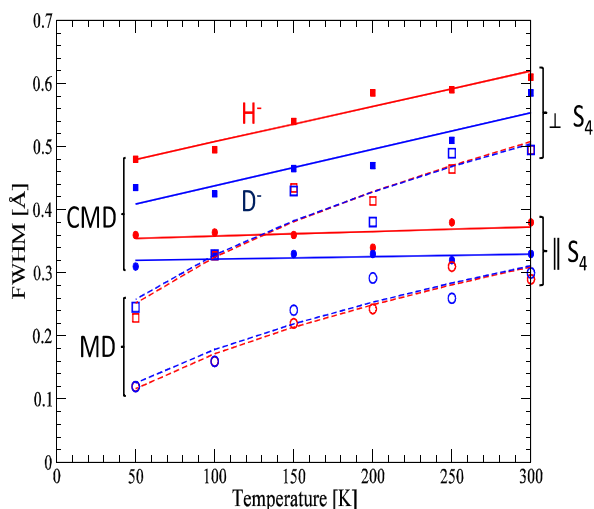
Fig. 3.   FWHM of the distributions of H⁻ and D⁻ in our C12A7 systems. Filled (open) circles and squares show the respective data for $\rho_\parallel$ and $\rho_\perp$ obtained using BO-CMD (-MD). Red and blue solid (dashed) lines show the results of the linear least-squares fitting of the computed FWHM for H⁻ and D⁻ obtained using BO-CMD (-MD), respectively.

Fig. 4. Theoretical IR ((a) and (b)) and Raman ((c) and (d)) spectra for our C12A7:H⁻ ((a) and (c)) and C12A7:D⁻ ((b) and (d)) computed from the auto-correlation function of polarization and polarizability, respectively.

shown to decrease linearly with decreasing temperature. For D⁻, the computed FWHM values show similar trends to the corresponding values for H⁻; however, we find that they are systematically smaller by 0.04 (0.07) Å for $\rho_\parallel(D^-)$ ($\rho_\perp (D^-)$) than those for $\rho_\parallel(H^-)$ ($\rho_\perp (H^-)$). By contrast, the BO-MD results do not show such systematic difference in the distributions of H⁻ and D⁻ anions, which is certainly due to the absence of zero-point vibrations in the BO-MD approach.

Figure 4 shows our computed infrared (IR) absorption ((a) and (b)) and Raman scattering ((c) and (d)) spectra for C12A7:H⁻ ((a) and (c)) and C12A7:D⁻ ((b) and (d)). For C12A7:H⁻, both IR and Raman spectra show rather small features attributed to the vibration of H⁻ at 600 and 950 cm⁻¹. Their tiny intensity found in our computed spectra for C12A7:H⁻ indicates that the dephasing of the vibration of H⁻ anions occurs in a very short time because of the strong quantum nature of the H nuclei. By contrast, for C12A7:D⁻, we find that the intensities of some peaks in the IR and Raman spectra, associated with the vibration of D⁻ located at around 300, 450, and 700 cm⁻¹, are reduced appreciably compared to those for C12A7:H⁻. This indicates that the vibration modes of

D⁻ anions, which have considerably smaller amplitude on average than those of H⁻ anions, behave as part of the phonons, in which they oscillate in phase with Ca^{2+} ions for the modes of ~300 cm⁻¹ and with Al^{3+} ions for the modes of ~450 and ~700 cm⁻¹. Therefore, our detailed analyses of the vibrational states reveal that the vibrations of H⁻ are virtually independent of each other, while those of D⁻ are highly collective, thereby resulting in the non-trivial isotope effects, which are suggested to be detectable using IR absorption and Raman scattering spectroscopy.

Acknowledgment

References

1. S. Matsuishi *et al.*, Science **301**, 626 (2003).
2. M. Kitano *et al.*, Nat. Chem. **4**, 934 (2012).
3. T. Ikeda, J. Chem. Phys. **146**, 204503 (2017).

Publication List

Publication List

Original Papers

1. Modeling of ablation of the target material for the plasma for coherent and incoherent EUV sources, A. Sasaki, A. Sunahara, K. Nishihara, W. Nishkawa, *Proceedings of the 15th International Conference on X-Ray Lasers*, **202**, 373 - 376 (2018).

2. Ultra-intense X-Ray Radiation Photopumping of Exotic States of Matter by Relativistic Laser-Plasma in the Radiation-Dominated Kinetic Regime (RDKR), A. Ya. Faenov, J.Coglan, S. A. Pikuz, A. Zhidkov, T. A. Pikuz, J. Abdallah Jr., E. Tubman, N. M. H. Butler, R. J. Dance, I. Yu. Skobelev, M. Z. Alkhimova, N. Booth, J. Green, C. Gregory, A. Andreev, M. Nishiuchi, H. Sakaki, A. Sagisaka, A. Pirozhkov, K. Ogura, Y. Fukuda, M. Kanasaki, N. Hasegawa, M. Nishikino, M. Kando, T. Kawachi, K. Kondo, P. McKenna, G. J. Tallents, N. Woolsey, R. Kodama, *Proceedings of the 15th International Conference on X-Ray Lasers*, **202**, 149 - 158 (2018).

3. Research on Laser Acceleration and Coherent X-RAY Generation Using J-KAREN-P Laser, A. Pirozhkov, M. Nishiuchi, H. Kiriyama, A. Kon, H. Sakaki, Y. Fukuda, N.P. Dover, K. Sekiguchi, K. Nishitani, A. Sagisaka, T. A. Pikuz, A. Ya. Faenov, K. Ogura, Y. Hayashi, H. Kotaki, T.Zh. Esirkepov, K. Huang, N. Nakanii, K. Kondo, J.K. Koga, K. Kondo, *Proceedings of the 15th International Conference on X-Ray Lasers*, **202**, 135 - 142 (2018).

4. High-Order Harmonic Generation by Relativistic Plasma Singularities: The Driving Laser Requirements, A. Pirozhkov, T.Zh. Esirkepov, T.A. Pikuz, A.Ya. Faenov, K. Ogura, Y. Hayashi, H. Kotaki, E.N. Ragozin, D. Neely, H. Kiriyama, J.K. Koga, Y. Fukuda, A. Sagisaka, M. Nishikino, T. Imazono, N. Hasegawa, T. Kawachi, H. Daido, Y. Kato, S.V. Bulanov, K. Kondo, M. Kando, *Proceedings of the 15th International Conference on X-Ray Lasers*, **202**, 85 - 92 (2018).

5. ERL-based Laser-Compton Scattering X-ray source for X-ray Imaging, A. Kosuge, A. Akagi, Y. Honda, S. Araki, J. Urakawa, T. Terunuma, R. Nagai, T. Shizuma, M. Mori, R. Hajima, *Proceedings of the 15th International Conference on X-ray Lasers*, **202**, 261 - 264 (2018).

6. Proposal for Experiment Systems Using Laser-Driven Heavy Ions and XFELs to Understand Physical Phenomena Occurring near the Incident Ion Path, K. Moribayashi, *Proceedings of the 15th International Conference on X-ray Lasers*, **202**, 121 - 123 (2018).

7. Analysis of reflection signal from EUV multilayer mirror for irradiation-induced damage study, M. Ishino, S. Ichimaru, M. Hatayama, N. Hasegawa, S. Oku, M. Nishikino, *Proceeding of The 15th International Conference on X-Ray Lasers*, **202**, 315 - 319 (2018).

8. In Situ Characterization of XFEL Beam Intensity Distribution and Focusability by High-Resolution LiF Crystal Detector, T. A. Pikuz, A. Ya. Faenov, T. Matsuoka, B. Albertazzi, N. Ozaki, N. Hartely, O. Muray Ricardo Arturo, T. Yabuuchi, H. Habara, S. Matsuyama, K. Yamauchi, Y. Inubushi, T. Togashi, H. Yumoto, Y. Tange, K. Tono, Y. Sato, M. Yabashi, M. Nishikino, T. Kawachi, A. Mitrofanov, S. A. Pikuz, D. Bleiner, A. Grum-Grzhimailo, N. N. Rosanov, N. V. Vysotina, M. Harmand, M. Koenig, K. A. Tanaka, T. Ishikawa, *Proceedings of the 15th International Conference on X-Ray Lasers*, **202**, 109 - 116 (2018).

9. Progress and Prospects of X-Ray Laser Research in QST, M. Nishikino, N. Hasegawa, M. Ishino, T. Imazono, A. Sasaki, K. Mikami, T. Dinh, T. Suemoto, S. Namba, A. Ya. Faenov, T. A. Pikuz, S. Ichimaru, M. Hatayama, T. Kawachi, *Proceedings of the 15th International Conference on X-Ray Lasers*, **202**, 21 - 24 (2018).

10. Irradiation damage test of Mo/Si, Ru/Si and Nb/Si multilayers using the soft x-ray laser built at QST, S. Ichimaru, M. Ishino, M. Nishikino, M. Hatayama, N. Hasegawa, T. Kawachi, T. Maruyama, K. Inokuma, M. Zenba, S. Oku, *Proceeding of The 15th International Conference on X-Ray Lasers*, **202**, 303 - 307 (2018).

11. Spectral weight of resonant inelastic X-ray scattering in doped cuprates: Effect of core-hole lifetime, T. Tohyama, K. Tsutsui, *International Journal of Modern Physics B* (2018).

12. Achieving Laser Wakefield Accelerated Electron Beams of Low Enough Energy Spread for an X-FEL, J. K. Koga, T.Zh. Esirkepov, S.V. Bulanov, M. Kando, *Proceedings of the 15th International Conference on X-Ray Lasers*, **202**, 117 - 120 (2018).

13. The Observation of Transient Thin Film Structures During the Femto-Second Laser Ablation Process by Using the Soft X-Ray Laser Probe, N. Hasegawa, M. Nishikino, M. Ishino, N. Onishi, A. M. Ito, Y. Minami, M. Baba, A. Ya. Faenov, N. Inogamov, T. Kawachi, K. Kondo, T. Suemoto, *Proceedings of the 15th International Conference on X-Ray Lasers*, **202**, 273 - 278 (2018).

14. Development of Time-Resolved Small-Angle X-Ray Scattering System Using Soft X-Ray Laser, T. Kumada, N. Hasegawa, M. Nishikino, T. Otobe, R. Motokawa, T. Suemoto, *Proceedings of the 15th International Conference on X-Ray Lasers*, **202**, 401 - 404 (2018).

15. Investigation of Surface Excitation Effect for Ablation of 4H-SiC Substrate Using Double-Pulse Beam, K. Matsunaga, T. Hayashi, S. Kurokawa, H. Yokoo, N. Hasegawa, M. Nishikino, T. Kumada, T. Otobe, Y. Matsukawa, Y. Takaya, *Proceedings of the 15th International Conference on X-Ray Lasers*, **202**, 321 - 326 (2018).

16. Laser-Induced Damage on Silica Glasses by Irradiation of Soft X-Ray Laser Pulse, K. Mikami, M. Ishino, T. Dinh, Y. Yamamoto, N. Hasegawa, M. Nishikino, T. Kawachi. S. Motokoshi, T. Jitsuno, *Proceedings of the 15th International Conference on X-Ray Lasers*, **202**, 333 - 337 (2018).

17. Development of a High Repetition Rate and High Pulse Energy Nd:YAG MOPA Laser System, K. Mikami, N. Hasegawa, H. Okada, S. Kondo, M. Nishikino, T. Kawachi, *Proceedings of the 15th International Conference on X-Ray Lasers*, **202**, 405 - 408 (2018).

18. Superfluorescence/Superradiance in Helium Following Free-Electron Laser Excitation, H. James, S.Kuma, H.Iwayama, E.Shigemasa, *Proceedings of the 15th International Conference on X-Ray Lasers*, **202**, 105 -108 (2018).

19. Predicting conformational ensembles and genome-wide Transcription Factor binding sites from DNA sequences, M. Andrabi, A. P. Hutchins, D. Miranda-Saavedra, H. Kono,R. Nussinov, K. Mizuguchi, S. Ahmad, *Scientific Reports*, **7**, 4071 (2017).

20. Nondestructive Inspection System for Special Nuclear Material Using Inertial Electrostatic Confinement Fusion Neutrons and Laser Compton Scattering Gamma-Rays, H. Ohgaki, I. Daito, H. Zen, T. Kii, K. Masuda, T. Misawa, R. Hajima, T. Hayakawa, T. Shizuma, M. Kando, and S. Fujimoto, *IEEE Transactions on Nuclear Science*, **64(7)**, 1635 - 1640 (2018),

21. Photodynamic therapy for biliary tract organ via a novel ultra-small composite optical fiberscope, K. Kasuya, K. Oka, R. Soya, T. Tsuchiya, T. Itoi, A. Tsuchida, *Experimental and Therapeutic Medicine*, **14(5)**, 4344 - 4348 (2017).

22. Laser Requirements for High-Order Harmonic Generation by Relativistic Plasma Singularities, A. Pirozhkov, T.Zh. Esirkepov, T. A. Pikuz, A. Ya. Faenov, A. Sagisaka, K. Ogura, Y. Hayashi, H. Kotaki, E. N. Ragozin, D. Neely, J. K. Koga, Y. Fukuda, M. Nishikino, T. Imazono, N. Hasegawa, T. Kawachi, H. Daido, Y. Kato, S. V. Bulanov, K. Kondo, H. Kiriyama, M. Kando, *Quantum Beam Science*, **2(1)**, 7 (2018).

23. Determination of specific ion positions of Cr^{3+} and O^{2-} in Cr_2O_3 thin films and their relationship to exchange anisotropy at Co/Cr_2O_3 interfaces, Yu Shiratsuchi, Yuuta Nakano, Nobuhito Inami, Tetsuro Ueno, Kanta Ono, Reiji Kumai, Ryoko Sagayama, Ryoichi Nakatani, *Journal of Applied Physics*, **123**, 103903-1 - 103903-7 (2018).

24. X-ray magnetic circular dichroism and hard X-ray photoelectron spectroscopy of tetragonal $Mn_{72}Ge_{28}$ epitaxial thin film, J. Kim, M. Mizuguchi, N. Inami, T. Ueno, S. Ueda, K. Takanashi, *Japanese Journal of Applied Physics*, **57(4S)**, 04FN10-1 - 04FN10-3 (2018).

25. Persistent optical hole-burning spectroscopy of nano-confined dye molecules in liquid at room temperature: spectral narrowing due to a glassy state and extraordinary relaxation in a nano-cage, H. Murakami, *The Journal of Chemical Physics*, **148(14)**, 144505-1 - 144505-12 (2018).

26. UV Harmonic Generation and Laser-Driven Proton Acceleration from Thin-Foil Target, A. Sagisaka, A. Pirozhkov, M. Nishiuchi, K. Ogura, H. Sakaki, A. Ya. Faenov, T. A. Pikuz, E. Timur, S. Bulanov, M. Kando, H. Kiriyama, K. Kondo, *The Review of Laser Engineerin*, **46(3)**, 148 - 151 (2018).

27. Improvement of Contact Grating Device for Efficient Terahertz Wave Generation Using Bi-Angular Filter, K. Nagashima, M. Tsubouchi, Y. Ochi, M. Maruyama, *Journal of Applied Physics*, **123(13)**, 123104-1 - 123104-6 (2018)

28. 高エネルギーＸ線回折を用いた銅酸化物高温超伝導体における電荷密度波の研究, 石井 賢司, 佐藤 研太朗, 浅野 駿, 藤田 全基, 中尾 裕則, *SPring-利用研究成果集*, **6(1)**, 46 - 49 (2018).

29. Spectral characterization of aperiodic normal incidence Sb/B4C multilayer mirrors for the λ < 124 Å range, E. A. Vishnyakov, I. A. Kopylets, V. V. Kondratenko, A. O. Kolesnikov, A. Pirozhkov, E. N. Ragozin, A. N. Shatokhin, *Quantum Electronics*, **48(3)**, 189 - 196 (2018).

30. Random spectral phase noise effect on the temporal contrast of ultra-high intensity laser pulse, H. Kiriyama, Y. Mashiba, Y. Miyasaka, M. Asakawa, *The Review of Laser Engineering*, **46(3)**, 142 - 144 (2018).

31. The J-KAREN-P facility laser performance status, H. Kiriyama, M. Nishiuchi, A. Pirozhkov, Y. Fukuda, H. Sakaki, A. Sagisaka, N. P. Dover, K. Kondo, K. Ogura, M. Mori, Y. Miyasaka, N. Nakanii, K. Huang, J. Koga, T.Zh. Esirkepov, M. Kando, K. Kondo, *The Review of Laser Engineering*, **46(3)**, 134 - 137 (2018).

32. Free Energy Profiles for Unwrapping the Outer Superhelical Turn of Nucleosomal DNA, H. Kono, S. Sakuraba, H. Ishida, *PLoS Comp. Biol.*, **14(3)**, e1006024-1 - e1006024-21 (2018).

33. Micron-size Hydrogen Cluster Target for Laser-Driven Proton Acceleration, S. Jinno, M. Kanasaki, M. Uno, R. Matsui, M. Uesaka, Y. Kishimoto, Y. Fukuda, *Plasma Physics and Controlled Fusion*, **60(4)**, 044021-1 - 044021-9 (2018).

34. Systematic charge distribution changes in Bi- and Pb-3d transition metal perovskites, M. Azuma, Y. Sakai, T. Nishikubo, M. Mizumaki, T. Watanuki, T. Mizokawa, K. Oka, H. Hojo, M. Naka, *Dalton Transactions*, **47**, 1371 - 1377 (2018).

35. Electro-optic spatial decoding on the spherical-wavefront Coulomb fields of plasma electron sources, K. Huang, T.Zh. Esirkepov, J. K. Koga, H. Kotaki, M. Mori, Y. Hayashi, N. Nakanii, S. V. Bulanov, M. Kando, *Scientific Reports*, **8**, 2938-1 - 2938-10 (2018).

36. Spin-1/2 Triangular-Lattice Heisenberg Antiferromagnet with √3×√3-Type Distortion --- Behavior around the Boundaries of the Intermediate Phase, A. Shimada, H. Nakano, T. Sakai, K. Yoshimura, *Journal of the Physical Society of Japan*, **87(3)**, 034706-1 - 034706-7 (2018).

37. Coherent detection of THz-induced sideband emission from excitons in the nonperturbative regime, K. Uchida, T. Otobe, T. Mochizuki, C. Kim, M. Yoshita, K. Tanaka, H. Akiyama, L. N. Pfeiffer, K. W. West, H. Hirori, *Physical Review B*, **97**, 165122-1 - 165122-7 (2018).

38. Effect of the track potential on the motion and energy flow of secondary electrons created from heavy-ion irradiation, K. Moribayashi, *Radiation Physics and Chemistry*, **146**, 68 – 72 (2018).

39. High-efficiency γ-ray flash generation via multiple-laser scattering in ponderomotive potential well, Z. Gong, R. H. Hu, Y. R. Shou, B. Qiao, C. E. Chen, X. T. He, S. S. Bulanov, T.Zh. Esirkepov, S. V. Bulanov, X. Q. Yan, *Physical Review E*, **95(1)**, 013210-1 - 013210-6 (2017).

40. Ion acceleration experiment with the high intensity, high contrast J-KAREN-P laser system, M. Nishiuchi, H. Kiriyama, H. Sakaki, N. P. Dover, K. Kondo, T. Miyahara, J. K. Koga, A. Pirozhkov, A. Sagisaka, Y. Fukuda, K. Ogura, Y. Watanabe, M. Kando, K. Kondo, *The review of laser engineering*, **46(3)**, 145 - 147 (2018).

41. Plasma equilibrium inside various cross-section capillary discharges, G. Bagdasarov, P. Sasorov, A. Boldarev, O. Olkhovskaya, V. Gasilov, A. J. Gonsalves, S. Barber, S. S. Bulanov, C. B. Schroeder, J. van Tilborg, E. Esarey, W. P. Leemans, T. Levato, D. Margarone, G. Korn, S. V. Bulanov, *Physics of Plasmas*, **24(5)**, 05311-1 - 053111-5 (2017).

42. 42. Pressure-induced coherent sliding-layer transition in the excitonic insulator Ta2NiSe5, A. Nakano, K. Sugawara, S. Tamura, N. Katayama, K. Matsubayashi, T. Okada, Y. Uwatoko, K. Munakata, A. Nakao, H. Sagayama, R. Kumai, K. Sugimoto, N. Maejima, A. Machida, T. Watanuki, H. Sawa, *IUCrJ*, **5(2)**, 158 - 165 (2018).

43. Maximizing Tc by tuning nematicity and magnetism in FeSe₁₋ₓSₓ superconductors, K. Matsuura, Y. Mizukami, Y. Arai, Y. Sugimura, N. Maejima, A. Machida, T. Watanuki, T. Fukuda, T. Yajima, Z. Hiroi, K. Y. Yip, Y. C. Chan, Q. Niu, S. Hosoi, K. Ishida, K. Mukasa, S. Kasahara, J.-G. Cheng, S. K. Goh, Y. Matsuda, Y. Uwatoko, T. Shibauchi, *Nature Communications*, **8**, 1143-1 - 1143-6 (2017).

44. Scintillator-based transverse proton beam profiler for laser-plasma ion sources, N. P. Dover, M. Nishiuchi, H. Sakaki, M.A. Alkhimova, A. Ya. Faenov, Y. Fukuda, H. Kiriyama, A. Kon, K. kondo, K. Nishitani, K. Ogura, T. A. Pikuz, A. Pirozhkov, A. Sagisaka, M. Kando, K. Kondo, *Review of Scientific Instruments*, **88(7)**, 073304-1 - 073304-7 (2017).

45. Paradoxical stabilization of forced oscillations by strong nonlinear friction, T.Zh. Esirkepov, S. V. Bulanov, *Physics Letters A*, **381(32)**, 2559 - 2564 (2017).

46. Charged particle dynamics in multiple colliding electromagnetic waves. Survey of random walk, Levy flights, limit circles, attractors and structurally determinate patterns, S. V. Bulanov, T.Zh. Esirkepov, J. K. Koga, S. S. Bulanov, Z. Gong, X. Q. Yan, M. Kando, *Journal of Plasma Physics*, **83(2)**, 905830202-1 - 905830202-45 (2017).

47. On production and asymmetric focusing of flat electron beams using rectangular capillary discharge plasmas, G. A. Bagdasarov, N. A. Bobova, A. S. Boldarev, O. G. Olkhovskaya, P. V. Sasorov, V. A. Gasilov, S. K. Barber, S. S. Bulanov, A. J. Gonsalves, C. B. Schroeder, J. van Tilborg, E. Esarey, W. P. Leemans, T. Levato, D. Margarone, G. Korn, M. Kando, S. V. Bulanov, *Physics of Plasmas*, **24(12)**, 123120-1 - 123120-10 (2017).

48. Characteristics of laser produced plasmas of hafnium and tantalum in the 1-7 nm region, B. Li, T. Otsuka, E. Sokell, P. Dunne, G. O'Sullivan, H. Hara, G. Arai, T. Tamura, Y. Ono, T. Dinh, T. Higashiguchi, *The European Physical Journal D*, **71(287)** (2017).

49. Dynamic stabilization of filamentation instability, S. Kawata, Y. J. Gu, X. F. Li, T. Karino, H. Katoh, J. Limpouch, O. Klimo, D. Margarone, Q. Yu, Q. Kong, S. Weber, S. V. Bulanov, A. Andreev, *Physics of Plasmas*, **25(1)**, 011601-1 - 011601-6 (2018).

50. Demonstration of 25-Hz-Inspection-Speed Laser Remote Sensing for Internal Concrete Defects, S. Kurahashi, K. Mikami, T. Kitamura, N. Hasegawa, H. Okada, S. Kondo, M. Nishikino, T. Kawachi, Y. Shimada, *Journal of Applied Remote Sensing*, **12(1)**, 015009-1 - 015009-10 (2018).

51. Effect of substrate orientation on strain relaxation mechanisms of InGaAs layer grown on vicinal GaAs substrates measured by in situ X-ray diffraction, H. Suzuki, T. Sasaki, M. Takahashi, Y. Ohshita, N. Kojima, I. Kamiya, A. Fukuyama, T. Ikari, M. Yamaguchi, *Japanese Journal of Applied Physics*, **56(8S2)**, 08MA06-1 - 08MA06-4 (2017).

52. Collisional-radiative model including recombination processes for W^{27+} ion, I. Murakami, A. Sasaki, D. Kato, F. Koike, *Eur. Phys. J D*, **71**, 246-1 - 246-6 (2017).

53. Coherent X-ray Diffraction for Domain Observation II, K. Ohwada, D. Shimizu, J. Mizuki, K. Fujiwara, T. Nagata, N. Ikeda, H. Ohwa, N. Yasuda, K. Namikawa, *Ferroelectrics*, **513(1)**, 16 - 21 (2018).

54. Quantum phase transition in the twisted three-leg spin tube, K. Ito, S. Ykoo, K. Okamoto, T. Sakai, *Polyhedron*, **136**, 42 - 44 (2017).

55. Magnetization Process of the Spin-1/2 Triangular-Lattice Heisenberg Antiferromagnet with Next-Nearest-Neighbor Interactions — Plateau or Nonplateau —, H. Nakano, T. Sakai, *Journal of the Physical Society of Japan*, **86(11)**, 114705-1 - 114705-5 (2017)

56. Ferrimagnetism in the Spin-1/2 Heisenberg Antiferromagnet on a Distorted Triangular Lattice, H. Nakano, T. Sakai, *Journal of the Physical Society of Japan*, **86(6)**, 063702-1 - 063702-5 (2017).

57. Exact Ground States of Frustrated Quantum Spin Systems Consisting of Spin-Dimer Units, T. Hikihara, T. Tonegawa, K. Okamoto, T. Sakai, *Journal of the Physical Society of Japan*, **86(5)**, 054709-1 - 054709-8 (2017).

58. ^{61}Ni synchrotron-radiation-based Mössbauer absorption spectroscopy of Ni nanoparticles composites, R. Masuda, H. Ishibashi, S. Hosokawa, Y. Yoda, T. Mitsui, H. Kitagawa, M. Seto, *Hyperfine Interactions*, **239**, 11-1 - 11-7 (2018)

59. Pressure-induced structural change in liquid GeI_4, K. Fuchizaki, H. Nishimura, T. Hase, H. Saito, *Journal of Physics: Condensed Matter*, **30(4)**, 045401-1 - 045401-9 (2018).

60. First principles centroid molecular dynamics simulation of high pressure ices, T. Ikeda, *The Journal of Chemical Physics*, **148(10)**, 102332-1 - 102332-8 (2018).

61. Two-magnon excitations in resonant inelastic x-ray scattering studied within spin density wave formalism, T. Nomura, *Physical Review B*, **96**, 165128-1 - 165128-10 (2017).

62. Spin state and electronic environment of iron in basaltic glass in the lower mantle, F. Maeda, S. Kamad, E. Ohtani, C. McCammon, M. Miyahara, R. Masuda, T. Mitsui, N. Hirao, *American Mineralogist*, **102(10)**, 2106 - 2112 (2017).

63. Evolution of synchrotron-radiation-based Mössbauer absorption spectroscopy for various isotopes, M. Seto, S. Kitao, Y. Kobayashi, H. Ishibashi, S. Hosokawa, M. Saito, R. Masuda, M. Kurokuzu, T. Mitsui, Y. Yoda, K. Mibu, *Hyperfine Interact*, **238**, 78-1 - 78-9 (2017).

64. ^{57}Fe nuclear resonant inelastic scattering of Fe$_{1.1}$Te, M. Kurokuzu, S. Kitao, Y. Kobayashi, M. Saito, R. Masuda, T. Mitsui, Y. Yoda, M. Seto, *Hyperfine Interactions*, **239**, 9-1 - 9-6 (2018).

65. Crystal-Site-Selective Spectrum of Fe$_3$BO$_6$by Synchrotron Mössbauer Diffraction with Pure Nuclear Bragg Scattering, S. Nakamura, T. Mitsui, K. Fujiwara, N. Ikeda, M. Kurokuzu, S. Shimomura, *Journal of the Physical Society of Japan*, **86(8)**, 084701-1 - 084701-5 (2017).

66. Burst intensification by singularity emitting radiation in multi-stream flows, A. Pirozhkov, T.Zh. Esirkepov, T. A. Pikuz, A. Ya. Faenov, K. Ogura, Y. Hayashi, H. Kotaki, E. N. Ragozin, D. Neely, H. Kiriyama, J. K. Koga, Y. Fukuda, A. Sagisaka, M. Nishikino, T. Imazono, N. Hasegawa, T. Kawachi, P. Bolton, H. Daido, Y. Kato, K. Kondo, S. V. Bulanov, M. Kando, *Scientific Reports*, **7**, 17968-1 - 17968-10 (2017).

67. Proton energy behavior by variation of the target density in laser acceleration, T. Morita, *Physics of Plasmas*, **24(8)**, 083104-1 - 083104-11 (2017).

68. Adaptive design of an X-ray magnetic circular dichroism spectroscopy experiment with Gaussian process modelling, T. Ueno, H. Hino, A. Hashimoto, Y. Takeichi, M. Sawada, K. Ono, *npj Computational Materials*, **4(1)**, 4-1 - 4-8 (2018).

69. Isotope-selective ionization utilizing field-free alignment of isotopologues using a switched nanosecond laser pulse, H. Akagi, T. Kumada, T. Otobe, R. Itakura, H. Hasegawa, Y. Ohshima, *Applied Physics B-Lasers and Optics*, **124**, 14-1 - 14-8 (2018).

70. Relation between Fractal Inhomogeneity and In/Nb-Arrangement in Pb(In$_{1/2}$Nb$_{1/2}$)O$_3$, S. Tsukada, K. Ohwada, H. Ohwa, S. Mori, S. Kojima, N. Yasuda, H. Terauchi, Y. Akishige, *Scientific Reports*, **7**, 17508-1 - 17508-8 (2017).

71. Accessibility of the histone H3 tail in the nucleosome for binding of paired readers, J. Gatchalian, K.L. Cox, X. Wang, A. H. Tencer, J. Ikebe, Y. Zhang, N. L. Burge, D. Luo, M. D. Gibson, C. A. Musselman, M. G. Poirier, H. Kono, J. J. Hayes, T. G. Kutateladz, *Nature Communications*, **8**, 1489-1 - 1489-10 (2017).

72. Covalent modifications of histone H3K9 promote binding of CHD3, A. H. Tencer, K. L. Cox, D. Luo, J. B. Bridgers, J. Lyu, X. Wang, J. K. Sims, T. M. Weaver, H. F. Allen, T. Zhang, J. Gatchalian, M. Darcy, M. Gibson, J. Ikebe, W. Li, P. A. Wade, J. J. Hayes, B. D. Strahl, H. Kono, M. G. Poirier, C. A. Musselman, T. G. Kutateladze, *Cell Reports*, **21(2)**, 455 - 465 (2017).

73. Analytical formulation for modulation of time-resolved dynamical Franz-Keldysh effect by the electron excitation in dielectrics, T. Otobe, *Physical Review B*, **96(23)**, 235115-1 - 235115-10 (2017).

74. オンライン型トムソンパラボラスペクトロメータによるレーザー加速イオンのリアルタイム計測, 神野　智史, 福田　祐仁, *放射線化学*, **104**, 41 − 45 (2017).

75. 固体飛跡検出器 CR-39 を用いたレーザー加速イオンのエネルギースペクトル及び空間分布の高精度計測, 金崎　真聡, 小田　啓二, 山内　知也, 福田　祐仁, *放射線化学*, **104**, 35 - 39 (2017).

76. 窒素イオンで照射された多結晶タングステン表面の X 線光電子分光による評価, 上浦　良友, 梅澤　憲司, 寺岡　有殿, 吉越　章隆, *日本金属学会誌*, **81(11)**, 510 - 515 (2017).

77. Devil's staircase of odd-number charge order modulations in divalent β-vanadium bronzes under pressure, T. Yamauchi, H. Ueda, K. Ohwada, H. Nakao, Y. Ueda, *Physical Review B*, **97(12)**, 125138-1 - 125138-23 (2018).

78. Pair distribution function analysis of nanostructural deformation of calcium silicate hydrate under compressive stress, S. Bae, H. Jee, M. Kanematsu, A. Shiro, A. Machida, T. Watanuki, T. Shobu, H. Suzuki, *Journal of the American Ceramic Society*, **101(1)**, 408 - 418 (2018)

79. Experimental characterization of concrete removal by high-power quasicontinuous wave fiber laser irradiation, N. Phi Long, H. Daido, T. Yamada, A. Nishimura, N. Hasegawa, T. Kawachi, *Journal of Laser Applications*, **29(4)**, 041501-1 - 041501-11 (2017).

80. Chiral Soliton Lattice Formation in Monoaxial Helimagnet $Yb(Ni_{1-x}Cu_x)_3Al_9$, T. Matsumura, Y. Kita, K. Kubo, Y. Yoshikawa, S. Michimura, T. Inami, Y. Kousaka, K. Inoue, S. Ohara, *Journal of the Physical Society of Japan*, **86(12)**, 124702-1 - 124702-12 (2017).

81. Effect of plasma formation on the double pulse laser excitation of cubic silicon carbide, T. Otobe, T. Hayashi, M. Nishikino, *Applied Physics Letters*, **111(17)**, 171107-1 - 171107-4 (2017).

82. 希土類金属3重水素化物の長周期構造の形成に関する研究, 町田晃彦, 綿貫　徹, 木村　通, 市川　貴之, 小島　由継, *SPring-8 / SACLA 利用研究成果集*, **6(1)**, 9 - 12 (2018)

83. Magnetic Circular Dichroism in X-Ray Emission from Ferromagnets, T. Inami, *Physical Review Letters*, **119(13)**, 137203-1 - 137203-5 (2017).

84. A numerical model for investigation of emission of particle debris from laser-irradiated metal targets, A. Sasaki, A. Sunahara, K. Nishihara, T. Nishikawa, *AIP Advances*, **7(9)**, 095005-1 - 095005-7 (2017).

85. Spectral evolution of soft x-ray emission from optically thin, high electron temperature platinum plasmas, H. Hara, H. Ohashi, B. Li, P. Dunne, G. O'Sullivan, A. Sasaki, C. Suzuki, N. Tamura, H. Sakaue, D. Kato, I. Murakami, T. Higashiguchi, *APL Photonics*, **2(8)**, 081301-1 - 081301-7 (2017)

86. First-Principles Molecular Dynamics Analysis of Ligand-Free Suzuki-Miyaura Cross-Coupling in Water: Transmetalation and Reductive Elimination, T. Hirakawa, Y. Uramoto, S. Yanagisawa, T. Ikeda, K. Inagaki, Y. Morikawa, *The Journal of Physical Chemistry C*, **121(36)**, 19904 - 19914 (2017).

87. New nethod for estimating clustering of DNA lesions induced by physical/chemical mutagens using fluorescence anisotropy, K. Akamatsu, N. Shikazono, T. Saitoh, *Analytical Biochemistry*, **536**, 78 - 89 (2017).

88. Synthesis of Novel Hydride Li_3AlFeH_8 at High Temperature and Pressure, H. Saitoh, S. Takagi, T. Sato, Y. Iijima, S. Orimo, *International Journal of Hydrogen Energy*, **42(35)**, 22489 – 22495 (2017).

89. Approaching the diffraction-limited, bandwidth-limited Petawatt, A. Pirozhkov, Y. Fukuda, M. Nishiuchi, H. Kiriyama, A. Sagisaka, K. Ogura, M. Mori, M. Kishimoto, H. Sakaki, N. P. Dover, K. Kondo, N. Nakanii, K. Huang, M. Kanasaki, K. Kondo, M. Kando, *Optics Express*, **25(17)**, 20486 - 20501 (2017).

90. Magnetic Compton profile evaluation of magnetization process of Tb_xCo_{100-x} films, A. Agui, C. Ma, X. Liu, N. Tsuji, M. Adachi, A. Shibayama, K. Suzzuki, H. Sakura, *Materials Research Express*, **4(10)**, 106108-1 - 106108-10 (2017).

91. Flash-lamp-pumped 4 J, 50 Hz Nd: YAG nanosecond laser system for mobile and transportable equipment, K. Mikami, N. Hasegawa, H. Okada, S. Kondo, M. Nishikino, T. Kawachi, *Japanese Journal of Applied Physics*, **56(8)**, 082701-1 - 082701-6 (2017).

92. 関西光科学研究所及びきっづ光科学館ふぉとんにおける教員研修の実践的効果評価, 星屋　泰二, *エネルギー環境教育研究*, **11(2)**, 39 - 46 (2017).

93. トンネル覆工コンクリート検査に向けたレーザー打音検査用小型高出力高繰り返しレーザー装置の開発, 岡田　大, 長谷川　登, 三上　勝大, 近藤　修司, 錦野　将元, 河内　哲哉, *レーザー研究*, **45(7)**, 427 - 432 (2017).

94. きっづふぉとん光科学ライブ 一光と色に関する効果的演示方法の検討一, 星屋　泰二, 橋本　雅史, 加道　雅孝, 織茂　聡, 山極　満, 野里　真澄, 広田　耕一, *エネルギー環境教育研究*, **11(2)**, 31 - 38 (2017).

95. Increase of the emission of laser-produced plasmas under N_2 gas atmosphere in the 2.9 – 6 nm region, M. Kado, M. Kishimoto, T. Ejima, K. Shinohara, *Applied Physics Letters*, **111(5)**, 054102-1 - 054102-4 (2017).

96. Characterization of micron-size hydrogen clusters using Mie scattering, S. Jinno, H. Tanaka, R. Matsui, M. Kanasaki, H. Sakaki, M. Kando, K. Kondo, A. Sugiyama, M. Uesaka, Y. Kishimoto, Y. Fukuda, *Optics Express*, **25(16)**, 18774 - 18783 (2017).

97. Ion pinhole imaging diagnostics on fast ion source in femtosecond laser plasma of cluster targets, S. Makarov, S. Pikuz, A. Faenov, T. Pikuz, Y. Fukuda, I. Skobelev, I. Zhbaniya, S. Varzar, M. Kando, R. Kodama, *Optics Express*, **25(14)**, 16419 - 16426 (2017).

98. Numerical modelling of the cluster targets for their optimization in femtosecond-laser-cluster-driven experiments, A.S. Boldarev, A.Y. Faenov, Y. Fukuda, S. Jinno, T.A. Pikuz, M. Kando, K. Kondo, R. Kodama, *Laser and Particle Beams*, **35(3)**, 397 - 408 (2017).

99. Two-Electron Oxygen Reduction on Carbon Materials Catalysts: Mechanisms and Active Sites, G-L. Chai, Z. Hou, T. Ikeda, K. Terakura, *The Journal of Physical Chemistry C*, **121(27)**, 14524 - 14533 (2017-07).

100. Chemical Form Analysis of Reaction Products in Cs-adsorption on Stainless Steel by means of HAXPES and SEM/EDX, M. Kobata, T. Okane, K. Nakajima, E. Suzuki, K. Ohwada, K. Kobayashi, H. Yamagami, M. Osaka, *Journal of Nuclear Materials*, **498**, 387 - 394 (2018).

101. DNA conformational transitions inferred from reevaluation of m|Fo|-D|Fc| electron density maps, T. Sunami, T. Chatake, H. Kono, *Acta Crystallographica Section D*, **73(7)**, 600 - 608 (2017).

102. Hysteresis phenomena on the crystal lattice of $Ti_{0.8}Zr_{0.2}Mn_{1.5}$ in the hydrogenation and dehydrogenation process, T. Noritake, M. Aoki, S. Towata, A. Machida, T. Watanuki, *International Journal of Hydrogen Energy*, **42(26)**, 16667 - 16674 (2017).

103. H4 tails potentially produce the diversity in the orientation of two nucleosomes, H. Ishida, H. Kono, *Biophysical Journal*, **113(5)**, 978 - 990 (2017).

104. Influence of indium supply on Au-catalyzed InGaAs nanowire growth studied by in situ X-ray diffraction, T. Sasaki, M. Takahashi, *Journal of Crystal Growth*, **468**, 135 - 138 (2017).

105. X-ray spectroscopy of super-intense laser-produced plasmas for the study of nonlinear processes. Comparison with PIC simulations, E. Dalimier, A. Ya. Faenov, E. Oks, P. Angelo, T. A. Pikuz, Y. Fukuda, A. Andreev, J. K. Koga, H. Sakaki, H. Kotaki, A. Pirozhkov, Y. Hayashi, I. Yu. Skobelev, S. A. Pikuz, T. Kawachi, M. Kando, K. Kondo, A. Zhidkov, E. Tubman, N. M. H. Butler, R. J. Dance, M. A. Alkhimova, N. Booth, J. Green, C. Gregory, P. McKenna, N. Woolsey, R. Kodama, *IOP Conf. Series: Journal of Physics: Conf. Series*, **810(1)**, 012004-1 - 012004-7 (2017).

106. Strain relaxation and compositional separation during growth of InGaAs/ GaAs(001), R. Deki, T. Sasaki, M. Takahashi, *Journal of Crystal Growth*, **468**, 241 - 244 (2017).

107. Anomalous photoelectron angular distribution in ionization of Kr in intense ultraviolet laser fields, M. Nakano, T. Otobe, R. Itakura, *Physical Review A*, **95(6)**, 063404-1 - 063404-8 (2017).

108. First principles centroid molecular dynamics simulation of hydride in nanoporous C12A7:H-, T. Ikeda, *The Journal of Chemical Physics*, **146(20)**, 204503-1 - 204503-7 (2017).

109. High power Laser Facilities in Kansai Photon Science Institute, K. Kondo, W. Utsumi, M. Kando, M. Nishikino, R. Itakura, H. Kiriyama, *Quantum Beam Science*, **1(1)**, 7-1 - 7-12 (2017).

110. Possible Precise Measurement of Delbrück Scattering Using Polarized Photon Beams, J. K. Koga, T. Hayakawa, *Physical Review Letters*, **118**, 204801-1 - 204801-5 (2017).

111. Crystal structure of the overlapping dinucleosome composed of hexasome and octasome, D. Kato, A. Osakabe, Y. Arimura, Y. Mizukami, N. Horikoshi, K. Saikusa, S. Akashi, Y. Nishimura, S-Y. Park, J. Nogami, K. Maehara, Y. Ohkawa, A. Matsumoto, H. Kono, R. Inoue, M. Sugiyama, H. Kurumizaka, *Science*, **356(6334)**, 205 - 208 (2017).

112. Quasi-Mono-Energetic Electron Beams from a Laser–Driven Argon Clustered Gas Target for Radiation Medicine, M. Tao, K. Huang, D. Li , Y. Li, X. Guo, Y. Ma, J. Zhao, M. Li, J. Wang, N. Hafz, J. Zhang, L. Chen, *Journal of medical physics and applied sciences*, **2(1)**, 3-1 - 3-5 (2017).

113. Wetting induced oxidation of Pt-based nano catalysts revealed by in situ high energy resolution X-ray absorption spectroscopy, Y. Cui, Y. Harada, H. Niwa, T. Hatanaka, N. Nakamura, M. Ando, T. Yoshida, K. Ishii, D. Matsumura, H. Oji, H. Ofuchi, M. Oshima, *Scientific Reports*, **7**, 1482-1 - 1482-8 (2017).

114. In situ X-ray diffraction of GaAs/MnSb/Ga(In)As heterostructures, P. J. Mousley, C. W. Burrows, M. J. Ashwin, M. Takahashi, T. Sasaki, G. R. Bell, physica status solidi (b), **254(2)**, 1600503-1 - 1600503-5 (2017).

115. レーザー場中にある誘電体における時間分解動的 Franz-Keldysh 効果によるサブサイクル応答, 乙部　智仁, *レーザー研究*, **45(4)**, 226 - 230 (2017).

116. Electron momentum densities near Dirac cones: Anisotropic Umklapp scattering and momentum broadening, N. Hiraoka, T. Nomura, *Scientific Reports*, **7**, 565-1 - 565-7 (2017).

117. Multilayer-coated photodiode-based beam intensity monitor for polarization analysis of plasma soft X-ray laser, T. Imazono, *Applied Optics*, **56(21)**, 5824 - 5829 (2017).

118. Observation of momentum-dependent charge excitations in hole-doped cuprates using resonant inelastic x-ray scattering at the oxygen K edge, K. Ishii, T. Tohyama, S. Asano, K. Sato, M. Fujita, S. Wakimoto, K. Tustsui, S. Sota, J. Miyawaki, H. Niwa, Y. Harada, J. Pelliciari, Y. Huang, T. Schmitt, Y. Yamamoto, J. Mizuki, *Physical Review B*, **96(11)**, 115148-1 - 115148-8 (2017).

119. A feasibility study of "range-extended" EXAFS measurement at Pt L_3-edge of Pt/Al_2O_3 in the presence of Au_2O_3, H. Asakura, N. Kawamura, M. Mizumaki, K. Nitta, K. Ishii, S. Hosokawa, K. Teramura, T. Tanaka, *Journal of Analytical Atomic Spectrometry*, **33(1)**, 84 - 89 (2018).

120. Magnetic moment evolution and spin freezing in doped $BaFe_2As_2$, J. Pelliciari, Y. Huang, K. Ishii, C. Zhang, P. Dai, G. F. Chen, L. Xing, X. Wang, C. Jin, H. Ding, P. Werner, T. Schmitt, *Scientific Reports*, **7**, 8003-1 - 8003-8 (2017).

121. 1/2 インチ配管内の検査補修用レーザー加工ヘッドの開発, 小松和三, 関健史, 長縄明大, 岡　潔, 西村昭彦, *保全学*, **16(3)**, 89 - 95 (2017).

Proceedings

1. 高輝度中赤外レーザーを用いた非侵襲血糖値センサーの開発，山川 考一，*日本光学会光設計研究グループ機関誌*，**(64)**，3 – 8（2018）．

2. Mo/Si Multilayer-Coated Photodiode Detector for Monitoring Soft X-Ray Laser Intensity, T. Imazono, *Springer Proceedings in Physics*, **202**, 309 - 313 (2018).

3. 量研における繰り返し型，超高強度 J–KAREN-P レーザーシステム，桐山 博光，西内 満美子，ピロジコフ アレキサンダー，福田 祐仁，榊 泰直，匂坂 明人，ドーバー ニコラス ピーター，近藤 康太郎，小倉 浩一，森 道昭，宮坂 泰弘，神門 正城，近藤 公伯，*電子情報通信学会技術研究報告*（2018）．

4. High Contrast High Intensity Petawatt J-KAREN-P Laser facility at QST, M. Nishiuchi, H. Kiriyama, H. Sakaki, N. P. Dover, K. Kondo, A. Pirozhkov, A. Sagisaka, Y. Fukuda, K. Nishitani, T. Miyahara, K. Ogura, M. A. Alkhimova ,T. Pikuz, Y. Faenove, Y. Watanabe, J. K. Koga, S. Bulanov, M. Kando, K. Kondo, *SPIE proceedings*, 102410N (2017).

5. Strong field electrodynamics of a thin foil, S. S. Bulanov, S. V. Bulanov, T.Zh. Esirkepov, M. Kando, S. Rykovanov, F. Pegoraro, C. B. Schroeder, E. Esarey, W. P. Leemans, *AIP Conference Proceedings*, **1812(1)** (2017).

6. Evolution of relativistic electron vortices in laser plasmas, K. V. Lezhnin, A. R. Kniazev, S. V. Soloviev, F. F. Kamenets, S. A. Weber, G. Korn, T.Zh. Esirkepov, S. V. Bulanov, *Proc. SPIE 10241, Research Using Extreme Light: Entering New Frontiers with Petawatt-Class Lasers III*, **10241** (2017).

7. Multiparametric PIC simulations of electron vortices in relativistic laser plasmas, A. R. Kniazev, S. V. Solovyev, F. F. Kamenets, K. V. Lezhnin, T.Zh. Esirkepov, S. V. Bulanov, *Proc. SPIE 10241, Research Using Extreme Light: Entering New Frontiers with Petawatt-Class Lasers III*, **10241** (2017).

8. Plasma formation in noncircular capillary discharges, G. Bagdasarov, P. Sasorov, A. Boldarev, O. Olkhovskaya, V. Gasilov, D. Khikhlukha, D. Margarone, G. Korn, S. V. Bulanov, S. S. Bulanov, C. Benedetti, A. J. Gonsalves, W. P. Leemans, *Proc. SPIE 10241, Research Using Extreme Light: Entering New Frontiers with Petawatt-Class Lasers III* **10241** (2017).

9. Soft x-ray laser ablation of metals and dielectrics, A. Faenov, T. Pikuz, M. Ishino, N. Inogamov, V. Zhakhovsky, I. Skobelev, N. Hasegawa, M. Nishikino, M. Kando, R. Kodama, T. Kawachi, *Proceedings of SPIE*, **10243**, 102430S-1 - 102430S-10 (2017).

10. Rarefaction after fast laser heating of a thin metal film on a glass mount, N.A. Inogamov, V.A. Khokhov, Y.V. Petrov, V.V. Zhakhovsky, K.P. Migdal, D.K. Ilnitsky, N. Hasegawa, M. Nishikino, M. Yamagiwa, M. Ishino, T. Kawachi, A.Y. Faenov, T.A. Pikuz, M. Baba, Y. Minami, T. Suemoto, *AIP Conference Proceedings*, **1893**, 070012 (2017).

11. Frustrated S = 1/2 Two-Leg Ladder with Different Leg Interactions, T. Tonegawa, K. Okamoto, T. Hikihara, T. Sakai, *Journal of Physics. Conference Series*, **828(1)**, 012003-1 - 01203-8 (2017).

12. Quantum Spin Liquid in the Kagome-Lattice Antiferromagnet and Related Systems, T. Sakai, H. Nakano, *Journal of Physics. Conference Series*, **868(1)**, 012006-1 - 012006-10 (2017).

13. 時間分解 X 線吸収分光による水溶液中パラジウムイオンの レーザー微粒子化反応研究，佐伯 盛久，田口 富嗣，大場 弘則，松村 大樹，辻 卓也，蓬田 匠，*電気学会研究会資料*，EFM(17)，15（2017）．

14. Simple formulas for heavy-ion-irradiation-induced electric field, K. Moribayashi, *Nuclear Instruments and Methods in Physics Research B*, **408**, 241 - 243, (2017).

15. The observation of a transient surface morphology in the femtosecond laser ablation process by using soft X-ray laser probe, N. Hasegawa, M. Nishikino, T. Tomita, N. Ohnishi, A. M. Ito, T. Eyama, N. Kamimoto, R. Idutsu, Y. Minami, M. Baba, A. Y. Faenov, N. A. Inogamov, T. Kawachi, M. Yamagiwa, T. Suemoto, *Proc. of SPIE*, **10091**, 100910O-1 - 100910O-5 (2017).

Awards

1. 文部科学省ナノテクノロジープラットフォーム平成 29 年度「秀でた利用成果」，石井　賢司（国立研究開発法人物質・材料研究機構 ナノテクノロジープラットフォームセンター、2018 年 1 月 23 日）

2. 公益社団法人日本金属学会 水素化物に関わる次世代学術・応用展開研究会 優秀ポスター賞，谷上　真惟（日本金属学会・水素化物に関わる次世代研究会、2017 年 11 月 17 日）

3. 公益社団法人日本金属学会 水素化物に関わる次世代学術・応用展開研究会 優秀ポスター賞，宇野　和仁（日本金属学会・水素化物に関わる次世代研究会、2017 年 11 月 17 日）

4. 公益社団法人日本金属学会 水素化物に関わる次世代学術・応用展開研究会 最優秀ポスター賞，森本　勝太（日本金属学会・水素化物に関わる次世代研究会、2017 年 11 月 17 日）

5. レーザ加工学会誌ベストオーサー賞受賞，宮坂　泰弘（レーザ加工学、2017 年 6 月 2 日）

6. 2016 Highly Cited Article Award，坂井　徹（Journal of the Physical Society of Japan 誌、2017 年 4 月 1 日）

The Kid's Science Museum of Photons

概要

　毎年、4 月 18 日の発明の日を含む月曜日から日曜日は「科学技術週間」となるため、定番の工作に加え、磁石やコイル、DNA 模型などの工作を行いました。また、映像ホールでは、新メニュー「THE MOON 月の不思議」の上映を開始しました。黄金週間には、外部からお招きした先生による実験工作や関西研の研究者による実験教室を開催するとともに、映像ホールでは「宇宙〜その大きさを感じてみよう〜」の上映を開始しました。7 月の中旬ごろから小学校が短縮授業になると同時に午後の来館者が増え、夏休みに入ると、子どもたちの歓声は一段と大きくなり、休館日を除く毎日、親子工作にレーザーラボ、宇宙シリーズの映像などで、連日大盛況でした。9 月からは、リニューアルしたレーザー加工機によるレーザー加工体験イベントを開始、11 月には、本部広報課による"ふぉとん"紹介ビデオの制作のため、関西研職員の子供たちの協力の下撮影が行われました。完成動画は 2 階 QST コーナーに設置されたディスプレイで上映するとともに、YouTube*にもアップされています。年末には、お出かけ情報サイト「いこーよ」**の京都南部エリア屋内施設の年間人気ランキング 1 位を獲得しました（集計期間：2016.12.1〜2017.11.30）。

　*https://www.youtube.com/watch?v=Lz-8fhSpuok&sns=fb
**https://iko-yo.net/rankings/areas/197/indoor/yearly

Ⅰ．2017 年度の活動

１．入館者状況

　平日は主に幼児連れの方や、学校、自治体による団体見学の利用が中心であり、土・日・祝日や夏休みなどには多くのご家族に利用いただいています。特に、8 月は年間を通じて月間入館者数が最も多い月でありますが、2017 年は 8,899 人と前年をやや上回る数字となりました。9 月（17 日）と 10 月（22 日）の日曜日に台風による警報が発令され、それぞれ半日と全日を休館としました。特に後者については、予定されていた関西光科学研究所の施設公開も中止となり、期待していた集客が得られませんでしたが、2017 年度の総入館者数は 44,178 人となり、昨年度（39,522 人）を上回っています。

２．主な行事

＜2017 年＞

4 月 8・9・15・16・22・23・29・30 日	親子工作 Photons de Science 2017
5 月 3〜7・14・20・21・27・28 日	親子工作 Photons Festival 2017
6 月 3・4・10・11・18・24・25 日	親子工作 Photons de あ〜した天気にな〜あれ！
7 月 1・2・8・9・15〜17・22・23・29・30 日	親子工作 Photons de もうすぐ夏休み！
8 月 2〜6・9〜16・19・20・23〜27・30・31 日	Photons de 工作夏まつり
8 月 9〜14 日	博物館（学芸員）実習生・科学館研修生（インターンシップ）として、奈良女子大学より学生 1 名受入れ

9 月 2・3・16〜18・23・24 日	Photons Happy Halloween 1st 2017
10 月 7〜9・（22）・28・29 日	Photons Happy Halloween 2nd 2017
11 月 3〜5・11・12・18・19・23・25・26 日	Photons Merry Christmas 1st 2017
12 月 2・3・9・10・16・17・23・24・27・28 日	Photons Merry Christmas 2nd 2017
12 月 2〜22 日	つくばエキスポセンター第 19 回全国ジュニア発明展（巡回展示）

＜2018 年＞

1 月 4〜8・13・14・20・21・27・28 日	ふぉとんで開運初笑い
2 月 3・4・10〜12・17・18・24・25 日	Photons Happy Valentine
3 月 3・4・10・11・17・18・21・24・25・31 日	ふぉとん さくらさくら 2018

３．事業内容（実験・工作・映像）

（１）レーザーラボ

　Nd:YAG や He-Ne レーザー、分光器等を用いた光及びレーザーに関するライブ実験を行っています。通常スケジュール、午前 11:40〜12:00、午後 15:00〜15:20、に加え、団体見学者用に適宜実施しました。また、全国科学博物館活動等助成事業（平成 29 年度採択））による招待講演（11月）では、原子力機構の西村昭彦氏によるレーザーラボスペシャルにおいて、レーザー発振や放電発光の仕組みなどについて演示を行っていただきました。

2017 年度の観覧者数は 7,768 人。

実施実績

年　　月	実施日数	実施回数	観覧者数	累積観覧者数
2017年4月	19 日	32 回	529 人	529 人
5 月	16 日	28 回	607 人	1,136 人
6 月	9 日	15 回	348 人	1484 人
7 月	19 日	36 回	1,003 人	2,487 人
8 月	21 日	50 回	1,877 人	4,364 人
9 月	17 日	28 回	547 人	4,911 人
10 月	14 日	23 回	447 人	5,358 人
11 月	17 日	29 回	446 人	5,804 人
12 月	13 日	24 回	440 人	6,244 人
2018年1月	16 日	27 回	497 人	6,741 人
2 月	15 日	24 回	456 人	7,197 人
3 月	20 日	38 回	571 人	7,768 人
年度合計	196 日	354 回	7,768 人	-

（2）レーザー加工体験

　レーザー加工機のリニューアルにともない、刻印できる絵文字をさらに豊富に整備し、9月より、スタッフ立会いのもと「レーザー加工体験」イベントとして正式運用を開始しました。開催日時は土日祝日等イベント開催日の 10:30～11:00（11 月までは 14:00～14:30 も開催）で、2017 年度の体験者総数は 140 人。

レーザー加工体験

実施実績

年　　月	実施日数	実施回数	体験者数	累積体験者数
2017年4月	-	-	-	-
5 月	-	-	-	-
6 月	-	-	-	-
7 月	-	-	-	-
8 月	-	-	-	-
9 月	5 日	9 回	28 人	28 人
10 月	7 日	12 回	34 人	62 人
11 月	8 日	11 回	27 人	89 人
12 月	5 日	5 回	10 人	99 人
2018年1月	6 日	6 回	14 人	113 人
2 月	5 日	5 回	15 人	128 人
3 月	6 日	6 回	12 人	140 人
年度合計	42 日	54 回	140 人	-

（3）実験・工作教室

　主に小学生を対象とした実験・工作教室をマルチホールとロビーにおいて開催しました。通常、マルチホールでは、（午前）10:30～11:00（午後）13:00～13:30 と 15:00～15:30、ロビーでは随時実施しています。

実験・工作教室実績

年　　月	実施日数		マルチホール実験・工作		ロビー工作
	マルチ	ロビー	実施回数	参加者数	参加者数
2017年4月	20 日	21 日	35 回	255 人	1,455 人
5 月	18 日	19 日	35 回	449 人	1,351 人
6 月	19 日	19 日	35 回	352 人	1,097 人
7 月	21 日	22 日	45 回	414 人	2,707 人
8 月	22 日	22 日	66 回	632 人	5,349 人
9 月	20 日	22 日	36 回	292 人	1,784 人
10 月	15 日	16 日	32 回	307 人	1,176 人
11 月	19 日	22 日	42 回	300 人	1,228 人
12 月	18 日	17 日	40 回	616 人	962 人
2018年1月	17 日	20 日	42 回	310 人	1,294 人

2 月	16 日	18 日	34 回	243 人	1,228 人
3 月	20 日	23 日	51 回	359 人	1,333 人
年度合計	225 日	241 日	493 回	4,529 人	20,964 人

（４）映像コンテンツの上映

　　光の映像ホール（ドーム型全天周映像ホール）において、通常スケジュール、（午前）11:10～11:30（午後）14:00～14:30 と（イベント開催日のみ）15:40～16:00、に加え、団体見学者用に適宜、以下のコンテンツから 1 日あたり 2～3 作品の上映を行いました。2017 年度の観覧者数は28,426 人。

　　１）映像コンテンツ

　　⓪ 宇宙～その大きさを感じてみよう～（25 分）

　　　　太陽系惑星の大きさ、距離、銀河系の大きさ、宇宙大規模構造等を学習します。

　　⓪ ふと気になる宇宙（25 分）

　　　　どこからが宇宙？宇宙の大きさって？等宇宙の話題について考えます。

　　⓪ THE MOON 月の不思議（25 分）

　　　　月の満ち欠け、月面の様子、地球からの距離や大きさの比較、月の生成、誕生の歴史を学習します。

　　⓪ ブラックホールの謎（25 分）

　　　　ブラックホールや太陽系外惑星などを電磁波の旅で探ります。

　　⓪ 今日の星空（15 分）

　　　　今日の木津川市の星空を紹介します。

①　　　　　②　　　　　③　　　　　④　　　　　⑤

　　２）上映実績

年　　月	上映日数	上映回数	観覧者数	累積観覧者数
2017年4月	21 日	50 回	1,722 人	1,722 人
5 月	20 日	50 回	2,296 人	4,018 人
6 月	20 日	44 回	1,531 人	5,549 人
7 月	21 日	60 回	3,777 人	9,326 人
8 月	22 日	67 回	6,028 人	15,354 人
9 月	22 日	49 回	2,435 人	17,789 人
10 月	18 日	47 回	1,883 人	19,672 人
11 月	22 日	56 回	1,638 人	21,310 人
12 月	20 日	48 回	1,457 人	22,767 人

2018年1月	20 日	46 回	1,858 人	24,625 人
2 月	20 日	44 回	1,929 人	26,554 人
3 月	23 日	58 回	1,872 人	28,426 人
年度合計	249 日	619 回	28,426 人	-

４．実験・工作実施例
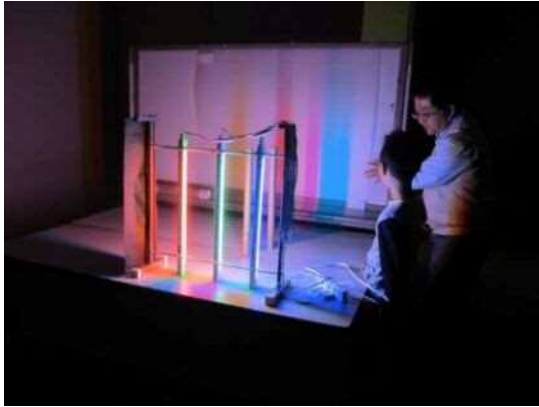
光と影の実験

光と影の部屋

紙コップカメラ

DNA 模型工作

不思議な（偏光フィルム）箱

UVレジン

ふぉとんくん（稼動中）

本部広報課からも応援

ハロウィンレジン

グラススコープ

UV スライム

キラキラ棒

QST コーナーのディスプレイと巡回展示

梅美台小学校生来館
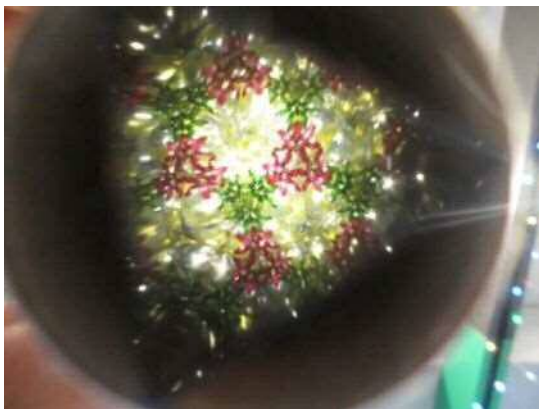
クリスマススコープ

クリスマスリース

戌年レジン

スーパーボール

チョコレートリース

♡レジン

さくらプラバン

さくらレジン

Ⅱ．2017 年度利用状況

1．入館者数（2017 年 4 月 1 日〜2018 年 3 月 31 日）

		開館日数	入館者数	
			月別	累計
2017	4 月	22 日	3,059 人	3,059 人
	5 月	21 日	3,314 人	6,373 人
	6 月	21 日	2,662 人	9,035 人
	7 月	22 日	5,656 人	14,691 人
	8 月	23 日	8,899 人	23,590 人
	9 月	22 日	3,493 人	27,083 人
	10 月	18 日	2,947 人	30,030 人
	11 月	22 日	2,565 人	32,595 人
	12 月	20 日	2,589 人	35,184 人
2018	1 月	20 日	2,734 人	37,918 人
	2 月	20 日	3,012 人	40,930 人
	3 月	24 日	3,248 人	44,178 人
年度合計		255 日	44,178 人	－

2．月別及び累積入館者数分布

Appendix

共同研究課題、施設共用課題

1）光量子科学研究施設

【共同研究課題】

共同研究先	共同研究課題名	担当研究グループ
東京学芸大学	リラクサー強誘電体のドメイン形成に関する研究	X線レーザー研究グループ
京都大学	高強度レーザーと構造性媒質との相互作用に関する研究	高強度レーザー科学研究グループ
神戸大学	固体飛跡検出器を用いた高エネルギーイオン検出手法開発	高強度レーザー科学研究グループ
兵庫県粒子線医療センター	量子メスを目指した粒子線照射計測・制御技術に関する研究	高強度レーザー科学研究グループ
大阪大学	ステージングレーザー電子加速に関する研究	高強度レーザー科学研究グループ
自然科学研究機構核融合科学研究所、東北大学	分子動力学シミュレーションを用いたフェムト秒レーザーアブレーションに関する研究	X線レーザー研究グループ
宇都宮大学、広島大学	水の窓高輝度軟X線発生に関する基礎研究	X線レーザー研究グループ
㈱島津製作所	高耐性光学デバイスの開発研究	X線レーザー研究グループ
九州大学	高効率フェムト秒レーザーアブレーションに関する基礎研究	X線レーザー研究グループ
NTTアドバンステクノロジ㈱	高耐力軟X線光学素子に関する基礎研究	X線レーザー研究グループ
慶應義塾大学	レーザーを活用した整形外科インプラント設置強度評価機構の開発	X線レーザー研究グループ
大阪大学	光学材料、光学薄膜の損傷機構のパーコレーションモデル	X線レーザー研究グループ
近畿大学	高強度・超高速レーザーを用いた化学物質の構造解析および反応制御に関する基盤技術開発	超高速光物性研究グループ
理化学研究所	テラヘルツパルス光源による高分子高次構造の制御	超高速光物性研究グループ
大阪大学	レーザーセラミックス接合に関する基礎研究	超高速光物性研究グループ
奈良先端科学技術大学院大学	有機マイクロキャビティを用いた強結合状態の観測と制御に関する基盤技術開発	超高速光物性研究グループ

大阪大学	高強度テラヘルツパルス光源による新規物質創成と新規物性発現に関する研究	超高速光物性研究グループ
東北大学、㈱島津製作所	極端紫外線領域の低入射角高効率回折格子の開発	光量子科学研究部
東京大学	生体分子シミュレーションシステムを用いた生体分子機能の解明研究	生体分子シミュレーショングループ
理化学研究所	パッキング最適化計算に基づくタンパク質結晶内分子配座の予測と改良	生体分子シミュレーショングループ
日本原子力研究開発機構	中性子散乱による生体高分子のダイナミクス解析に関する研究	生体分子シミュレーショングループ
㈱OK ファイバーテクノロジー	配管内アクセスによるレーザー溶接システムの開発	量子生命科学研究部
理化学研究所	物理、化学、計算科学を統合した動的構造生物学の確立	生体分子シミュレーショングループ
大阪大学	レーザー走査センシングの高度化に関する開発	X線レーザー研究グループ

【施設共用課題】

平成 29 年度全期施設共用課題

課題番号	利用区分	施設装置	利用課題
2017A-K01	公開	X線レーザー実験装置	ダブルパルス照射による基板表面励起加工過程の調査に関する研究
2017A-K02	公開	X線レーザー実験装置	EUV 放射用レジスト材料アブレーションの X 線放射パルス幅依存性に関する研究
2017A-K03	公開	軟 X 線平面結像型回折格子評価装置	極端紫外線（EUV）回折格子の結像評価研究

平成 29 年度後期施設共用課題

課題番号	利用区分	施設装置	利用課題
2017B-K01	公開	X 線レーザー実験装置	高耐性軟 X 線光学素子に関する基礎研究

２）放射光科学研究施設

【共同研究課題】

共同研究先	共同研究課題名	担当研究グループ
日本原子力研究開発機構	ダイヤモンドアンビル回折計を用いた高圧物性研究	高圧・応力科学研究グループ

日本原子力研究開発機構	高圧プレス装置を用いた高圧物性研究	高圧・応力科学研究グループ
京都大学	同位体特定による局所状態解明のための先進的メスバウアー分光法の開発研究	磁性科学研究グループ
日本原子力研究開発機構	大型回折計を用いた物質材料評価研究	磁性科学研究グループ
日本原子力研究開発機構	XAFS 測定装置を用いた機能性材料のオペランド観察	高圧・応力科学研究グループ
日本原子力研究開発機構	κ型回折計を用いた機能性材料の構造的研究	高圧・応力科学研究グループ
日本原子力研究開発機構	XAFS 測定による分子・物質の構造的研究	磁性科学研究グループ
兵庫県立大学	クラスターイオンビームによる新規遷移金属化合物の創製と電子状態の解析	磁性科学研究グループ
室蘭工業大学	核融合炉ダイバータ用 SiC 複合材料/W 接合材における接合条件の最適化	高圧・応力科学研究グループ
物質・材料研究機構	原子二体分布関数法による機能性材料の先進的ナノ構造研究	高圧・応力科学研究グループ
日本原子力研究開発機構	放射光を利用した構造材料応力・変形評価に関する研究	高圧・応力科学研究グループ
日本原子力研究開発機構	廃炉及び福島環境復興のための技術開発	量子シミュレーション研究グループ

【施設共用課題】

　関西研では 2012 年度より文部科学省のナノテクノロジープラットフォーム事業を受託しており、放射光科学研究施設を成果公開型課題で利用する外部研究者に対して、特に専用ビームラインにおける研究支援を強化しています。課題は年 2 回、SPring-8 を運営する公益財団法人高輝度光科学研究センターの一般課題募集時期（5 月及び 11 月）に合わせて募集しています。

平成 29 年度前期施設共用課題

課題番号	利用区分	施設装置	利用課題
2017A-H01	公開	放射光メスバウアー分光装置	多核種メスバウアー装置による Ni ナノ粒子・MOF 複合体の研究
2017A-H02	公開	放射光メスバウアー分光装置	ユウロピウム水素化物（EuHx）の高圧水素雰囲気下メスバウアー分光測定
2017A-H03	公開	共鳴 X 線非弾性散乱装置	イオン液体で被覆した Pt3Ni ナノ粒子のオペランド高分解能 X 線吸収分光解析

課題番号	利用区分	施設装置	利用課題
2017A-H04	公開	共鳴 X 線非弾性散乱装置	ナトリウムイオン二次電池正極用固溶体の高分解能 XAFS 測定
2017A-H05	公開	共鳴 X 線非弾性散乱装置	Investigating the spin-state of electron-doped rare-earth nickelates with Ni-K β emission spectroscopy
2017A-H06	公開	共鳴 X 線非弾性散乱装置	RIXS test of the revolutionary idea of gradual Mott localization in La2-xSrxCuO4
2017A-H07	公開	表面 X 線回折計	InGaN 分子線エピタキシー成長におけるひずみ緩和過程のその場 X 線回折測定
2017A-H08	公開	表面 X 線回折計	RF 窒素プラズマを用いたサファイア基板窒化処理の XRD その場観察
2017A-H10	公開	単色 X 線実験用高温高圧プレス装置	高圧下における Fe-Ni-S 三成分系融体の熱膨張率測定
2017A-H11	公開	ダイヤモンドアンビルセル（DAC）回折計	ペロブスカイト PbMnO3、PbCoO3 の圧力誘起電荷移動転移の観察
2017A-H13	公開	ダイヤモンドアンビルセル（DAC）回折計	X 線 PDF 解析による長期材齢のセメントクリンカー硬化体及び混和材を混合したセメント硬化体中の C-S-H 変形挙動の解明
2017A-H14	公開	ダイヤモンドアンビルセル（DAC）回折計	Development of thin film PDF technique
2017A-H15	公開	ダイヤモンドアンビルセル（DAC）回折計	貴金属クラスターの水素雰囲気下での形成過程の解明と精密な構造解析
2017A-H16	公開	大型 X 線回折計	液体及び固体酸素の強磁場中 X 線回折によるスピン操作分子制御機構の解明
2017A-H17	公開	大型 X 線回折計	Yb(Ni1-xCux)3Al9 における結晶のキラリティとらせん磁気構造
2017A-H18	公開	大型 X 線回折計	フェムト秒レーザピーニングによって鉄中に形成された転位構造の解析

平成 29 年度後期施設共用課題

課題番号	利用区分	施設装置	利用課題
2017B-H01	公開	放射光メスバウアー分光装置	多元素メスバウアー分光法による Ni ナノ粒子・MOF 複合体の研究(II)
2017B-H02	公開	共鳴非弾性 X 線散乱装置	K β 線観測による LaCoO3 薄膜のスピン状態へのエピタキシャル歪みの影響の観測
2017B-H03	公開	表面 X 線回折計	その場 X 線回折測定を用いた GaInN 分子線エピタキシー成長におけるひずみ緩和過程の制御技術構築

2017B-H04	公開	表面X線回折計	その場X線回折測定を使用したグラフェン析出成長メカニズムの解明
2017B-H05	公開	表面X線回折計	放射光X線を用いた格子不整合III-V族化合物半導体混晶のリアルタイム構造解析
2017B-H06	公開	表面X線回折計	Development of a high-speed X-ray diffraction method for time-resolved in-situ observation of structure relaxation and dislocation creation in III-V semiconductor films
2017B-H08	公開	高温高圧プレス装置	高水素配位錯体水素化物における新たな固体イオニクスの開拓
2017B-H09	公開	高温高圧プレス装置	TRIP鋼の水素脆化に及ぼす金属組織状態と応力状態の影響
2017B-H10	公開	単色X線実験用高温高圧プレス装置	Nb-TiNi複相型水素透過合金の水素化—脱水素化過程の観察と耐水素脆化機構の解明
2017B-H11	公開	単色X線実験用高温高圧プレス装置	ダイヤモンドアンビルセルを用いたX線吸収による密度測定法の開発
2017B-H12	公開	ダイヤモンドアンビルセル回折計	FeSe1-xSxにおける圧力下構造解析
2017B-H13	公開	ダイヤモンドアンビルセル回折計	拡張ナノ空間の溶液X線回折測定による水の構造解析と物性発現機構の解明
2017B-H14	公開	ダイヤモンドアンビルセル回折計	異常散乱現象から得られる元素選択的二体分布関数解析を用いたゼオライト合成における無機カチオン種の構造規定効果の解明
2017B-H15	公開	ダイヤモンドアンビルセル回折計	Investigating the structures of nano-confined complex metal hydrides and transition metal nanoclusters
2017B-H16	公開	大型X線回折計	液体及び固体酸素の強磁場中X線回折によるスピン操作分子制御機構の解明
2017B-H17	公開	大型X線回折計	SmS圧力下異常金属相における磁気秩序
2017B-H20	非公開	共鳴非弾性X線散乱装置	高分解能蛍光検出XAFSによる高分子膜の分析
2017B-H21	非公開	大型X線回折計	鋼板内部の歪・応力非破壊解析2017
2017B-H22	非公開	大型X線回折計	水素吸蔵鉄鋼材料の一定荷重負荷中における転位密度その場観察測定
2017B-H23	非公開	共鳴非弾性X線散乱装置	高分解能蛍光検出XAFSによる高分子膜の分析（2）

関西光科学研究所でのシンポジウム・セミナー・ワークショップ等

　関西光科学研究所（木津地区、播磨地区）では、各種シンポジウム、セミナー、ワークショップ、研究会等を開催しています。また、研究所として参加した会合についても、主なものを記載しています。

1	9-10-May-2017	大阪大学銀杏会館（大阪府吹田市）	主催：量研関西光科学研究所、大阪大学レーザー科学研究所
	光・量子ビーム科学合同シンポジウム 2017 OPTO2017　Symposium on Photon and Beam Science		
2	11-May-2017	関西光科学研究所（播磨地区：兵庫県佐用郡佐用町）	主催：量研関西光科学研究所放射光科学研究センター
	第 1 回 QST 播磨・機械学習研究会		
3	25-August-2017	高崎量子応用研究所（群馬県高崎市）	主催：QST 微細構造解析プラットフォーム、JAEA 微細構造解析プラットフォーム
	平成 29 年度文部科学省ナノテクノロジープラットフォーム事業 JAEA・QST 微細構造解析プラットフォーム放射光設備利用講習会		
4	29-August-2017	科学技術振興機構（JST）東京本部別館（東京都千代田区）	主催:JAEA 微細構造解析プラットフォーム
	平成 29 年度第 1 回結晶 PDF 解析研究会/文部科学省ナノテクノロジープラットフォーム事業微細構造解析プラットフォーム第 1 回放射光利用研究セミナー		
5	4-5-September-2017	広島大学東千田未来創生センター（広島県広島市）	主催：SPring-8 ユーザー協同体（SPRUC）、（公財）高輝度光科学研究センター、理化学研究所放射光科学総合研究センター、広島大学（創発的物性物理研究拠点）
	SPring-8 シンポジウム 2017		
6	13-September-2017	東京大学本郷キャンパス　工学部 14 号館（東京都文京区）	主催　日本放射光学会
	第 9 回放射光基礎講習会		
7	26-September-2017	研究社英語センター(東京都新宿区)	主催:中性子産業利用推進協議会、茨城県中性子利用促進研究会、SPring-8 ユーザー協同体、JAEA 微細構造解析プラットフォーム
	平成 29 年度第 1 回残留ひずみ・応力解析研究会/微細構造解析プラットフォーム第 2 回放射光利用研究セミナー		
8	31-October-2017	関西光科学研究所（木津地区：京都府木津川市）	主催：科学技術振興機構、量研関西光科学研究所
	ImPACT「ユビキタス・パワーレーザーによる安全・安心・長寿社会の実現」第 6 回　運営会議（XFEL）・知財会議　開催案内		
9	2-November-2017	関西光科学研究所（播磨地区：兵庫県佐用郡佐用町）	主催：関西光科学研究所放射光科学研究センター
	第 2 回 QST 播磨・機械学習研究会		
10	24-November-2017	リーガロイヤルホテル（大阪府大阪市）	主催：関西光科学研究所、大阪大学
	光量子ビーム科学シンポジウム 2017　「光量子ビーム科学　コ・クリエーション」		
11	8-10-January-2018	つくば国際会議場(茨城県つくば市)	主催：第 31 回日本放射光学会年会・放射光科学合同シンポジウム組織委員会
	第 31 回日本放射光学会年会・放射光科学合同シンポジウム		

12	23-January-2018	京都大学 国際科学イノベーション棟（京都府京都市）	主催：文部科学省、量子科学技術研究開発機構、大阪大学、東京大学、京都大学、分子科学研究所、理化学研究所、慶應義塾大学、電気通信大学、東京工業大学
	第 10 回 文部科学省「最先端の光の創成を目指したネットワーク研究拠点プログラム」		
13	2-February-2018	関西光科学研究所（播磨地区：兵庫県佐用郡佐用町）	主催：量研関西光科学研究所放射光科学研究センター
	第 3 回 QST 播磨・機械学習研究会		
14	9-February-2018	TKP ガーデンシティ京都（京都府京都市）	主催：京大微細構造解析プラットフォーム最先端構造観察・計測共用拠点、JAEA 微細構造解析プラットフォーム、NIMS 微細構造解析プラットフォーム、QST 微細構造解析プラットフォーム
	京大・JAEA・NIMS・QST 微細構造解析プラットフォーム地域セミナー「分光法の最前線」		
15	14-Febrauary-2018	関西光科学研究所（木津地区：京都府木津川市）	主催：量研関西光科学研究所、理研光量子工学研究センター
	RIKEN-RAP and QST-KPSI Joint Seminar　（テーマ：アト秒科学）		
16	21-February-2018	東京大学本郷キャンパス 小柴ホール（東京都文京区）	主催：文部科学省
	文部科学省光・量子融合連携研究開発プログラムシンポジウム		
17	12-14-March-2018	SPring-8（兵庫県佐用郡佐用町）	主催：量子科学技術研究開発機構 関西光科学研究所放射光科学研究センター、日本原子力研究開発機構物質科学研究センター放射光エネルギー材料研究ディビジョン、JAEA&QST 微細構造解析プラットフォーム
	JAEA-QST 放射光科学シンポジウム 2018/微細構造解析プラットフォーム第 3 回放射光利用研究セミナー		
18	26-March-2018	エッサム神田（東京都千代田区）	主催：中性子産業利用推進協議会、茨城県中性子利用促進研究会、SPring-8 ユーザー協同体、JAEA 微細構造解析プラットフォーム
	平成 29 年度第 2 回残留ひずみ・応力解析研究会/微細構造解析プラットフォーム第 4 回放射光利用研究セミナー		
19	29-30-March-2018	関西光科学研究所（木津地区：京都府木津川市）	主催：固体飛跡検出器研究会、量研関西光科学研究所
	31st Workshop on Solid State Nuclear Track Detectors		

KPSI セミナー（**Kansai Photon Science Institute Seminar**）

　関西光科学研究所（木津地区）では国内外の著名な研究者をお招きして学術的に最先端の専門的なセミナーを開催しています。今年度は合計 16 回のセミナーを開催しました。開催にあたっては KPSI Web サイトやメーリングリストを活用し、関西研内外に開催案内を行っています。また、報告についても Web サイトを活用しています。

Web サイト：http://www.kansai.qst.go.jp/seminar-0.html

1	14-April-2017	Dr. Ceri Brenner	Central Laser Facility, Science and Technology Facilities Council, UK
	Industry engagement and development of laser-driven beams for applications in medicine through to manufacturing		
2	17-April-2017	Dr. Ji-Ping Zou	Laboratoire pour l'Utilisation des Lasers Intenses, CNRS, Ecole Polytechnique, Palaiseau, France
	Current status of the LULI laser facilities		
3	25-April-2017	Dr. Felix Karbstein	Helmholtz Institute in Jena, Germany
	Probing quantum vacuum nonlinearities with high-intensity lasers		
4	23-May-2017	Dr. Natsumi Iwata	Institute of Laser Engineering, Osaka University, Japan
	Fast ion acceleration in a foil plasma heated by a multi-picoseconds high intensity laser		
5	31-May-2017	Dr. Maxence Gauthier	High Energy Density Science, SLAC, USA
	High-intensity short-pulse laser proton acceleration from condensed hydrogen jet		
6	15-June-2017	Prof. Sergei V. Bulanov	KPSI, QST, Japan
	On the way towards novel applied and fundamental physics		
7	5-July-2017	Dr. Timur Esirkepov	KPSI, QST, Japan
	Paradoxical Stabilization of Forced Oscillations by Strong Nonlinear Friction		
8	12-July-2017	Prof. Hirohiko Kono	Department of Chemistry, Graduate School of Science, Tohoku University, Japan
	Reaction dynamics simulation: From XFEL-induced Coulomb explosion to strand breaks in DNAs		
9	14-September-2017	Dr. Sergey A. Pikuz	JIHT RAS, Russia
	X-ray emission and absorption spectroscopy to study laser-initiated WDM.		
10	4-October-2017	Prof. Carles Serrat	Departament de Física Universitat Politècnica de Catalunya, Spain
	Simulations on strong field driven XUV attosecond pulse amplification		
11	12-October-2017	Dr. Thomas Metzger	TRUMPF Scientific Lasers GmbH + Co. KG, Germany
	High Average Power Ultrafast Thin-Disk Amplifiers		

12	12-October-2017	Dr. Motoaki Nakatsutsumi	Osaka University, Japan/ European XFEL, Germany
	Short-pulse high-intensity laser-plasma science using an X-ray free electron laser		
13	15-November-2017	Dr. Bruno Gonzalez-Izquierdo	KPSI, QST, Japan
	Collective charged particle dynamics in relativistically transparent laser-plasma interactions		
14	19-January-2018	Dr. Hui Chen	Lawrence Livermore National Laboratory, USA
	Relativistic electron-positron jets from intense lasers		
15	5-February-2018	Prof. Sergei V. Bulanov	ELI-BL, Czech Republic/ KPSI, QST, Japan
	On the High Field Initiative Project at ELI-Beamlines		
16	20-March-2018	Dr. Hisataka Kobayashi	National Cancer Institute, NIH, USA
	Near Infrared Photoimmunotherapy for Cancer		

QST 播磨セミナー

　関西光科学研究所（播磨地区）では国内外の著名な研究者をお招きして学術的に最先端の専門的なセミナーを開催しています。

1	21-June-2017	八巻　徹也　上席研究員	QST　高崎量子応用研究所
	量子ビームを利用した水素エネルギー材料の創製研究　－燃料電池部材を中心にして－		
2	9-August-2017	森　茂生　教授	大阪府立大学
	$SrAl_2O_4$ の強誘電相での特異なドメイン構造の TEM 観察		
3	23-Augugst-2017	武市　泰男　助教	高エネルギー加速器研究機構 放射光科学研究施設
	PF での硬・軟 X 線顕微分光と将来展望		

S-cube（スーパーサイエンスセミナー）

　関西光科学研究所では中学高校生を中心に一般の方に光科学についての理解を深めていただくことを目的に、第一線の研究者による講義「S-cube（エスキューブ：スーパーサイエンスセミナー）」を開講しています。

　2017 年度は合計 13 回（第 186 回～第 198 回）開催し、研究の楽しさ体験や参加者と研究者との交流を行うことができました。また、開催に際しては案内を KPSIWeb サイト等で行ってきたことにより一般参加（市民）もあり、デモ実験等含めた本セミナーをけいはんな地域の方にも体験いただきました。

Web サイト：http://www.kansai.qst.go.jp/s-cube-0.html?btnG=S-Cube

186	09-June-2017	講師：森林　健悟　放射線 DNA 損傷研究グループ	83 人参加
	テーマ：光と放射線のおはなし		
187	24-July-2017	講師：岡田　大　研究企画室	7 人参加
	テーマ：レーザー基礎とレーザー安全講習		
188 （第 1 部）	02-August-2017	講師：青山　誠　レーザー医療応用研究グループ	46 人参加
	テーマ：手のひらサイズの非侵襲血糖値センサー		
188 （第 2 部）	02-August-2017	講師：長谷川　登　X 線レーザー研究グループ	46 人参加
	テーマ：コンクリートの欠陥を遠くから見つける～屋外で使う高強度レーザー～		
189	03-August-2017	講師：赤木　浩　超高速光物性研究グループ	21 人参加
	テーマ：分子を分けるって？～レーザー同位体分離について～		
190	09-August-2017	講師：宮坂　泰弘　先端レーザー技術開発グループ	37 人参加
	テーマ：レーザーを使うと何ができるの？		
191	21-September-2017	講師：鹿園　直哉　量子生命科学研究部	15 人参加
	テーマ：電離放射線の生物影響の原因は何か？		
192	01-Feburary-2017	講師：近藤　康太郎　高強度レーザー科学研究グループ	194 で実施
	テーマ：High power lasers open a new world for science		
193	08-Feburary-2017	講師：森林　健悟　放射線 DNA 損傷研究グループ	78 人参加
	テーマ：光と放射線のおはなし		
194	13-Feburary-2017	講師：近藤　康太郎　高強度レーザー科学研究グループ	22 人参加
	テーマ：ハイパワーレーザーが拓く新しい科学の世界		
195	23-Feburary-2017	講師：坪内　雅明　超高速光物性研究グループ	40 人参加
	テーマ：暮らしの中の光 ～ 「色」で理解しよう		
196	15-March-2017	講師：宮坂　泰弘　先端レーザー技術開発グループ	23 人参加
	テーマ：生活を支えるレーザー技術		
197	26-March-2017	講師：宮坂　泰弘　先端レーザー技術開発グループ	30 人参加
	テーマ：生活を支えるレーザー技術		
198	28-March-2017	講師：近藤　公伯　光量子科学研究部	27 人参加
	テーマ：量子メス（レーザーによる粒子加速とがん治療器開発）		

施設公開・出展・アウトリーチ活動

関西光科学研究所では、施設公開（年間 2 回：播磨地区 1 回（毎年 4 月ごろ）、木津地区 1 回（毎年 10 月ごろ））や研究成果のわかり易い公表、光科学の基礎についての出前授業、科学啓発イベント等への出展を積極的に進めています。

ここでは主なものを記載し、「きっづ光科学館ふぉとん」、S-cube（スーパーサイエンスセミナー）については別途記載しています。

1	30-April-2017	SPring-8（兵庫県佐用郡佐用町）	主催：理化学研究所放射光科学総合研究センター
	第 25 回 SPring-8/SACLA 施設公開		
2	9-12-July-2017	SPring-8（兵庫県佐用郡佐用町）	主催：兵庫県立大学、関西学院大学、東京大学、岡山大学、大阪大学、高輝度光科学研究センター、理化学研究所、日本原子力研究開発機構、関西光科学研究所
	第 17 回 SPring-8 夏の学校		
3	22-23-July-2017	桜山公園（兵庫県姫路市）	主催：姫路科学館、星の子館、兵庫県立こどもの館、姫路市自然観察の森
	桜山公園まつり「科学の屋台村」に参加		
4	28-July-2017	北陸先端科学技術大学院大学東京サテライト（東京都港区）	主催：ナノテクノロジープラットフォーム事業分子・物質合成プラットフォーム、大学連携研究設備ネットワーク事業
	平成 29 年度第 5 回技術職員・技術支援者研修会		
5	29-30-July-2017	科学技術館（東京都千代田区）	主催：日本科学技術振興財団
	青少年のための科学の祭典 2017		
6	1-August-2017	科学技術振興機構（JST）東京本部別館（東京都千代田区）	主催：科学技術振興機構、量子科学技術研究開発機構
	新技術説明会		
7	2-August-2017	関西光科学研究所（木津地区：京都府木津川市）	主催：木津川市教育委員会、きっづ光科学館ふぉとん、関西光科学研究所
	「科学のまちの子どもたち」を育てる木津川市立学校教員研修会		
8	21-25-August-2017	SPring-8（兵庫県佐用郡佐用町）	主催：量子科学技術研究開発機構
	平成 29 年度 QST サマースクール		
9	11-15-September-2017	関西光科学研究所（播磨地区：兵庫県佐用郡佐用町）	主催：ナノテクノロジープラットフォームセンター
	平成 29 年度文部科学省ナノテクノロジープラットフォーム事業学生研修プログラム		
10	28-29-September-2017	けいはんなオープンイノベーションセンター（京都府相楽郡精華町）	主催：京都スマートシティエキスポ運営協議会
	京都スマートシティエキスポ 2017		

11	28-September-2017	科学技術振興機構（JST）東京本部（東京都千代田区）	主催：ナノテクノロジープラットフォームセンター
	文部科学省ナノテクノロジープラットフォーム事業平成 29 年度学生研修プログラム成果発表会		
12	2-October-2017	東京大学浅野キャンパス（東京都文京区）	主催：微細構造解析プラットフォーム
	2017 年度微細構造解析プラットフォームシンポジウム		
13	10-October-2017	播磨高原広域事務組合立播磨高原東中学校（兵庫県たつの市）	主催：関西光科学研究所
	中学校で出前授業		
14	20-October-2017	科学技術振興機構（JST）東京本部（東京都千代田区）	主催：ナノテクノロジープラットフォームセンター
	平成 29 年度ナノテクノロジープラットフォーム総会		
15	21-October-2017	木津川台小学校（京都府木津川市）	主催：木津川台小学校
	木津川台小学校出張教室		
16	22-October-2017	関西光科学研究所（木津地区：京都府木津川市）	主催：関西光科学研究所
	関西光科学研究所施設公開（木津地区）		
17	26-27-October-2017	けいはんなプラザ（京都府相楽郡精華町）	主催：関西文化学術研究都市推進機構
	けいはんなビジネスメッセ 2017		
18	26-28-October-2017	けいはんなプラザ（京都府相楽郡精華町）	主催：けいはんな情報通信フェア 2017 実行委員会、情報通信研究機構、関西文化学術研究都市推進機構、国際電気通信基礎技術研究所、関西経済連合会
	けいはんな情報通信フェア 2017		
19	29-October-2017	大阪科学技術館（大阪府大阪市）	主催：大阪科学技術センター
	サイエンス・ステージ		
20	27-November-2017	JFE テクノリサーチ　ナノ解析センター（千葉県千葉市）	主催：QST 微細構造解析プラットフォーム
	QST 微細構造解析プラットフォーム説明会		
21	4-December-2017	大阪イノベーションハブ（大阪府大阪市）	主催：科学技術振興機構（JST）
	JST 産学連携事業平成 29・30 年度公募説明会		
22	4-8-December-2017	九州大学伊都キャンパス（福岡県福岡市）	主催：ナノテクノロジープラットフォームセンター
	平成 29 年度ナノプラ技術スタッフ交流プログラム		

23	12-13-December-2017	高崎シティギャラリー（群馬県高崎市）	主催：QST 高崎量子応用研究所
	QST 高崎サイエンスフェスタ		
24	22-December-2017	名古屋大学東山キャンパスベンチャーホール（愛知県名古屋市）	主催：ナノテクノロジープラットフォーム、分子・物質合成プラットフォーム、大学連携研究設備ネットワーク事業
	文部科学省ナノテクノロジープラットフォーム事業平成 29 年度技術職員・技術支援者研修会		
25	14-16-February-2018	東京ビッグサイト（東京都江東区）	主催：nano tech 実行委員会
	【nano tech 2018】第 17 回国際ナノテクノロジー総合展・技術会議		
26	16-February-2018	東京ビッグサイト（東京都江東区）	主催：文部科学省ナノテクノロジープラットフォーム、物質・材料研究機構ナノテクノロジープラットフォームセンター
	第 16 回ナノテクノロジー総合シンポジウム「持続的な社会発展に向けたナノテクノロジー」（JAPAN NANO 2018）		
27	26-February-2018	SPring-8（兵庫県播磨科学公園都市））	主催：軽金属溶接協会レーザ溶接委員会、JAEA 微細構造解析プラットフォーム、QST 微細構造解析プラットフォーム
	平成 29 年度一般社団法人軽金属溶接協会レーザ溶接委員会/平成 29 年度文部科学省ナノテクノロジープラットフォーム事業 JAEA・QST 微細構造解析プラットフォーム放射光施設見学会		
28	13-March-2018	イーグレひめじ（兵庫県姫路市）	主催：兵庫県立大学高度産業科学技術研究所
	兵庫県立大学　高度産業科学技術研究所　先端技術セミナー2018		
29	13-March-2018	科学技術振興機構（JST）東京本部（東京都千代田区）	主催：ナノテクノロジープラットフォームセンター
	文部科学省ナノテクノロジープラットフォーム平成 29 年度技術スタッフ交流プログラム報告会		
30	27-March-2018	イイノホール＆カンファレンスセンター（東京都千代田区）	主催：物質・材料研究機構微細構造解析プラットフォーム
	オールジャパン構造解析ワークショップ 2018　～微細構造解析研究基盤構築の現状と展望～		
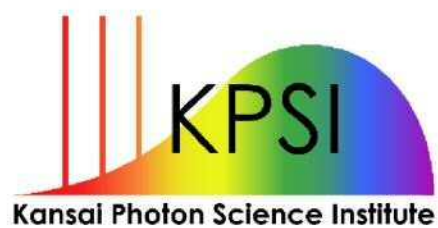
KANSAI PHOTON SCIENCE INSTITUTE
Quantum Beam Science Research Directorate
National Institutes for Quantum and Radiological Science and Technology

8-1-7, Umemidai, Kizugawa-shi, Kyoto 619-0215, Japan
http://www.kansai.qst.go.jp/kpsi-en/index.html